THE UNIVERSITY OF CHICAGO

STUDIES OF NEUTRAL YTTERBIUM ATOMS IN A SOLID NEON MATRIX

A DISSERTATION SUBMITTED TO
THE FACULTY OF THE DIVISION OF THE PHYSICAL SCIENCES
IN CANDIDACY FOR THE DEGREE OF
DOCTOR OF PHILOSOPHY

DEPARTMENT OF PHYSICS

BY
CHEN-YU XU

CHICAGO, ILLINOIS
MARCH 2015

To My Mother,

for Enduring My Absence for Over Six Years.

道雖邇, 不行不至; 事雖小, 不爲不成.

——《荀子 · 修身》

A destination might seem close, but you would never arrive unless you depart.

A work might sound trivial, but you would never finish unless you embark.

—— Xunzi, Chapter 2 (Self-Cultivation)

ACKNOWLEDGMENTS

First and foremost, I would like to express my deepest gratitude to my advisor Zheng-Tian Lu (卢征天). Five and a half years ago when I was still immersed in the depression that my dream of being a theoretical condensed matter physicist was doomed, he agreed to take me on as a student in his labs at Argonne National Laboratory. Over the years, he has convinced me that the key to a good experimentalist is exactly the same as to a good theorist. Thank you, Lu, for teaching me what makes a successful researcher! I know I am doing way below your expectation in some aspects, but I will definitely keep working on that in my future positions. In addition, I appreciate that you often encourage me to nurture my hobbies in spare time, which will certainly accompany me for a lifetime.

During my Ph.D. work at Argonne, I have had the privilege of working closely with senior researchers Shui-Ming Hu (胡水明), Jaideep Singh, Peter Mueller, and Wei Jiang (蒋蔚). I feel extremely lucky to have worked with Shui-Ming in the early years, from whom I picked up all my knowledge in matrix isolation. The wonderful start of this project was not possible without his help, which made me feel more and more excited about this project. I am very grateful to Jaideep not only for his enormous help and the pleasant time we spent working together, but also for him being a model of an excellent postdoc which I will reference to a lot in the next a few years. I thank Peter and Wei for sharing their knowledge and experience. There were many times that a ten-minute discussion with them answered all the questions I had pondered over for a few days.

I acknowledge Kevin Bailey and Tom O'Connor for the thoughtfully designed apparatus that made my life easier; Will Williams, for giving me the first taste of experimental physics; Will Trimble, for offering rides and sharing puzzles; and Jake Zappala, for kindly allowing me to spend most of the last two months writing this dissertation. I thank all other past and current members in the atom trapping group including Roy Holt, Ibrahim Sulai, Brent Graner, Richard Parker, Yu Sun (孙羽), Mukut Kalita, Matt Dietrich, Guo-Ming Yang (杨国民), Nathan Lemke, and Mike Bishof, from whom I learned a great deal.

I would like to thank the following people for their help at different stages of my thesis work: Bob Dunford, for the gift of the monochromator for high resolution spectroscopy; Steve Pratt and Hong Xu (徐红), for allowing Jaideep and me to use their new OPO for laser spectroscopy; John Greene, for loading the isotopically pure Yb samples into the crucible; Chen-Yu Liu, for teaching Jaideep and me how to operate a SQUID and lending us her own SQUID; Jon Weistein, for teaching me how to calculate the optical pumping rate for nuclear polarization at the presence of a crystal field; and Ulrich Welp, for proposing this project with Lu to LDRD which financially supported me for the first three years.

I acknowledge Cheng Chin, Philippe Guyot-Sionnest, David Mazziotti, and Takeshi Oka for serving on my thesis committee and I appreciate their suggestions and comments that helped me better understand our system. I particularly thank Oka for the gift of the cryostat that made all the experiments possible. I am indebted to Nobuko McNeill, Autym Henderson, David Reid, Barb Fletcher, Colleen Tobolic, Kathleen Daily, Kim Miller, and Debbie Beres for their help in the administrative work.

I would like to thank all the friends I have made over the years in Chicago. You are the reason why I never feel lonely in a place thousands of miles away from my home country. Finally, I thank my father (徐伟民) and my mother (成怡芬) for giving me the freedom to pursue what I like and study abroad. I thank my grandmother (林翠英) for always having confidence in me. Last but not least, I thank my wife (贺海伦) for the warm home she gave me and for holding my hands whenever I feel restless.

This work was supported by the Department of Energy, Office of Nuclear Physics.

ABSTRACT

Ytterbium (Yb) atoms frozen in a solid neon (Ne) matrix qualitatively retain the structure of free atoms. Yb transitions are found to be mostly blue-shifted in both absorption and emission spectra. Transitions also acquire significantly broadened linewidth, which can be a few nanometers for outer-shell transitions and as narrow as 0.03 nm (or 120 GHz) for inner-shell transitions. We explicitly demonstrate that the linewidth broadening is homogeneous for the $6s^2\ {}^1S_0 - 6s6p\ {}^1P_1$ transition. Splitting of transitions is observed as well, and is attributed to the broken spherical symmetry of the Yb trapping sites in solid Ne.

The lifetimes of $6s6p\ {}^3P_{0,1}$ in both ^{171}Yb and ^{172}Yb are measured in solid Ne using the spectrally-resolved fluorescence-decay technique. The finite vacuum lifetime of $6s6p\ {}^3P_0$ in ^{171}Yb is due to the hyperfine quenching, and gives the natural linewidth of the Yb clock transition. With the measurements in solid Ne, we extract this vacuum lifetime for the first time after correcting for various medium effects. One effect is the index-of-refraction dependence of the spontaneous emission, of which we perform an independent calibration based on the $6s6p\ {}^3P_1$ lifetime in vacuum and in solid Ne. We obtain a vacuum decay rate of $(4.42 \pm 0.35) \times 10^{-2}$ s^{-1} for $6s6p\ {}^3P_0$ in ^{171}Yb, which agrees with a recent calculation.

The feasibility of optically polarizing ^{171}Yb nuclei in solid Ne is discussed. The excitation rate of Yb transitions in solid Ne is suppressed by the same factor by which the absorption linewidth is broadened. The optical pumping efficiency for nuclear spins is estimated to be further suppressed by four orders of magnitude due to the presence of the crystal field. Finally, a few experiments are proposed as the applications of our techniques or ways to further understand the system of impurity atoms in solid noble gases.

TABLE OF CONTENTS

LIST OF TABLES

LIST OF FIGURES

LIST OF SYMBOLS

A	absorbance; hyperfine constant
$\boldsymbol{A}, A$	vector potential
$\mathscr{A}_1, \mathscr{A}_2, \mathscr{E}, \mathscr{T}_1, \mathscr{T}_2$	irreducible representation of O or D_3
a	area
a_B	Bohr radius
a_i, ϕ_i, q_i	crystal field parameter
$\boldsymbol{B}, B$	magnetic field
$\mathscr{C}$	class, class of a group
c_n	coefficient of Fourier expansion
D	duty cycle
D_3	dihedral group
$D(\omega)$	density of states
$\mathscr{D}$	electric-dipole operator
$\mathscr{D}^{(j)}$	irreducible representation of $SO(3)$
d	distance, nearest-neighbor distance
E	energy
$\boldsymbol{E}, E$	electric field
e	elementary charge
$\boldsymbol{F}, F$	total angular momentum of an atom
$f(\cdot), g(\cdot), G(\cdot), K(\cdot)$	function
g_I	nuclear g-factor
H, N	count, integer number
$\mathscr{H}$	Hamiltonian
$h, \hbar$	Planck constant, reduced
I	light intensity
$\boldsymbol{I}, I$	nuclear spin angular momentum
i	unit imaginary number
i, j, m, n	integer index
$\boldsymbol{J}, J$	total angular momentum of electrons
j_x, j_y, j_z	matrix representation of an angular momentum operator
k_B	Boltzmann constant
$\boldsymbol{L}, L$	total orbital angular momentum of electrons
$\boldsymbol{l}, l$	orbital angular momentum of an electron
M	mass; z-component of L, J, I, or F
m	z-component of l
n	number density; index of refraction
O	octahedral group
$\boldsymbol{P}, P, \mathcal{P}$	polarization
p	pressure
Q	flux density of particles; configuration coordinate
Q_0, v_0, w	Morse potential parameter
R	radius

$R(r)$	radial part of a wave function
$\mathbf{R}$	lattice vector
$\mathscr{R}$	representation of a group
$\boldsymbol{r}, r$	displacement vector
(r, θ, ϕ), (r, Ω)	spherical coordinate system
$\boldsymbol{S}, S$	total spin angular momentum of electrons
SO(3)	3D rotation group
s	thickness
T	temperature
T_D	Debye temperature
T_1, T_2	relaxation time
$\mathbb{T}^{-1}$	relaxation matrix
t	time
$U(\boldsymbol{r})$	crystal field potential
u, v, w	coherences and population in the optical Bloch equations
$V(Q)$	potential energy surface
v	velocity
$v(Q)$	Morse potential
W	broadening factor of a transition
(x, y, z)	Cartesian coordinate system
$Y_{lm}(\Omega)$	spherical harmonics

α, β	dimensionless parameter
Γ	rate
γ	gyromagnetic ratio
ϵ, ϵ_0	permittivity, vacuum permittivity
η	excitation/decay rate ratio
λ	eigenvalue of a Hamiltonian; wavelength
$\boldsymbol{\mu}, \mu$	magnetic dipole moment
μ_0	vacuum permeability
μ_N	nuclear magneton
ν	wavenumber; frequency
ξ	dilution factor
(ρ, ϕ, z)	cylindrical coordinate system
$\Sigma, \partial\Sigma$	2D surface and its boundary
σ	cross-section of atom-photon interaction
τ	decay lifetime, time constant
Φ	magnetic flux
Φ_0	magnetic flux quantum
χ	character of a group element
$\psi(\boldsymbol{r})$	wave function
Ω	rotation of 2π
ω	angular frequency
ω_L	Larmor (angular) frequency
ω_R	Rabi (angular) frequency

CHAPTER 1

INTRODUCTION

1.1 Matrix Isolated Atoms

The interest of studying a guest species isolated in a noble-gas solid originally lies in the fact that chemically unstable molecules and free radicals in the gas phase remain stable in these inert solids and thus can be spectroscopically studied at leisure [1]. In addition, matrix isolation spectroscopy has more advantages over gas-phase spectroscopy including the possibility of simultaneously studying multiple transitions and studying states not accessible from the ground state by an allowed transition [2]. In the case of large molecules such as aromatic hydrocarbons, the absorption and emission lines are so narrow in a matrix that single-molecule spectroscopy has been demonstrated [3].

In contrast, matrix isolated atoms are not suitable for precision spectroscopy because the electronic levels of these trapped atoms are usually broadened to a few hundred cm^{-1} [4]. This can be explained by the different atom-matrix coupling when the atom is in the lower and upper states [5]. This phenomenon is quite similar to the way that an atom interacts with other atoms in a molecule [6]. However, since matrix isolation provides an efficient trapping, a high density, and a stable confinement for the atoms of interest, this technique has potential for applications including measuring lifetimes of forbidden transitions [7], building optical magnetometers [8], studying rare isotopes [9], catching and detecting rare decay products [10], and testing fundamental symmetries [11].

In particular, the applications of building optical magnetometers and searching for the electron's electric dipole moment rely on the prerequisite that the electronic spins of matrix isolated atoms can be efficiently polarized by optical pumping and the spin relaxation times are reasonably long in the matrix. Efforts to polarize alkali atoms isolated in noble-gas solids by optical pumping were pioneered by F. Pipkin and his colleagues in the 1960's [12, 13]. Although not accomplished then, with the greatly improved pumping rate due to the invention

of lasers, optically polarizing the electronic spins of alkali atoms isolated in condensed noble gases is now a mastered technique. The electronic-spin relaxation times have been measured to be somewhere between a tenth of a second and a few seconds [14, 15, 8]. On a different path, it has also been demonstrated that polarization of impurity ions is achieved by optical pumping in some ionic crystals where the magnetic circular dichroism is large [16, 17].

1.2 Motivations

The work presented in this dissertation was originally motivated to investigate the feasibility of optically polarizing the *nuclear spins of diamagnetic atoms* isolated in noble-gas solids. Such a technique has never been reported in literature. To our interest, once this is successful, the system opens up the potential for measuring the nuclear Schiff moment [18] of heavy neutral atoms in a solid matrix. The relaxation times of nuclear spins in noble-gas solids are known to be very long due to their weak coupling to the environment [19]. Conventionally, the nuclear polarization of a condensed matter sample is created by the Boltzmann factor at high fields and low temperatures [20]. But the optical-pumping method provides a much more efficient and controllable way. Because photons only strongly interact with atomic electrons, optical creation of nuclear polarization in a matrix requires that the hyperfine interaction is not significantly perturbed.

As a test case, we use Yb atoms as the guest species and solid Ne as the host matrix. Yb is a diamagnetic atom, and its ground level is $^1S_0$ where the electronic spin is zero. Yb has an abundant isotope ^{171}Yb with nuclear spin 1/2, which is an ideal candidate for studying nuclear magnetic resonance due to the absence of the electric quadrupole moment [21]. We choose solid Ne as the matrix because Ne is easier to solidify than He and interacts more weakly with the guest species than heavier noble gases [22]. The nuclear-spin relaxation times of ^{21}Ne nuclei have also been measured in solid Ne [23]. The spin-lattice relaxation time is about a few hundred seconds, and the spin-spin relaxation time is about a few seconds at the melting point (25 K) and decreases to a few millisecond at 15 K.

Although we have not yet observed the nuclear polarization signal of ^{171}Yb in solid Ne, with that goal in mind we have obtained many interesting results including the observations that atomic metastable levels persist in a matrix and that the intersystem crossing between different spin states is enhanced in a matrix [24], and the measurements of the hyperfine quenching rate in ^{171}Yb and enhanced spontaneous emission rates in a medium [7]. Moreover, we have gained some understanding of how the solid Ne matrix alters the atomic structure of the trapped Yb so as to lay the foundation for future efforts on nuclear polarization by optical pumping in noble-gas matricies.

1.3 Overview of Dissertation

This dissertation is organized as follows. In Chapter 2, I will describe the recipe for preparing the Yb/Ne samples. In Chapter 3, I will present the results on optical spectroscopy with explanations for the linewidth broadening and the line splitting in a matrix. In Chapter 4, I will present the lifetime measurements of the two lowest excited levels $6s6p\ ^3P_{0,1}$ of Yb in solid Ne. In Chapter 5, I will discuss the possibility of optically polarizing ^{171}Yb nuclei in solid Ne based on the results in the previous chapters. In Chapter 6, I will give a brief summary of the current work and some suggestions for future work.

Finally, I have compiled many technical details such as equation solving, dead-time correction, matrix diagonalization, pumping-rate calculation, and magnetic-flux calculation in the appendices. This by no means implies that these details are not important. On the contrary, they are some of my most original calculations that provide insights to many of our observations. The intent of leaving them in the appendices is simply to allow the main texts to flow more smoothly.

CHAPTER 2

MATRIX ISOLATION OF YB IN SOLID NE

In this chapter, I will describe how we prepare the Yb/Ne samples. I will first discuss the relevant physical properties of Yb and Ne, which determine the scheme for matrix isolation of Yb in solid Ne. Then I will describe the apparatus and the procedure for making samples. Finally, I will introduce the parameters to characterize the Yb density of the samples.

2.1 Properties of Yb and Ne

Yb is a rare earth and the fourteenth element in the lanthanide series. The pure form of Yb is a soft, malleable and ductile metal that displays a bright silvery luster [25]. It oxidizes slowly in air and is stored under the Ar atmosphere in our lab. The sublimation pressure of Yb (Figure 2.1) is significantly higher than other lanthanides due to the fact that only the two valence electrons are available for metallic bonding. However, to achieve a significant vapor pressure for matrix isolation experiments, we are required to use an effusive oven with a crucible to heat up the Yb sample. Yb with natural isotopic abundance is purchased from Sigma-Aldrich in the form of chips that are relatively easy to load into the crucible.

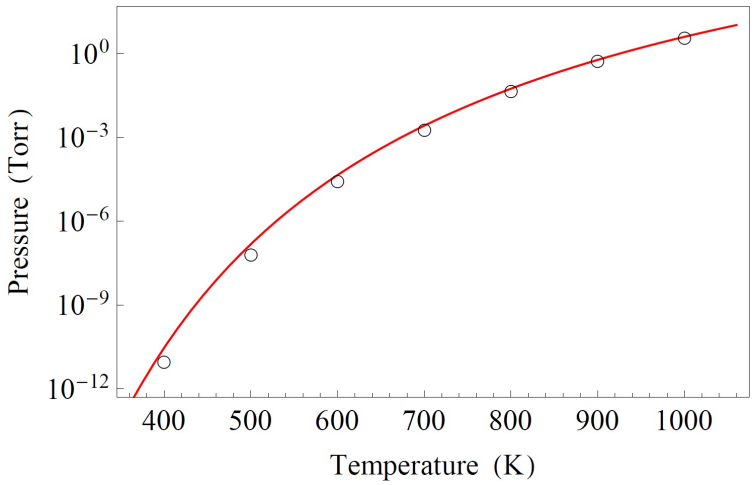

Figure 2.1: The sublimation pressure of Yb. Data are taken from Reference [26] and plotted as open circles. The red curve is a fit with the Clausius-Clapeyron equation.

We choose solid Ne among other popular host matrices in Table 2.1 for the following reasons. Compared to other noble gases, Ne has the second smallest polarizability. Therefore solid Ne is expected to perturb the structure of the guest atom more weakly than heavier noble gas solids, but more strongly than solid He. However, He is not as technically accessible as Ne because it only freezes under the pressure of 26 atm. Ne, in contrast, readily solidifies at 25 K under the atmospheric pressure. Solid para-hydrogen (p-H_2) is another commonly used matrix due to its quantum nature similar to solid He in preserving the symmetry of the embedded defect [27]. We briefly experimented with isolating Yb in solid H_2 and found that optically excited Yb atoms can react with H_2 and form stable molecules.

Table 2.1: Properties of commonly used host matrices [22, 28].

	He	Ne	Ar	Kr	Xe	p-H_2
lattice structure	hex	fcc	fcc	fcc	fcc	hex
lattice constant (Å)	3.57	4.43	5.26	5.72	6.20	3.75
density (10^{22} cm^{-3})	2.70	4.60	2.75	2.13	1.68	2.68
freezing temperature (K)	~ 1.0	24.5	83.9	116.5	161.3	14.0
freezing pressure (atm)	26	1	1	1	1	1
polarizability (Å^3)	0.204	0.392	1.63	2.47	4.01	0.787
nuclear spin impurities	^{3}He	^{21}Ne	/	^{83}Kr	^{129,131}Xe	o-H_2, HD
natural abundance	1.4 ppm	0.27%	/	11.5%	47.6%	115 ppm

For applications requiring long coherence of Yb nuclear spins, we prefer fewer spin impurities in the matrix (Section 5.3). One such impurity is the isotopes of the matrix atoms that possess nonzero nuclear spins. Ne has 0.27% of ^{21}Ne with nuclear spin 3/2 which puts a limit on the spin-spin relaxation time of Yb atoms. In this respect, solid Ar seems a more suitable matrix because none of its abundant isotopes has a nonzero nuclear spin. However, besides a larger polarizability, thick solid Ar samples are not as transparent as solid Ne. Fortunately, Ne gas with depleted isotope of ^{21}Ne is commercially available.

Perfectly crystallized solid Ne is transparent in the visible-ultraviolet wavelength range. Its lattice structure is face-centered-cubic with a cubic lattice constant of 4.43 Å. The sublimation pressure of solid Ne is shown in Figure 2.2. Under reduced pressures, the freezing temperature of solid Ne decreases accordingly. Based on our experience, solid Ne samples

start melting near 8 K, which implies that the vacuum in the cryostat is better than 10^{-7} Torr at this temperature (see the extrapolated curve in the right panel of Figure 2.2).

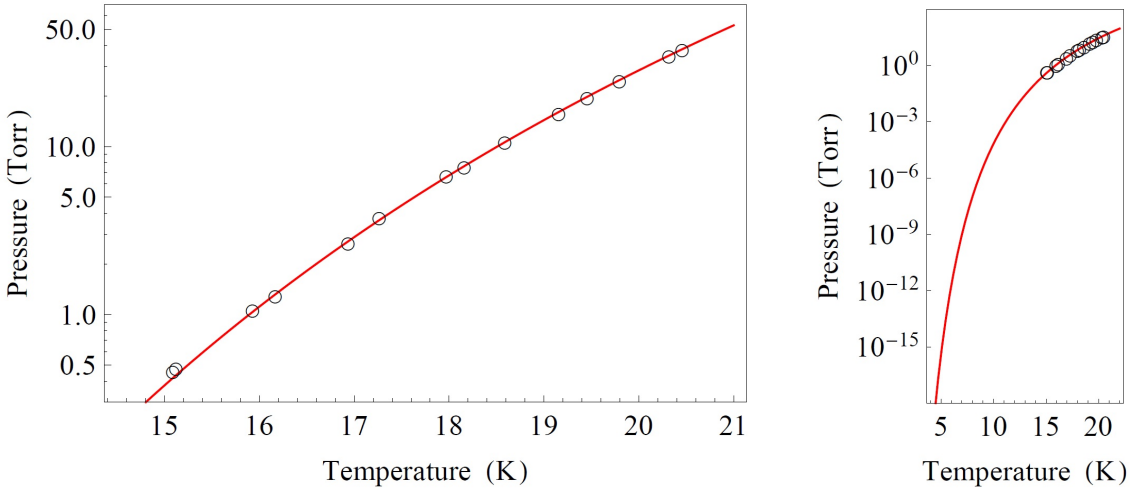

Figure 2.2: The sublimation pressure of Ne. Data are taken from Reference [29] and plotted as open circles. The red curve is a fit with the Clausius-Clapeyron equation.

2.2 Apparatus and Setup

The most important apparatus for producing the data presented in this dissertation is the cryostat. The Infrared Laboratories HD-3(8) model we use is a double-vessel liquid He cryostat that has a liquid N_2 capacity of 2.5 L and a liquid He capacity of 2.8 L (Figure 2.3). The liquid N_2 vessel cools down an aluminum shield that surrounds the liquid He vessel and protects it from any room temperature radiation. Due to the Stefan-Boltzmann law, the blackbody radiation is reduced by a factor of 200 from 300 K to 80 K. To cool down the liquid He vessel, we need to precool it by liquid N_2 in order to conserve liquid He. Since liquid He cannot stably exist at room temperature, the transfer of liquid He takes more caution and tools. The procedure for transferring liquid He from a commercial portable dewar to the cryostat is given in Appendix A.

The designed hold time of the cryostat with all ports closed and all supports in place is 36 hours. The actual hold time is, however, only about 8 hours due to the aging of the

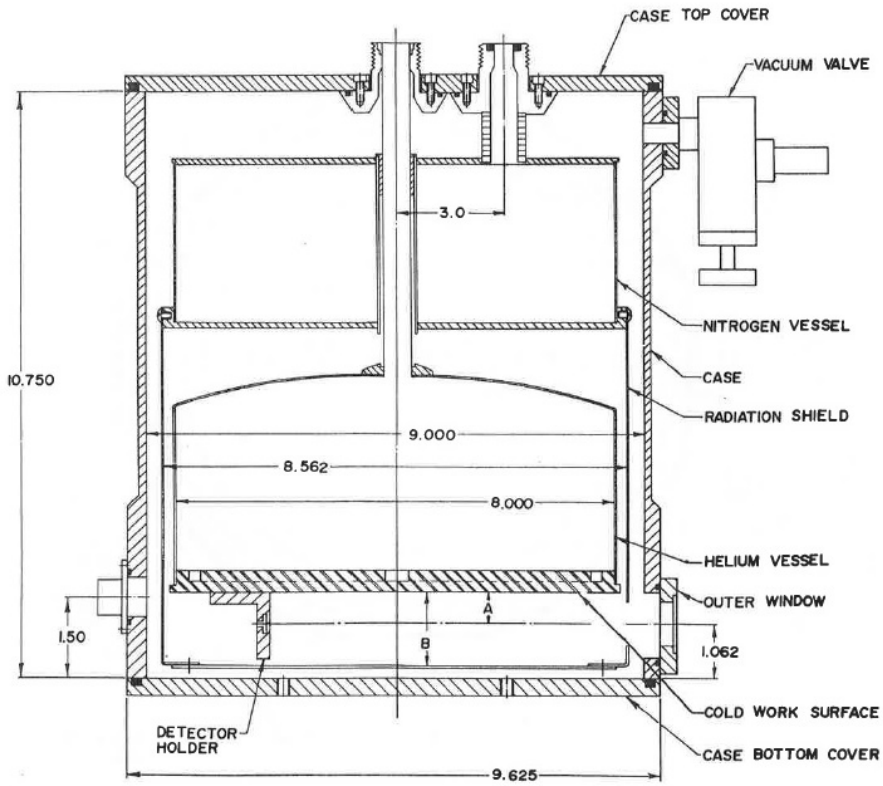

Figure 2.3: A sketch of the Infrared Laboratories HD-3(8) cryostat. This figure is reprinted from the manufacturer's catalog.

cryostat and additional heat load imparted to the liquid He. For spectroscopy and lifetimes studies, this hold time is still sufficient. For experiments that require a longer hold time, we can always refill the cryostat while maintaining the cold temperature (Appendix A).

The 4 K work surface inside the cryostat is the bottom of the liquid He vessel which has an area of about 300 cm^2. On the vacuum side, a copper substrate mount (Figure 2.4) is installed to hold the substrate vertically. The mount comes in two pieces. The first piece, or the base piece, establishes the conduction between the horizontal cold surface and the vertically oriented substrate. The contact between the cold surface and the base piece is improved by the low-vapor-pressure cryogenic grease (Apiezon N). The second piece, or the front piece, clamps the substrate against the vertical part of the base piece with indium wires used as the "glue". The front piece is often removed after the substrate has been securely installed for the sake of a larger aperture.

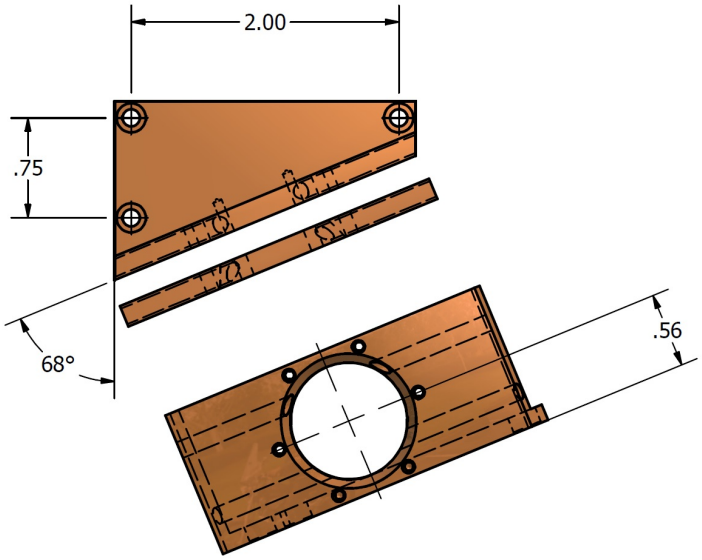

Figure 2.4: A sketch of the substrate mount. Image courtesy of T. O'Connor.

The substrates used for most of the times are sapphire windows because of sapphire's good transparency in the visible-ultraviolet range, its excellent thermal conductivity at low temperatures, and its sturdiness that allows for many thermal cycles between the room temperature and the liquid He temperature [30]. In comparison, fused-silica substrates could not reach a temperature low enough to freeze solid Ne under the current cooling scheme. CaF_2 substrates are also used from time to time for its good optical transparency, but CaF_2 is a fragile material that the substrates easily get cracked either at the installation stage or after only a few thermal cycles.

For spectroscopy and lifetime studies, we use 1 inch diameter, 0.5 cm thick sapphire substrates. These substrates are purchased from Thorlabs and cut in a way that the c-axis of the sapphire crystal is perpendicular to the substrate surface. The surface quality of the substrates is 60/40 scratch/dig. We also use sapphire with other shapes, including 1/2 inch diameter, 1 cm long cylinders and 3 cm each side, 0.3 cm thick square substrates. These more versatile pieces are purchased from Guild Optics and have the same cut and the surface quality. Before being installed in the cryostat, the substrates are washed in the ultrasonic cleaner followed by the acetone cleaning.

The temperature of the substrate is measured by the Lakeshore CX-1050-AA resistance temperature sensors and read out by the Lakeshore Model 330 temperature controller. We install two sensors on the substrate holder with one on each piece. When a sapphire substrate is installed, readings of the two sensors are different by less than 100 mK and are typically between 4.2 K and 4.7 K. Since the front piece is entirely cooled through its contact with the substrate, this implies that the substrate is sufficiently cooled for growing solid Ne.

The method of growing Yb/Ne samples is similar to the molecular beam epitaxy [31]. The Ne gas is depleted of H_2 and N_2 by a noble gas purifier (LDetek LDP1000) and depleted of H_2O by a liquid N_2 cooled charcoal trap. It then flows into a reservoir through a leak valve which controls the reservoir pressure. A 1/4 inch thick flexible stainless steel hose connects the output of the reservoir and a capillary tube feeding into the cryostat. The capillary tube points at the substrate 5 cm away from a nearly normal angle. Since the pressure of the reservoir is much higher than that in the cryostat, the Ne gas flow rate, and thus the solid Ne growth rate, has a linear dependence on the reservoir pressure.

The Yb atoms are deposited onto the substrate via an atomic beam generated by a home-made effusive oven with a titanium crucible (Figure 2.5). On the front end of the crucible, there is a nozzle from which the atomic beam emerges. On the rear end, there is a slot for a thermocouple used to monitor the temperature. The calculation of the Yb flux follows Reference [32]. In the molecular flow regime, the flux density of an effusive oven in the forward direction is

$$Q = \frac{a}{4\pi d^2} nv, \tag{2.1}$$

where a is the opening area of the oven, d is the distance between the oven and the observation point, n is the number density of the particles in the oven, and v is the mean velocity of particles in the beam. From the kinetic theory of gases, we have

$$n = \frac{p(T)}{k_{\mathrm{B}}T} \text{ and } v = \sqrt{\frac{3k_{\mathrm{B}}T}{M}}, \tag{2.2}$$

where $p(T)$ is the vapor pressure of the particles as a function of the temperature T, k_{B} is the Boltzmann constant, and M is the mass of the particle. The Yb flux can also be measured in the beam using the transverse beam fluorescence method [33]. The transition we use is $6s^2\ {}^1S_0 - 6s6p\ {}^1P_1$ at 398.9 nm in vacuum. The excitation light is obtained by frequency doubling a Ti:Al_2O_3 laser. The results of the two methods agree within a factor of a few.

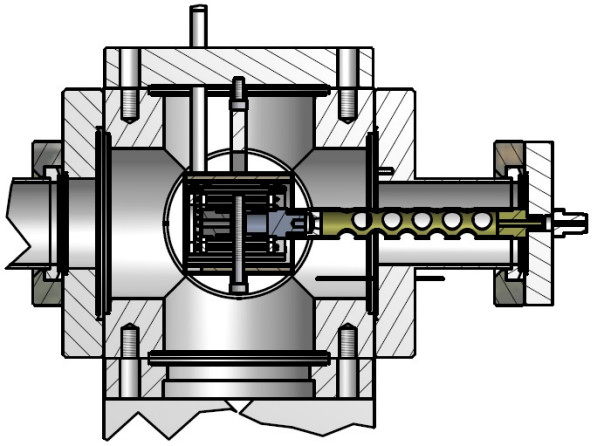

Figure 2.5: A sketch of the Yb oven. Image courtesy of T. O'Connor.

The Yb oven is connected to the cryostat in a way shown in Figure 2.6. There are four 1 inch diameter ports on the perimeter of the cryostat, one of which is connected to the oven by a 60 cm long beam line. The other three ports are covered with fused silica windows and used as viewports. Viewports A and B make a $\pi/8$ angle with the substrate normal and are used in the sample thickness measurement and the absorption studies. Viewport C makes a $3\pi/8$ angle with the substrate normal and is used in the emission studies to collect fluorescence light from the sample. This arrangement is based on the requirement that the substrate receives a large fraction of the Yb flux and at the same time the light beam for absorption studies also probes a large fraction of the sample.

2.3 Sample Growth

The thickness of the solid Ne samples is measured based on the thin-film interference principle [34]. A He-Ne laser is split up by a beam-splitter, with one beam shined through the

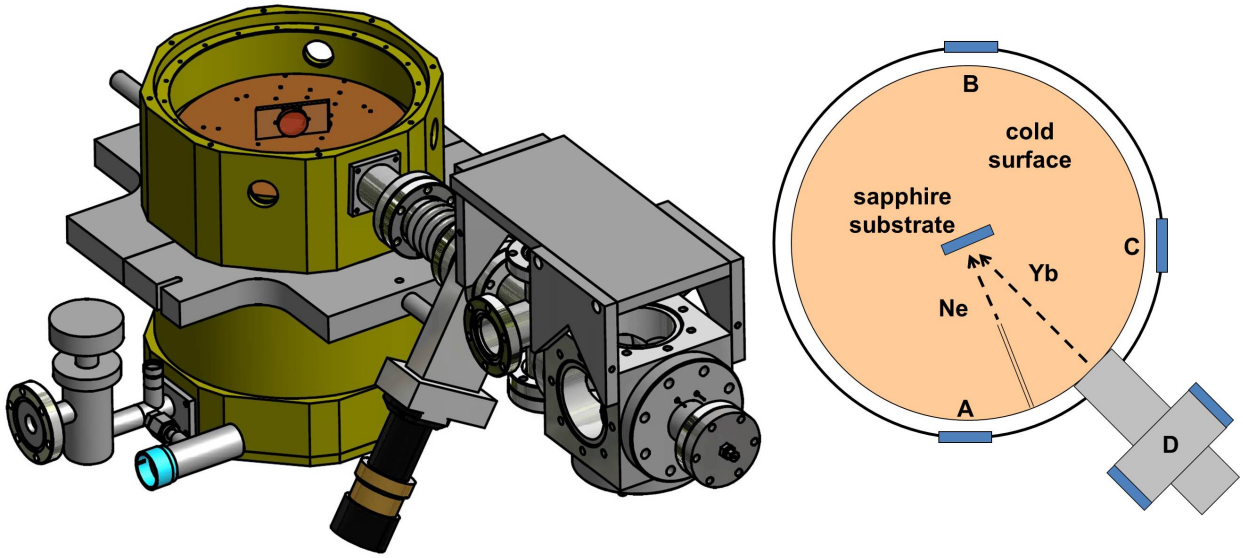

Figure 2.6: A sketch that shows the connection between the cryostat and the Yb beam line as well as the orientation of the cryostat ports with respect to the substrate normal. A, B, and C are three viewports covered with fused silica windows. D is a six-way cross where the Yb beam flux can be measured. Image courtesy of T. O'Connor.

growing solid Ne from viewport A to B in Figure 2.6 while the other used as a reference. If the substrate normal is parallel with $\overline{\text{AB}}$, then we can either detect the reflection at A or the transmission at B. The reflection detection is preferable since the interference fringes have a larger contrast. However, if the substrate is installed as in Figure 2.6, only the transmission detection is possible.

The power fluctuation of the He-Ne laser is canceled out by the reference beam, but the polarization and the frequency fluctuations are not. To deal with the polarization fluctuation, a linear polarizer or a polarization beam-splitter is added before the split point. Therefore a polarization fluctuation is converted into a power fluctuation. The frequency fluctuation mainly comes from the temperature fluctuation of the laser. To minimize this, we wait until the laser fully warms up and reaches a stable temperature.

Figure 2.7 shows a typical set of interference fringes using the reflection signal when the substrate normal is parallel with $\overline{\text{AB}}$. The oscillation of the signal is observed to have two components. The the fast oscillation corresponds to the growth of solid Ne on the front

surface of the substrate, while the slow oscillation corresponds to the growth on the back surface. The wavelength of the He-Ne laser is 632 nm, so each fringe roughly corresponds to a 300 nm thick layer. In total, this particular sample is about 30 μm thick. During the 8-hour long growth, the growth rate has been deliberately changed from about 3 μm/hr to 10 μm/hr to investigate its influence on the sample transparency. As can be seen from the figure, the contrast of the fringes roughly remains the same throughout the growth.

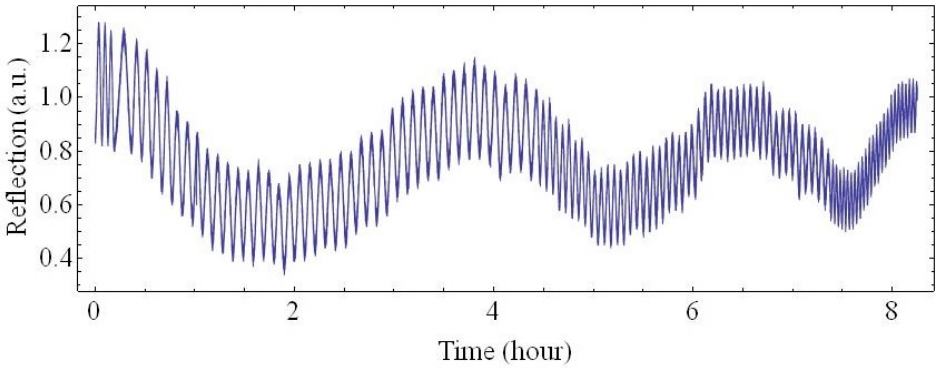

Figure 2.7: The thin-film interference fringes while growing a solid Ne sample.

To prepare a Yb/Ne sample, we first grow a layer of pure solid Ne by ramping up the reservoir pressure until the desired growth rate is reached. In order to maintain sample transparency, the initial ramp-up is very gentle which takes about an hour to reach 100 mTorr, which roughly corresponds to a solid Ne growth rate of 0.25 μm/hr. From that, it usually takes an hour to further get to 4 Torr (10 μm/hr) and another half hour to 20 Torr (50 μm/hr). The maximal growth rate we have achieved is about 100 μm/hr. However, at this rate the solid Ne sample may easily get cracked during the first hour of growth.

Once the desired solid Ne growth rate is reached, we open the gate valve on the Yb beam line to let Yb atoms deposit on the substrate simultaneously with the growing solid Ne matrix. After enough Yb atoms are collected in solid Ne, we close the gate valve and cut off the Ne supply to the reservoir. This way a final layer of solid Ne will grow on top of the Yb/Ne sample for about half an hour as the reservoir pressure decays.

2.4 Sample Parameters

For a thin-film sample, both the 3D and the 2D number densities n_3 and n_2 need to be specified. They are related through the sample thickness s, $n_2 = n_3 s$. The Yb 3D density $n_{3,\mathrm{Yb}}$ is most conveniently expressed as the Yb/Ne dilution factor $\xi = n_{3,\mathrm{Yb}}/n_{3,\mathrm{Ne}}$, where the Ne 3D density $n_{3,\mathrm{Ne}}$ is given in Table 2.1. The Yb 2D density $n_{2,\mathrm{Yb}}$ is related to the absorbance $A(\omega) = \ln(I_0(\omega)/I(\omega)) = n_{2,\mathrm{Yb}}\sigma^*(\omega)$, where $I_0(\omega)$ and $I(\omega)$ are the incident and transmitted intensities of the probe light at angular frequency ω, and $\sigma^*(\omega)$ is the absorption cross-section in solid Ne. We show in Section 3.3.5 that $\sigma^*(\omega_0) = \sigma(\omega_0)/W$, where $\sigma(\omega)$ is the cross-section in vacuum, ω_0 is the resonance frequency, and W is the broadening factor of the absorption linewidth. $\sigma(\omega_0) \equiv \sigma_0 = 3\lambda_0^2/2\pi$ where λ_0 is the resonance wavelength.

While growing Yb/Ne samples, ξ is adjusted by the Yb flux density Q_{Yb} and the Ne flux density Q_{Ne},

$$\xi = \frac{n_{3,\mathrm{Yb}}}{n_{3,\mathrm{Ne}}} = \frac{Q_{\mathrm{Yb}}}{Q_{\mathrm{Ne}}}. \tag{2.3}$$

Flux density Q is defined as the number of particles passing through a normal unit area per unit time, and therefore $Q = \mathrm{d}n_2/\mathrm{d}t$ where n_2 is the 2D density of a growing solid made of these particles. For Yb, we have

$$Q_{\mathrm{Yb}} = \frac{\mathrm{d}n_{2,\mathrm{Yb}}}{\mathrm{d}t} = \frac{1}{\sigma^*(\omega_0)}\frac{\partial A(\omega_0)}{\partial t} = \frac{W}{\sigma_0}\frac{\partial A(\omega_0)}{\partial t}, \tag{2.4}$$

where W and $\partial A(\omega_0)/\partial t$ can both be measured. For Ne, we have

$$Q_{\mathrm{Ne}} = \frac{\mathrm{d}n_{2,\mathrm{Ne}}}{\mathrm{d}t} = n_{3,\mathrm{Ne}}\frac{\mathrm{d}s_{\mathrm{Ne}}}{\mathrm{d}t}, \tag{2.5}$$

where $\mathrm{d}s_{\mathrm{Ne}}/\mathrm{d}t$ is the solid Ne growth rate which can also be measured using the method described previously. Therefore we have an expression for ξ all based on measurements,

$$\xi = \frac{Q_{\mathrm{Yb}}}{Q_{\mathrm{Ne}}} = \frac{W}{n_{3,\mathrm{Ne}}\sigma_0}\frac{\partial A(\omega_0)}{\partial t}\left(\frac{\mathrm{d}s_{\mathrm{Ne}}}{\mathrm{d}t}\right)^{-1}. \tag{2.6}$$

We empirically find that single Yb atoms are isolated in solid Ne only when $\xi < 5$ ppm at temperatures between 4.2 K and 4.7 K. When $\xi > 5$ ppm, the probability is significantly increased that Yb atoms find each other and form clusters in solid Ne. We typically grow samples with $\xi = 1$ ppm and $\mathrm{d}s_{\mathrm{Ne}}/\mathrm{d}t = 50\ \mu$m/hr. Under these conditions, $n_{3,\mathrm{Yb}} = 4.5{\times}10^{16}$ cm^{-3} and $Q_{\mathrm{Yb}} = 2.3 \times 10^{14}$ cm$^{-2} \cdot$ hr^{-1}. This Yb flux can be achieved by running the oven at about 620 K. The heat load due to the deposition of Ne and the blackbody radiation from the Yb oven increases the substrate temperature by less than 50 mK.

CHAPTER 3

SPECTROSCOPY OF YB IN SOLID NE

In this chapter, results on optical spectroscopy and laser excitation of Yb atoms in solid Ne are presented. Yb transitions in solid Ne are found to be mostly blue-shifted from their vacuum positions and broadened by a few orders of magnitude compared with their natural linewidth. The broadening is mainly due to the different impurity-lattice coupling when the impurity is in the lower and upper states. For inner-shell transitions of Yb, this effect is weaker because the valence electrons responsible for coupling with the Ne lattice do not directly participate in the transitions. Transitions are also split in solid Ne due to the broken spherical symmetry of the Yb trapping sites. To understand these observations, I will start with a brief review on the electronic structure of a neutral Yb atom in vacuum.

3.1 Electronic Structure of Yb

A neutral Yb atom has 70 electrons orbiting outside the nucleus. Its ground state is a non-degenerate $^1S_0$ from the electronic configuration [Xe]$4f^{14}6s^2$, and thus has zero electronic orbital and spin angular momenta. The Yb energy-level diagram (Figure 3.1) and electronic transitions share some similarities with alkaline earth atoms such as Ba. However, the Yb spectrum has richer features due to the $4f$ electrons unique to lanthanides.

The configurations of many low-lying states in Yb result from the elevation of a *single* electron. This electron can either be a $6s$ electron or a $4f$ electron. Configurations associated with the $6s$-electron elevation look like $4f^{14}nl6s$ or $4f^{14}6snl$, where $4f^{14}$ can be omitted for brevity and nl stands for the orbital the $6s$ electron is elevated to. The resultant states are described by terms and levels in the LS coupling scheme. Levels of this sort should be familiar since they are also found in alkaline earth atoms. For example, the $5d6s$ configuration contains $^3D_{1,2,3}$ and $^1D_2$ levels. A brief description of how the wave function of a term is constructed in the LS coupling scheme is given in Appendix B.

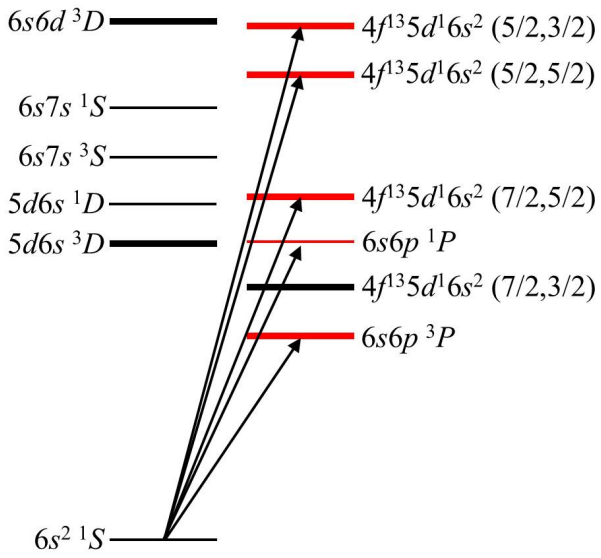

Figure 3.1: Low-lying terms and transitions of a neutral Yb atom. Upward arrows indicate allowed electric-dipole transitions from the ground level to five $J = 1$ levels belonging to different terms.

Configurations associated with the $4f$-electron elevation look like $4f^{13}nl6s^2$ or $4f^{13}6s^2nl$. For these configurations, the spin-orbit interaction of the individual electrons is stronger than the residual Coulomb interaction between two electrons. Therefore the jj coupling scheme gives a more appropriate description of the resultant states [35]. Since a full shell has zero orbital and spin angular momenta, $4f^{13}$ is equivalent to $4f$ in the consideration of angular momentum coupling. For example, the $4f^{13}6s^26p$ configuration, equivalent to $4f6s^26p$ or simply $4f6p$, contains four jj coupling terms with (j_1, j_2) equal to $(\frac{7}{2}, \frac{3}{2})$, $(\frac{7}{2}, \frac{1}{2})$, $(\frac{5}{2}, \frac{3}{2})$, and $(\frac{5}{2}, \frac{1}{2})$ respectively, and these four terms contain twelve levels in total.

Electric-dipole ($E1$) transitions in Yb follow the selection rule $\Delta l = \pm 1$ if a *single* electron jump is involved, where l is the orbital angular momentum of that electron [36]. Starting from the ground level $4f^{14}6s^2$, the allowed jumps with the least energies are $6s \rightarrow 6p$ and $4f \rightarrow 5d$. Note that the $4f \rightarrow 5d$ jump does not involve the valence $6s$ electrons, and both the initial and the final orbitals of the jumping electron are interior to the valence shell. A transition associated with this type of electron jump is called an inner-shell transition. In contrast, an outer-shell transition is associated with an electron jump in which either the

initial orbital or the final orbital of the jumping electron is exterior to the valence shell. Apparently, transitions with the $6s \rightarrow 6p$ jump are outer-shell transitions.

$E1$ transitions, either inner- or outer-shell, further follow the selection rule $\Delta J = 0, \pm 1$ and $J = 0 \nleftrightarrow 0$, where J is the total angular momentum of the atomic level [36]. Since the Yb ground level has $J = 0$, allowed transitions originating from it will end up only in levels with $J = 1$. The $4f^{14}6s6p$ configuration, as a result of the $6s \rightarrow 6p$ jump, contains four levels belonging to two LS terms: ${}^3P_{0,1,2}$ and ${}^1P_1$. The $4f^{13}5d6s^2$ configuration, as a result of the $4f \rightarrow 5d$ jump, contains twenty levels belonging to four jj terms: $(\frac{7}{2}, \frac{5}{2})_{1,2,3,4,5,6}$, $(\frac{7}{2}, \frac{3}{2})_{2,3,4,5}$, $(\frac{5}{2}, \frac{5}{2})_{0,1,2,3,4,5}$, and $(\frac{5}{2}, \frac{3}{2})_{1,2,3,4}$. Among them, only five levels have $J = 1$,

$$\overbrace{{}^3P_1,\ {}^1P_1}^{4f^{14}6s6p} \text{ and } \overbrace{\left(\frac{7}{2}, \frac{5}{2}\right)_1,\ \left(\frac{5}{2}, \frac{5}{2}\right)_1,\ \left(\frac{5}{2}, \frac{3}{2}\right)_1}^{4f^{13}5d6s^2}. \tag{3.1}$$

These five $E1$ transitions are indicated by upward arrows in Figure 3.1.

3.2 Absorption Spectroscopy

One way to verify whether we have successfully isolated individual Yb atoms in solid Ne is to perform absorption spectroscopy on the Yb/Ne samples. Optical absorption spectra of Yb in solid Ar, Kr and Xe have been reported previously [37], where the embedded Yb atoms exhibit broadened and shifted electronic transitions, similar to other group II atoms in solids [38]. However, limited by the instrumental resolution, the previous researchers did not further study the details of the Yb absorption bands. We have studied the absorption of Yb in solid Ne with progressively finer resolutions using both spectrometers and lasers. Therefore we are able to observe the dramatic difference in lineshape between inner- and outer-shell transitions. Usually the probe light is weak so that one essentially probes transitions only from the ground level. But with additional excitation, long-lived excited levels may be populated from which the transitions can be studied as well.

3.2.1 Results with Spectrometers

We first perform the traditional absorption spectroscopy using a broadband light source and a spectrometer. The light is fiber coupled to a collimator and shined through the sample from viewport A in Figure 2.6. Outside viewport B, the transmitted light is collected by a second collimator and fiber coupled to the spectrometer. Without the sample, the spectrum of the transmitted light is recorded as the reference. With the sample, any change in the spectrum of the transmitted light signals the absorption by the sample.

Two light sources from Ocean Optics are used, DT-2000-MINI and DH2000-DUV. They are both deuterium-tungsten lamps that cover wavelengths from 200 nm to 2500 nm, but DH2000-DUV is about 50 times brighter. Two optical spectrometers are used, Ocean Optics USB4000-UV-VIS and McPherson 225. The groove densities of their gratings are both 600 mm^{-1}. However, the resolution is 1.5 nm for the Ocean Optics and 0.03 nm for the McPherson due to the different entrance-slit size and the arm length. We usually pair the DT-2000-MINI lamp with the Ocean Optics spectrometer and the DH2000-DUV lamp with the McPherson spectrometer to get reasonable signal to noise ratio.

The Ocean Optics spectrometer module has a built-in camera to record spectra. It has a fixed camera frame that covers wavelengths from 200 nm to 1100 nm. The communication with the spectrometer is made via the software provided by Ocean Optics. For the McPherson spectrometer, we replace the exit slit assembly by a CCD line camera (Mightex TCE-1304-UW). Due to the 1.66 nm/mm dispersion at the exit, each camera frame covers only 40 nm. Therefore we shift the central wavelength of the spectrometer to select the desired wavelength windows. The central wavelength can be tuned from 200 nm to 600 nm. We have developed LabVIEW programs to extract data from the CCD camera.

An overview of the Yb absorption in solid Ne is obtained using the Ocean Optics spectrometer with 1.5 nm resolution. In Figure 3.2, the red curve shows the absorption spectrum with $n_{2,\text{Yb}} \sim 1 \times 10^{14}$ cm^{-1} [24], and the blue curve with $n_{2,\text{Yb}} \sim 2 \times 10^{15}$ cm^{-1}. Five absorption bands are observed and identified as Yb transitions from the ground level (Ta-

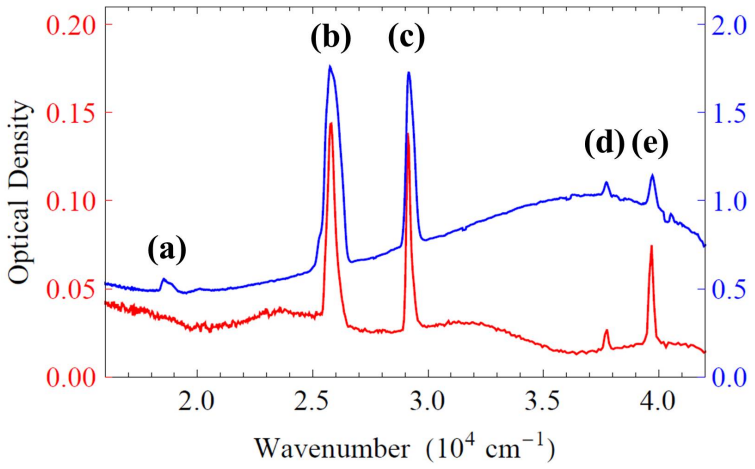

Figure 3.2: The absorption spectra of Yb atoms in solid Ne taken by the Ocean Optics spectrometer with 1.5 nm resolution. All absorption bands correspond to Yb transitions from the ground level. Two curves are the absorption signals with two different Yb densities.

ble 3.1). Compared to transitions in vacuum, the centers of absorption bands in solid Ne all get shifted to the high energy side by a few hundred to more than a thousand cm^{-1}. Band (a), identified as the relatively weak intercombination transition $6s^2\ {}^1S_0 - 6s6p\ {}^3P_1$, is not observable in the low density spectrum. Band (b) is used to calibrate the Yb density in the sample (Section 2.4). In the high density spectrum, the size of bands (b), (c), (d), and (e) is background limited and does not reflect the transition strength relative to that of band (a). The situation is worse for bands (d) and (e) than bands (a) and (b) because the broadband light contains fewer photons near 4.0×10^4 cm^{-1} than 2.5×10^4 cm^{-1}.

Table 3.1: The identification of the observed absorption bands of Yb atoms in solid Ne shown in Figure 3.2. All transitions are from the ground level $4f^{14}6s^2\ {}^1S_0$ to the levels below. ν is the transition frequency in vacuum, ν_a^* is the center of the absorption band in solid Ne, $\Delta\nu$ is the natural linewidth in vacuum, and $\Delta\nu_a^*$ is the width of the narrowest peak in the absorption band shown in Figure 3.3. ν, ν_a^*, $\nu_a^* - \nu$, $\Delta\nu$, and $\Delta\nu_a^*$ are in cm^{-1}. The uncertainties are 40 cm^{-1} for ν_a^*, and 10% for $\Delta\nu_a^*$.

Band	Level	ν	ν_a^*	$\nu_a^* - \nu$	$\Delta\nu$	$\Delta\nu_a^*$	$\Delta\nu_a^*/\Delta\nu$
(a)	$4f^{14}6s6p\ {}^3P_1$	17,992	18,510	+518	3.9×10^{-5}	270	6.9×10^6
(b)	$4f^{14}6s6p\ {}^1P_1$	25,068	25,760	+692	1.0×10^{-3}	120	1.2×10^5
(c)	$4f^{13}5d6s^2\ (\frac{7}{2},\frac{5}{2})_1$	28,857	29,140	+283	3.6×10^{-4}	5	1.1×10^4
(d)	$4f^{13}5d6s^2\ (\frac{5}{2},\frac{5}{2})_1$	37,415	37,730	+315	4.8×10^{-4}	6	1.0×10^4
(e)	$4f^{13}5d6s^2\ (\frac{5}{2},\frac{3}{2})_1$	38,422	39,670	+1,248		30	

Note that the five absorption bands exactly correspond to the five transitions discussed in Section 3.1. Bands (a) and (b) are outer-shell transitions with the $6s \rightarrow 6p$ jump, while bands (c), (d), and (e) are inner-shell transitions with the $4f \rightarrow 5d$ jump. Under the Ocean Optics spectrometer, the five bands do not seem very different as they all appear to be single peaked. However, the widths of bands (d) and (e) are limited by the resolution (240 cm^{-1} at 4×10^4 cm^{-1}). To study their detailed structure and find out their intrinsic linewidth, we improve the resolution by using the McPherson spectrometer.

Figure 3.3 shows separately the lineshape of the five absorption bands with 0.03 nm resolution. The difference between inner- and outer-shell transitions is readily seen. The width of the narrowest peak in bands (a) and (b) remains a few hundred cm^{-1} while the width of the narrowest peaks in bands (c), (d), and (e) ranges from a few to a few ten cm^{-1} (Table 3.1). With narrower linewidth, the lineshapes of bands (c), (d), and (e) reveal more splitting than (a) and (b). I will explain the broadening and the splitting in the following two sections. But before that I will show the result of laser spectroscopy on band (d) due to its particularly narrow linewidth and relatively simple lineshape.

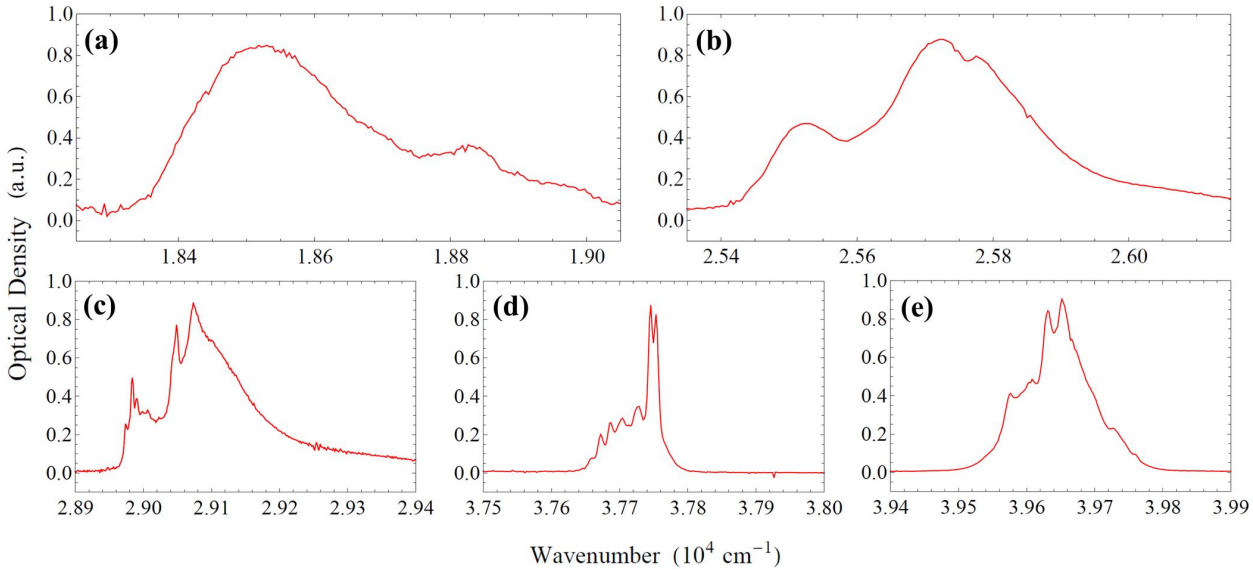

Figure 3.3: The absorption spectra of Yb atoms in solid Ne taken by the McPherson spectrometer with 0.03 nm resolution. All the panels use the same wavenumber scale and the absorption strengths are separately normalized.

3.2.2 Results with Lasers

In Figure 3.3, the width of the two narrow peaks on the high wavenumber side in band (d) is about 5 cm^{-1}, comparable to the resolution of the McPherson spectrometer (4.3 cm^{-1} at 3.8×10^4 cm^{-1}). Therefore to find out the intrinsic width of the peaks in band (d), a laser with narrow linewidth is needed as the probe light for the absorption study.

The laser we use is a frequency-doubled optical parametric oscillator (OPO) from Continuum (Sunlite EX). It is pumped by a third harmonic pulsed Nd:YAG laser (Powerlite DLS), and its signal output is doubled by a second-harmonic generator (Inrad AT-II). Each pulse contains about 1 mJ energy which is attenuated by four orders of magnitude to avoid heating the samples. The linewidth of the ultraviolet photons is about 1 GHz, and the wavelength is scanned with an interval of 5×10^{-4} nm or about 2 GHz in frequency. Therefore the resolution of this laser spectroscopy is about 2.5 GHz. The ultraviolet laser is then split into a probe beam and a reference beam. The probe beam is shined through the sample and its transmission is detected by a photodiode. The reference beam propagates outside the cryostat and is detected by a second photodiode. As the wavelength is scanned, the power ratio of the probe beam to the reference beam gives the transmission spectrum.

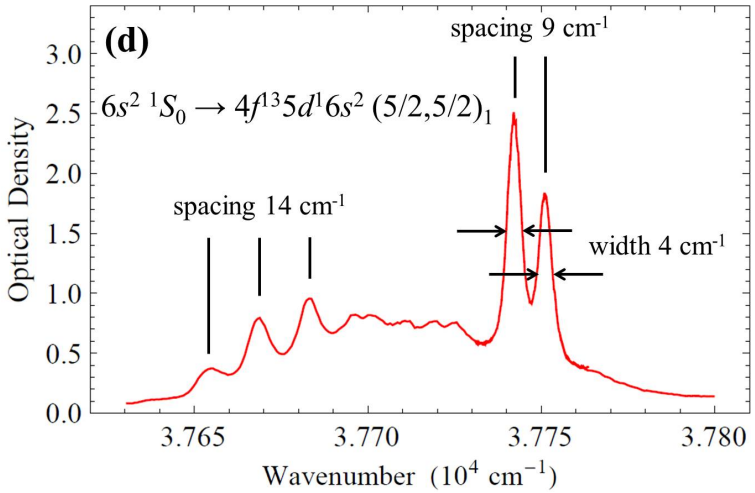

Figure 3.4: The intrinsic lineshape of absorption band (d) in Figures 3.2 and 3.3 probed by the frequency-doubled OPO laser. The spectrum has a resolution of about 2.5 GHz. Both peaks on the high wavenumber side have a width of 4 cm^{-1} or 120 GHz.

Figure 3.4 shows the lineshape of the absorption band (d) with 2.5 GHz resolution. Since the spectrum is no longer resolution limited, the width of the two peaks on the high wavenumber side, 4 cm^{-1} or 120 GHz, represents the narrowest linewidth of Yb transitions in solid Ne . Three peaks on the low wavenumber side have a larger width and are regularly spaced by 14 cm^{-1}. It is tempting to think that they are the phonon sidebands while the two narrow peaks are the zero phonon lines. However, in the absorption mode, the phonon sidebands should appear on the high wavenumber side of the zero phonon line(s).

3.3 Linewidth Broadening Mechanism

We have seen that the widths of the peaks in different Yb absorption bands in solid Ne vary from a few cm^{-1} to a few hundred cm^{-1}, which are broadened from their natural linewidths by four to almost seven orders of magnitude. We would like to understand two things: (1) whether the linewidth broadening is homogeneous or inhomogeneous; (2) what mechanism causes such a broad linewidth and the variation among different transitions.

3.3.1 Homogeneous Broadening

The first question can be answered by doing a hole-burning experiment [39]. In a hole-burning experiment, a strong light with a narrow linewidth compared to the observed atomic linewidth resonantly pumps the atoms out of the equilibrium state. A weak light then probes the lineshape of the atomic transition. If the broadening is inhomogeneous, then the pump light will resonate with only a small class of atoms and thus burn a narrow hole on the lineshape measured by the probe light. Whereas for homogeneous broadening, the lineshape remains the same with, however, a reduced intensity.

We choose to study absorption band (b), the center of which is at 388 nm in solid Ne [24]. The 388 nm laser is obtained by frequency doubling the Ti:Al_3O_3 laser (Sirah Matisse TS) using a LiB_3O_5 crystal and a cavity. The resultant linewidth is about 1 MHz, sufficiently

narrow compared to the atomic linewidth in solid Ne (a few THz). The power of the Ti:Al_3O_3 laser at 776 nm is about 1 W when pumped by the 10 W Nd:YAG laser (Sirah Millennia). The power of the 388 nm laser is about 5 mW and the beam width is expanded to 1 cm, wider than the probe beam. In this experiment, we continue to use the weak broadband lamp and the Ocean Optics spectrometer to probe the absorption lineshape.

In Figure 3.5, the red curve is the same spectrum with low Yb density as in Figure 3.2, and the blue curve is the steady-state spectrum when the 388 nm laser is on. When the sample is excited by the 388 nm laser, the absorption bands (b), (c), (d), and (e) almost disappear, which implies that the Yb atoms are depleted from the ground level. In the meantime, new absorption bands appear, among which the strongest absorption band (f) is identified as the $6s6p\ ^3P_0 - 6p^2\ ^3P_1$ transition. This indicates that the 388 nm laser can efficiently shelve the Yb population from $6s^2\ ^1S_0$ to the metastable $6s6p\ ^3P_0$. This population transfer is only possible if the narrow linewidth laser interacts with most of the atoms, which shows that the broadening is homogeneous, at least for this transition.

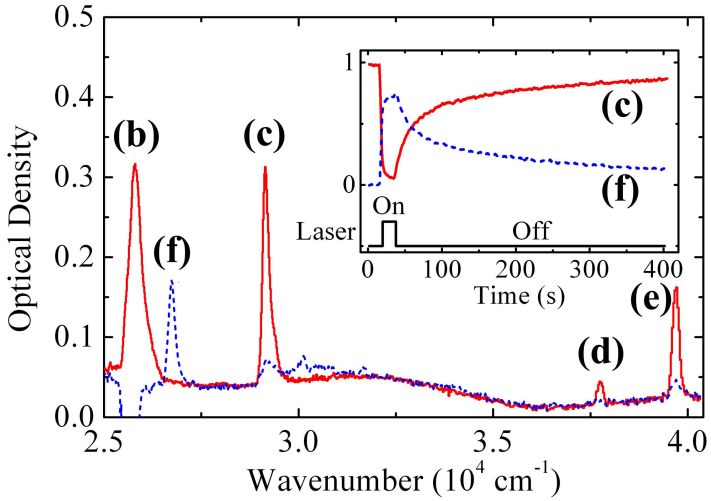

Figure 3.5: The absorption spectra of Yb in solid Ne taken by the Ocean Optics spectrometer with the 388 nm laser off (red solid) and on (blue dashed). Upon laser excitation, the original absorption bands all disappear while a new band (f) appears which corresponds to the $6s6p\ ^3P_0 - 6p^2\ ^3P_1$ transition. Inset: the evolution of the areas of absorption bands (c) (red solid) and (f) (blue dashed) as the excitation laser is switched on and off. This figure is reprinted with permission from a published work by C.-Y. Xu *et al.* in *Phys. Rev. Lett.* **107**, 093001 (2011). Copyright © 2011 by American Physical Society

3.3.2 Intersystem Crossing

The entire population-transfer process can be seen from the inset of Figure 3.5, where the evolution of the total area of bands (c) and (f) is plotted. After the 388 nm laser is turned on, band (c) disappears and band (f) appears within a few seconds. After the 388 nm laser is turned off, band (c) reappears and band (f) disappears in a few minutes. While the latter dynamics originates from the slow decay of the metastable $6s6p\ ^3P_0$ back to $6s^2\ ^1S_0$, the former indicates an unusually fast transfer from $6s6p\ ^1P_1$ to $6s6p\ ^3P_0$.

In vacuum, $6s6p\ ^1P_1$ only decays to $6s6p\ ^3P_0$ via $5d6s\ ^3D_1$. The decay rate of $5d6s\ ^3D_1 \leftarrow 6s6p\ ^1P_1$ is about 10 s^{-1} and that of $6s^2\ ^1S_0 \leftarrow 6s6p\ ^1P_1$ is about 2×10^8 s^{-1}. Therefore the branching ratio of $5d6s\ ^3D_1 \leftarrow 6s6p\ ^1P_1$ is about 5×10^{-8}. In the next step, $6s6p\ ^3P_0 \leftarrow 5d6s\ ^3D_1$ is the dominant decay channel of $5d6s\ ^3D_1$ with a branching ratio of about 0.6. Therefore the total branching ratio of $6s6p\ ^3P_0 \leftarrow 6s6p\ ^1P_1$ is about 3×10^{-8}.

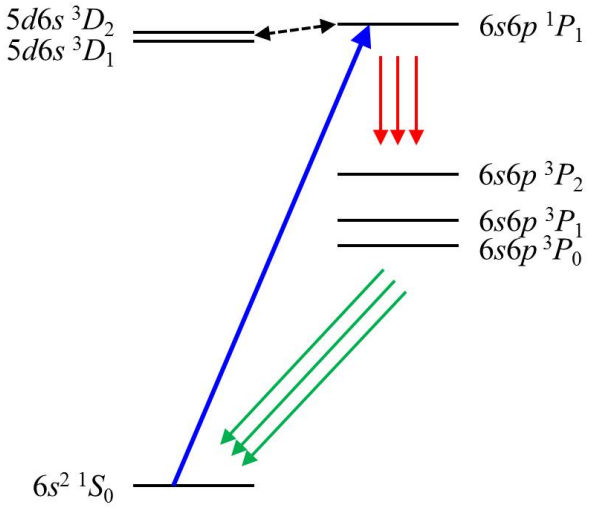

Figure 3.6: Yb atoms in solid Ne are efficiently transferred from $6s^2\ ^1S_0$ to $6s6p\ ^3P_0$ upon the excitation to $6s6p\ ^1P_1$. The $6s6p\ ^3P_{0,1,2} \leftarrow 6s6p\ ^1P_1$ decay is induced by the Stark mixing between $5d6s\ ^3D_{1,2}$ and $6s6p\ ^1P_1$ due to the crystal field. In particular, the admixture of $5d6s\ ^3D_1$ in $6s6p\ ^1P_1$ gives an enhanced the branching ratio of $6s6p\ ^3P_0 \leftarrow 6s6p\ ^1P_1$.

The cause for the enhanced intersystem crossing from the singlet to the triplet in solid Ne is the Stark mixing between $5d6s\ ^3D_{1,2}$ and $6s6p\ ^1P_1$ due to the crystal field (Figure 3.6). In particular, the admixture of $5d6s\ ^3D_1$ in $6s6p\ ^1P_1$ gives rise to the direct decay $6s6p\ ^3P_0 \leftarrow$

$6s6p\ ^1P_1$. The mixing coefficient between $5d6s\ ^3D_1$ and $6s6p\ ^1P_1$ is difficult to estimate because we do not know their relative energies in solid Ne (see Appendix C for a calculation using energies of free Yb). But suppose the mixing coefficient is 0.1, with which $6s6p\ ^1P_1$ is still thought to be reasonably pure. Since the decay rate of $6s6p\ ^3P_0 \leftarrow 5d6s\ ^3D_1$ is about $2 \times 10^6\ \mathrm{s}^{-1}$, the induced rate of $6s6p\ ^3P_0 \leftarrow 6s6p\ ^1P_1$ is about $2 \times 10^4\ \mathrm{s}^{-1}$. Therefore the induced branching ratio of $6s6p\ ^3P_0 \leftarrow 6s6p\ ^1P_1$ is about 10^{-4}, enhanced by 3×10^3.

The Stark mixing between $5d6s\ ^3D_{1,2}$ and $6s6p\ ^1P_1$ also causes $6s6p\ ^3P_{1,2}$ to be populated. Together with $6s6p\ ^3P_0$, their spontaneous decays to $6s^2\ ^1S_0$ constitute most of the observed green fluorescence when the sample is excited by the 388 nm laser (Figure 3.7). The laser induced fluorescence spectroscopy is discussed in Section 3.5. The transfer $6s^2\ ^1S_0 \rightarrow 6s6p\ ^3P_0$ and the evolution of the $6s^2\ ^1P_1$ and $6s^2\ ^3P_{1,2}$ populations are analyzed in Appendix D using rate equations.

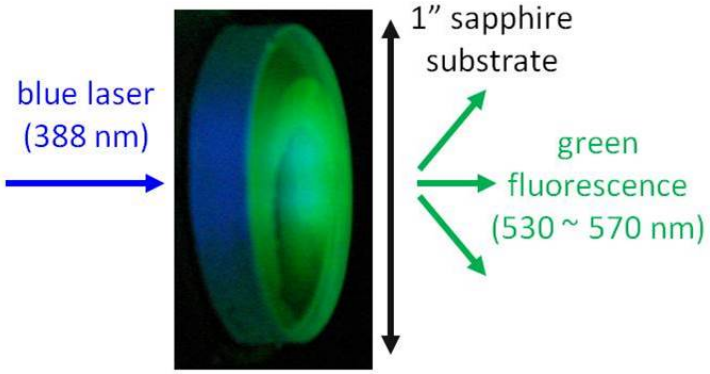

Figure 3.7: A picture of a Yb/Ne sample grown on the sapphire substrate when excited by the 388 nm laser. The strong green fluorescence is attributed to the spontaneous decays of $6s6p\ ^3P_{0,1,2}$ and those of other excited levels that happen to fall in this wavelength range.

3.3.3 Phonon Dephasing

So far, we have answered the first question, raised at the beginning of Section 3.3, that the Yb transitions in solid Ne are homogeneously broadened. This suggests that the difference in optical properties of Yb atoms due to the different trapping sites in solid Ne is negligible compared with the homogeneous mechanisms. The most obvious cause for homogeneous

broadening is the reduced lifetime in accordance with the uncertainty principle. The reduced lifetime could be caused by some type of collisions or "pressure" in a solid matrix [40]. Since the linewidth is broadened by several orders of magnitude, the lifetime has to be reduced by the same amount. However, as will be seen in Chapter 4, the lifetimes of excited levels in solid Ne remain within the same order of magnitude as the vacuum lifetimes. Therefore this mechanism is not the dominant contribution to the observed linewidth broadening.

Another candidate for homogeneous broadening in solids is the thermal broadening due to phonon dephasing. The physical picture of this mechanism is that the interaction between the impurity and the phonons in a crystal randomly shifts the phase of the excited state of the impurity, and therefore although the excited-state lifetime remains unchanged, a phase decoherence of the excited state is induced which results in a linewidth broadening.

For an isolated impurity in a crystal, the theory [41] considers the following Hamiltonian that describes the coupling between a two-level impurity and a phonon field

$$\mathscr{H}_{\text{imp+ph}} = |\text{g}\rangle\langle\text{g}|\mathscr{H}_{\text{ph}}^{\text{g}} + |\text{e}\rangle\langle\text{e}|\mathscr{H}_{\text{ph}}^{\text{e}} = \mathscr{H}_{\text{ph}}^{\text{g}} + |\text{e}\rangle\langle\text{e}|(\mathscr{H}_{\text{ph}}^{\text{e}} - \mathscr{H}_{\text{ph}}^{\text{g}}), \tag{3.2}$$

where $|\text{g}\rangle$ and $|\text{e}\rangle$ are the ground and excited states of the impurity, and $\mathscr{H}_{\text{ph}}^{\text{g}}$ and $\mathscr{H}_{\text{ph}}^{\text{e}}$ are the phonon Hamiltonians when the impurity is in the ground and excited states. $\mathscr{H}_{\text{ph}}^{\text{e}} - \mathscr{H}_{\text{ph}}^{\text{g}}$ equals the difference of the potential energy surfaces of the impurity-lattice system V_{g} and V_{e} when the impurity is in the ground and excited states. $V_{\text{e}} - V_{\text{g}}$ can be expanded in terms of a strain field, and α is the dimensionless coefficient of the quadratic term.

The optical absorption lineshape is given by

$$I(\omega) \propto \int_{-\infty}^{\infty} \mathrm{d}t e^{i\omega t} e^{-|t|/2\tau} \langle \mathscr{D}(t)\mathscr{D}(0)\rangle, \tag{3.3}$$

where τ is the excited-state lifetime, $\langle\cdots\rangle$ stands for the average in the canonical ensemble, and $\mathscr{D}(t) = e^{i\mathscr{H}t/\hbar}\mathscr{D}e^{-i\mathscr{H}t/\hbar}$ is the time-dependent electric-dipole operator. The calculation of the ensemble average is quite lengthy and requires the analysis of a few types of

Feynman diagrams. The result is that the lineshape is a Lorentzian, and the linewidth at low temperatures, where $n(\omega) = (e^{\hbar\omega/k_{\mathrm{B}}T} - 1)^{-1} \ll 1$, is

$$\Delta\omega^* = \frac{1}{4\pi^2}\int_0^\infty \mathrm{d}\omega \frac{n(\omega)(n(\omega)+1)D^2(\omega)}{(1-\alpha K(\omega))^2 + \alpha^2 D^2(\omega)}, \tag{3.4}$$

where $D(\omega)$ is the phonon density of states and $K(\omega) = (2/\pi)\int_0^\infty \mathrm{d}\nu D(\nu)\nu/(\omega^2 - \nu^2)$.

In a solid Ne matrix, only acoustic phonons are present. Their density of states under the Debye approximation is $n(\omega) = (3\pi/2)(\omega/\omega_{\mathrm{D}})^3$ for $\omega < \omega_{\mathrm{D}}$, where $\hbar\omega_{\mathrm{D}} = k_{\mathrm{B}}T_{\mathrm{D}}$ and T_{D} is the Debye temperature. Therefore the linewidth becomes

$$\frac{\Delta\omega^*}{\omega_{\mathrm{D}}} = \frac{9}{4}\left(\frac{\alpha}{1+\alpha}\right)^2\left(\frac{T}{T_{\mathrm{D}}}\right)^7 \int_0^{T_{\mathrm{D}}/T} \mathrm{d}x \frac{x^6 e^x}{(e^x-1)^2}, \tag{3.5}$$

when $T \ll T_{\mathrm{D}}$, which displays a T^7 dependence [42]. The strong temperature dependence originates from the fact that acoustic phonons are very soft thermal excitations of the lattice vibration and their density of states increases rapidly as the lattice gets hotter.

Our experiments fall in the low temperature regime because the mean Debye temperature of solid Ne is 63 K [22]. We can change the temperature of the Yb/Ne samples between 3 K and 5 K. If the phonon dephasing theory is the dominant mechanism, we should observe a factor of 36 change in linewidth. However, we find that the lineshape of bands (b) and (d) hardly changes even using the McPherson spectrometers. Therefore the phonon dephasing mechanism is not the dominant cause for the observed homogeneous broadening either.

3.3.4 Reflection Principle

The failure of using the phonon dephasing theory to explain the broadening of Yb transitions in solid Ne lies in the fact that the theory only applies to the broadening of the zero-phonon line. For matrix isolated atoms, the zero-phonon line is weak or absent due to the low Franck-Condon factor for the $n = 0 \leftrightarrow 0$ transition [4], where n is the quantum number of the phonon state. What we have observed is, instead, transitions of the impurity atom

with simultaneous excitation of local phonons due to the different potential energy surfaces of the impurity-lattice system when the impurity is in the ground and exited states. For example, the ground state of the group I and II atoms has a spherical symmetry and interacts isotropically with the matrix. But in the excited state, the electron cloud is usually stretched, which leads to an anisotropic interaction. This idea was first realized by Lax [5], and when applied to molecules, it helps understand the lineshape of photodissociation, where it is known as the reflection principle [43].

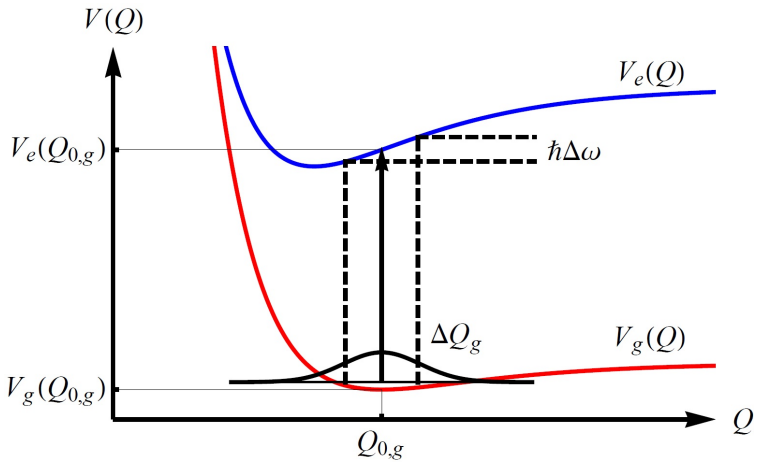

Figure 3.8: A sketch of the reflection principle that can explain the broad linewidth of Yb transitions in solid Ne. The interaction between the impurity and the lattice is described by two potential energy surfaces when the impurity is in the ground and excited states. When the impurity makes a vertical transition, the spread of the ground-state wave-function is reflected by the slope of the excited-state potential curve into a spread in the energy space.

Let $V_{\mathrm{g}}(Q)$ and $V_{\mathrm{e}}(Q)$ be the potential energy surfaces for the impurity-lattice system when the impurity is in the ground and excited states, where Q is the configuration coordinate that collectively describes the the lattice vibration (Figure 3.8). To simplify the problem, let us assume that the impurity makes a transition to a high vibrational level of the final state. Then the process can be treated semiclassically, i.e., the initial state is treated quantum mechanically and the final state is treated classical mechanically [5]. For absorption, only the lowest vibrational level of the ground state is populated since $T \ll T_{\mathrm{D}}$. The impurity transition is vertical because the lattice moves much slower than the electron. The electron ends up in a segment on the excited-state potential surface rather than on specific vibrational

levels. Therefore the absorption lineshape can be calculated from the ground-state wave-function of the electron, which has a linewidth

$$\Delta\omega^* = \frac{1}{\hbar}\frac{\mathrm{d}V_\mathrm{e}}{\mathrm{d}Q}\bigg|_{Q_{0,\mathrm{g}}} \Delta Q_\mathrm{g}, \tag{3.6}$$

where ΔQ_g is the width of the ground-state wave-function and $Q_{0,\mathrm{g}}$ is the equilibrium position in the ground state.

This mechanism qualitatively agrees our observations in a few ways. First, it is homogeneous since the transition of every single atom is broadened. Second, it is independent of temperature since it originates from the zero-point spread of the ground-state wave-function as a quantum mechanical effect. Third, it explains why inner-shell transitions are narrower than outer-shell transitions. For an inner-shell transition, the two potential energy surfaces are more horizontally aligned because the valence electrons which are responsible for coupling with the lattice do not directly participate in the transition. Therefore the impurity transition can land in a segment on the excited-state potential energy surface where the slope is relatively gentle, which leads to a smaller spread in energy.

Quantitatively, we can estimate the linewidth using the pair potential between Yb and Ne atoms to approximate the potential energy surfaces between Yb and the Ne lattice. These pair potentials have been calculated [44] in terms of the Morse function

$$v(Q) = v_0\left(1 - e^{-(Q-Q_0)/w}\right)^2, \tag{3.7}$$

where v_0 is the well depth, w is the well width, and Q_0 is the equilibrium position. Then the potential energy surfaces are roughly $V_{\mathrm{g,e}}(Q) = Nv_{\mathrm{g,e}}(Q)$, where $N = 12$ is the number of nearest Ne atoms of the Yb impurity. Let us look at the linewidth of the $6s^2\ {}^1S_0 - 6s6p\ {}^1P_1$ transition as an example. For the ground state, $v_{0,\mathrm{g}} = 14.7\ \mathrm{cm}^{-1}$, $w_\mathrm{g} = 0.909$ Å, $r_{0,\mathrm{g}} = 5.23$ Å, and $\Delta Q_\mathrm{g} \sim w_\mathrm{g}$. For the excited state, $v_{0,\mathrm{e}} = 43.9\ \mathrm{cm}^{-1}$, $w_\mathrm{e} = 0.909$ Å, and $r_{0,\mathrm{e}} = 4.67$ Å. In the end, we get $\Delta\omega^* = 262\ \mathrm{cm}^{-1}$ which is order of magnitude correct.

3.3.5 Optical Bloch Equations

From the previous discussion, we know that the linewidth broadening is homogeneous and is independent of the lifetime of the excited state. Therefore in order to correctly describe the atom-photon interaction, we need to modify the optical Bloch equations accordingly. For a two-level system in a free atom, these equations are, see Equation (7.67) in Reference [39],

$$\begin{cases} \dfrac{\mathrm{d}u}{\mathrm{d}t} = (\omega - \omega_0)v - \dfrac{\Gamma}{2}u \\ \dfrac{\mathrm{d}v}{\mathrm{d}t} = -(\omega - \omega_0)u + \omega_\mathrm{R} w - \dfrac{\Gamma}{2}v \\ \dfrac{\mathrm{d}w}{\mathrm{d}t} = -\omega_\mathrm{R} v - \Gamma(w - 1) \end{cases}, \tag{3.8}$$

where u, v, and w are the coherences and the population difference between the ground and excited states, ω is the angular frequency of the probe light, ω_0 is the resonance angular frequency, Γ is the spontaneous emission rate of the excited state, and ω_R is the Rabi frequency associated with the probe light. To incorporate additional broadening that does not reduce the excited state lifetime, we simply add decoherence terms only to the u- and v-equations

$$\begin{cases} \dfrac{\mathrm{d}u^*}{\mathrm{d}t} = (\omega - \omega_0)v^* - \dfrac{\Gamma}{2}u^* - \dfrac{\Gamma_\mathrm{d}}{2}u^* \\ \dfrac{\mathrm{d}v^*}{\mathrm{d}t} = -(\omega - \omega_0)u^* + \omega_\mathrm{R} w^* - \dfrac{\Gamma}{2}v^* - \dfrac{\Gamma_\mathrm{d}}{2}v^* \\ \dfrac{\mathrm{d}w^*}{\mathrm{d}t} = -\omega_\mathrm{R} v^* - \Gamma(w^* - 1) \end{cases}, \tag{3.9}$$

where Γ_d is the decoherence rate. The steady-state solution to the modified equations is

$$w^* = \frac{(\omega - \omega_0)^2 + (\Gamma_\mathrm{d}/\Gamma + 1)^2\Gamma^2/4}{(\omega - \omega_0)^2 + (\Gamma_\mathrm{d}/\Gamma + 1)^2\Gamma^2/4 + (\Gamma_\mathrm{d}/\Gamma + 1)\omega_\mathrm{R}^2/2}, \tag{3.10}$$

which, using the same derivation that leads to Equation (7.75) – (7.77) in Reference [39], leads to the modified absorption cross-section

$$\sigma^*(\omega) = \sigma_0 \frac{(\Gamma_\mathrm{d}/\Gamma + 1)\Gamma^2/4}{(\omega - \omega_0)^2 + (\Gamma_\mathrm{d}/\Gamma + 1)^2\Gamma^2/4}. \tag{3.11}$$

As we can see, the linewidth scales as $\Delta\omega^* = W\Delta\omega$, where $W = \Gamma_\mathrm{d}/\Gamma + 1$. At the same time, $\sigma^*(\omega_0) = \sigma(\omega_0)/W$ so that the integral $\int \sigma^{(*)}(\omega)\mathrm{d}\omega = \pi\sigma_0\Gamma/2$ remains the same. As a result, the saturation intensity scales as $I^*_\mathrm{sat} = WI_\mathrm{sat}$ since $I^{(*)}_\mathrm{sat} = \hbar\omega_0\Gamma/2\sigma^{(*)}(\omega_0)$.

3.4 Level Splitting Mechanism

Besides the significantly broadened linewidth of Yb transitions in solid Ne, another feature seen from Figure 3.3 is that one absorption band which corresponds to a single allowed transition in vacuum splits into multiple peaks. In this section, we utilize the group theory to analyze the splitting of atomic transitions in solids [45]. Although this approach cannot predict the size of the splitting, it accurately determines the number of splitting based on the symmetry of the trapping site.

3.4.1 Group Theoretical Approach

An atom in vacuum enjoys the symmetry of the full 3D rotation group SO(3). The energy levels are thus described by its irreducible representations $\mathscr{D}^{(j)}$, where $j \in \mathbb{N}$ is the angular momentum of the representation. The dimension of the representation $\mathscr{D}^{(j)}$ is $2j + 1$ which determines the degeneracy of the described level. When an atom is located in a crystal, the crystal field of the trapping site destroys the isotropy of free space. Thus the symmetry group is reduced to some finite group of rotation, which allows the originally irreducible representations $\mathscr{D}^{(j)}$ to be reduced with respect to the finite group. This reduction in the dimensionality of the irreducible representations causes the degeneracy associated with complete rotational symmetry to be lifted.

Since the five absorption bands all correspond to $J = 0 \to 1$ transitions, let us study how $J = 0, 1$ levels split. Given a point group that describes the symmetry of the trapping site, we work out the characters of the conjugate classes in both its own irreducible representations and $\mathscr{D}^{(j)}$. As an example, Table 3.2 shows the character table of the octahedral group

O comprised of 24 proper rotations, where $\mathscr{A}_1$, $\mathscr{A}_2$, $\mathscr{E}$, $\mathscr{T}_1$, and $\mathscr{T}_2$ are its five irreducible representations. The decomposition of $\mathscr{D}^{(j)}$ is determined by the decomposition formula

$$\mathscr{R} = \sum_i^{\oplus} n_i \mathscr{R}_i, \quad n_i = \frac{1}{N} \sum_k N_k \chi_{\mathscr{R}_i}(\mathscr{C}_k) \chi_{\mathscr{R}}(\mathscr{C}_k), \tag{3.12}$$

where $\mathscr{R}$ ($\mathscr{R}_i$) stands for the (ir)reducible representation, N is the number of group elements, N_k is the number of group elements in the class $\mathscr{C}_k$, and $\chi_{\mathscr{R}}(\mathscr{C})$ is the character of the class $\mathscr{C}$ in the representation $\mathscr{R}$. The result for $\mathscr{D}^{(j)}$ ($j = 0, 1, 2, 3$) is also given in Table 3.2.

Table 3.2: The character table of the octahedral group O comprised of only proper rotations.

O	E	$8C_3$	$3C_2$	$6C_2$	$6C_4$	decomposition
$\mathscr{A}_1$	1	1	1	1	1	
$\mathscr{A}_2$	1	1	1	-1	-1	
$\mathscr{E}$	2	-1	2	0	0	
$\mathscr{T}_1$	3	0	-1	-1	1	
$\mathscr{T}_2$	3	0	-1	1	-1	
$\mathscr{D}^{(0)}$	1	1	1	1	1	$\mathscr{A}_1$
$\mathscr{D}^{(1)}$	3	0	-1	-1	1	$\mathscr{T}_1$
$\mathscr{D}^{(2)}$	5	-1	1	1	-1	$\mathscr{E} \oplus \mathscr{T}_2$
$\mathscr{D}^{(3)}$	7	1	-1	-1	-1	$\mathscr{A}_2 \oplus \mathscr{T}_1 \oplus \mathscr{T}_2$

We see that under the octahedral symmetry neither $J = 0$ nor $J = 1$ levels splits. Therefore the Yb trapping sites in solid Ne must have a symmetry lower than octahedral to account for the splitting of $J = 0 \to 1$ transitions. For example, if the octahedron cage of Ne atoms housing the Yb atom is elongated along one of the three-fold axes, the symmetry is further reduced to the dihedral group D_3. Then we need to further decompose the irreducible representations of O by the irreducible representations of D_3. This can be done again using Equation (3.12) once we have the character table of D_3. We skip the calculation here and only show the final result: $\mathscr{D}^{(0)} \xrightarrow{O} \mathscr{A}_1 \xrightarrow{D_3} \mathscr{A}_1$ and $\mathscr{D}^{(1)} \xrightarrow{O} \mathscr{T}_1 \xrightarrow{D_3} \mathscr{E} \oplus \mathscr{A}_2$. This means $J = 0$ still does not split but $J = 1$ splits into two sublevels under the D_3 symmetry, which explains the roughly two-fold splitting of bands (a) and (b) in Figure 3.3.

3.4.2 Splitting of $4f \to 5d$ Transitions

The above treatment for $J = 0 \to 1$ transitions does not explain the splitting of bands (c), (d), and (e) because $J = 0$ never splits and $J = 1$ *at most* has a three-fold splitting. To understand these three bands, note that the configuration change $4f^{14}6s^2 \to 4f^{13}5d6s^2$ they all correspond to is, in essence, a $4f \to 5d$ electron jump. Therefore it is heuristic to study the much simpler configuration change $4f6s^2 \to 5d6s^2$ with the same jump, which is found in La although the order of the two states is reversed. The ground state of $4f6s^2 \to 5d6s^2$ is a fine structure doublet $^2F_{7/2}$ and $^2F_{5/2}$, and the excited state is also a fine structure doublet $^2D_{5/2}$ and $^2D_{3/2}$ (Figure 3.9). According the selection rule for J, only three $E1$ transitions are allowed. Therefore we have established a one-to-one correspondence, Yb: $4f^{14}6s^2\ ^1S_0 \to 4f^{13}5d6s^2\ (j_1, j_2)_1 \iff$ "La": $4f6s^2\ ^2F_{j_1} \to 5d6s^2\ ^2D_{j_2}$. Now the angular momenta the crystal field acts on are j_1 and j_2, which are allowed to have more than three-fold splittings given some symmetry.

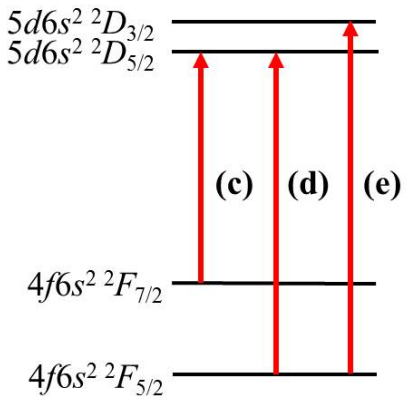

Figure 3.9: The energy levels of the configuration change $4f6s^2\ ^2F \to 5d6s^2\ ^2D$. The only three allowed electric-dipole transitions have a one-to-one correspondence with the three $J = 0 \to 1$ transitions in the Yb configuration change $4f^{14}6s^2 \to 4f^{13}5d6s^2$.

Because j_1 and j_2 are half integers $\frac{3}{2}$, $\frac{5}{2}$, and $\frac{7}{2}$, the 2π rotation (Ω) is no longer an identity operation. Therefore the size of the original rotation group needs to be doubled to accommodate new group elements which are just all the original group elements multiplied by Ω. Such an augmented group is called the crystal double group which inevitably has more

conjugate classes and thus more irreducible representations [46]. The decomposition of $\mathscr{D}^{(j)}$ with half integer j contains only those newly added irreducible representations.

We use the D_3 group as an example since we already know that the octahedral symmetry is too good to describe the splitting of bands (a) and (b). The character table of the crystal double group of D_3 is given in Table 3.3, where $\mathscr{R}_1$, $\mathscr{R}_2$, and $\mathscr{R}_3$ are the original irreducible representation of D_3, and $\mathscr{R}_4$, $\mathscr{R}_5$, and $\mathscr{R}_6$ are the three additional irreducible representations due to the increased number of conjugate classes. Again using Equation (3.12), we can readily decompose $\mathscr{D}^{(j)}$ with half integer j. The result is that $5d6s^2\ {}^2D_{3/2}$ splits into three sublevels, $5d6s^2\ {}^2D_{5/2}$ and $4f6s^2\ {}^2F_{5/2}$ into four, and $4f6s^2\ {}^2F_{5/2}$ into five. Although it takes some more work to figure out the exact assignment, at least we now have enough degrees of freedom to explain the splitting of bands (c), (d), and (e).

Table 3.3: The character table of the crystal double group of the dihedral group D_3.

D_3	E	$2C_3$	$3C_2$	Ω	$2\Omega C_3$	$3\Omega C_2$	decomposition
$\mathscr{R}_1$ ($\mathscr{A}_1$)	1	1	1	1	1	1	
$\mathscr{R}_2$ ($\mathscr{A}_2$)	1	1	-1	1	1	-1	
$\mathscr{R}_3$ ($\mathscr{E}$)	2	-1	0	2	-1	0	
$\mathscr{R}_4$	1	-1	1	-1	1	-1	
$\mathscr{R}_5$	1	-1	-1	-1	1	1	
$\mathscr{R}_6$	2	1	0	-2	-1	0	
$\mathscr{D}^{(1/2)}$	2	1	0	-2	-1	0	$\mathscr{R}_6$
$\mathscr{D}^{(3/2)}$	4	-1	0	-4	1	0	$\mathscr{R}_4 \oplus \mathscr{R}_5 \oplus \mathscr{R}_6$
$\mathscr{D}^{(5/2)}$	6	0	0	-6	0	0	$\mathscr{R}_4 \oplus \mathscr{R}_5 \oplus 2\mathscr{R}_6$
$\mathscr{D}^{(7/2)}$	8	1	0	-8	-1	0	$\mathscr{R}_4 \oplus \mathscr{R}_5 \oplus 3\mathscr{R}_6$

3.5 Emission Spectroscopy

We have seen in Section 3.3 that the 388 nm laser, resonant with the $6s^2\ {}^1S_0 - 6s6p\ {}^1P_1$ transition of Yb atoms in solid Ne, is capable of populating $6s6p\ {}^3P_{0,1,2}$ due to an enhanced intersystem crossing $6s6p\ {}^3P_{0,1,2} \leftarrow 6s6p\ {}^1P_1$. As a result, the 388 nm laser induces a strong green fluorescence corresponding to the spontaneous decays of $6s6p\ {}^3P_{0,1,2}$.

When we use a spectrometer to analyze the steady-state fluorescence from the sample, we

observe a lot more emission bands in the visible-ultraviolet range (Figure 3.10). The reason is that when the 388 nm laser is steadily on, Yb atoms are mostly on the metastable $6s6p\ ^3P_0$, from which they can absorb a second photon and get further excited before decaying back to $6s^2\ ^1S_0$. The strongest absorption band from $6s6p\ ^3P_0$ is centered at 26,740 cm^{-1} (band (f) in Figure 3.5). Due to the broad absorption linewidth, the 388 nm (25,770 cm^{-1}) laser still has a small cross-section for exciting this transition. Once Yb atoms are further excited, more decay channels are turned on, which results in more emission bands. The identification of the emission bands in Figure 3.10 is summarized in Table 3.4, which is discussed below in three wavelength regions.

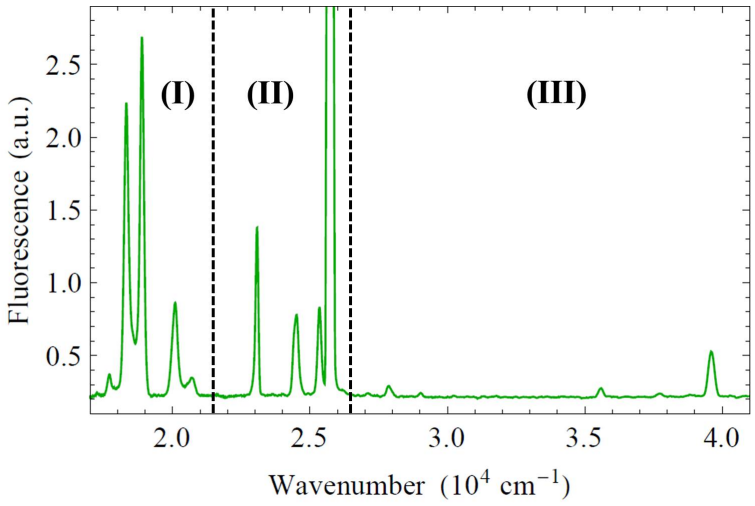

Figure 3.10: The steady-state emission spectrum of Yb atoms in solid Ne induced by the 388 nm laser taken by the Ocean Optics spectrometer with 1.5 nm resolution.

Region I ($1.7\times10^4 \sim 2.1\times10^4$ cm^{-1}): The emission bands in this region are responsible for the strong green glow shown in Figure 3.7. The $6s^2\ ^1S_0 \leftarrow 6s6p\ ^3P_{0,1,2}$ decays fall in this region, and their spacings roughly match those in vacuum. In solid Ne, metastable $6s6p\ ^3P_0$ remains very long-lived and the lifetime of $6s6p\ ^3P_1$ is comparable to that in vacuum, which is the main result of Chapter 4. *Curiously, the lifetime of metastable* $6s6p\ ^3P_2$ *is quenched to only a few milliseconds, for which we do not have a good explanation.* The strong band at 18,900 cm^{-1} corresponds to the $6s6p\ ^1P_1 \leftarrow 6p^2\ ^3P_1$ decay, which follows the $6s6p\ ^3P_0 \rightarrow 6p^2\ ^3P_1$ excitation. The band at 20,710 cm^{-1} is unidentified.

Table 3.4: The identification of the observed emission bands of Yb atoms in solid Ne shown in Figure 3.10. Five emission bands labeled by letters are the corresponding emission of the five absorption bands in Figure 3.2 and Table 3.1. Forbidden transitions in vacuum are labeled by †. ν is the transition frequency in vacuum and $\nu_{\rm e}^*$ is the center of emission bands in solid Ne. $\nu_{\rm a}^*$, the center of absorption bands in solid Ne, is also listed for comparison. All numbers are in $\rm cm^{-1}$. $\nu_{\rm e}^*$ and $\nu_{\rm a}^*$ have an uncertainty of 40 $\rm cm^{-1}$.

Transition		ν	$\nu_{\rm e}^*$	$\nu_{\rm e}^* - \nu$	$\nu_{\rm a}^*$	$\nu_{\rm a}^* - \nu_{\rm e}^*$
$6s^2\ {}^1S_0 \leftarrow 6s6p\ {}^3P_0$	†	17,288	17,730	+442		
$6s^2\ {}^1S_0 \leftarrow 6s6p\ {}^3P_1$	(a)	17,992	18,320	+328	18,510	+190
$6s6p\ {}^1P_1 \leftarrow 6p^2\ {}^3P_1$		18,737	18,900	+163		
$6s^2\ {}^1S_0 \leftarrow 6s6p\ {}^3P_2$	†	19,710	20,080	+370		
Unidentified			20,710			
$6s^2\ {}^1S_0 \leftarrow 4f^{13}5d^16s^2\ (\frac{7}{2},\frac{3}{2})_2$	†	23,189	23,070	−119		
$6s^2\ {}^1S_0 \leftarrow 5d6s\ {}^3D_1$	†	24,489	24,490	~ 0		
$6s^2\ {}^1S_0 \leftarrow 6s6p\ {}^1P_1$	(b)	25,068	25,320	+252	25,760	+440
$6s^2\ {}^1S_0 \leftarrow 5d6s\ {}^1D_2$	†	27,678	27,860	+182		
$6s^2\ {}^1S_0 \leftarrow 4f^{13}5d^16s^2\ (\frac{7}{2},\frac{5}{2})_1$	(c)	28,857	29,030	+173	29,140	+110
$6s^2\ {}^1S_0 \leftarrow 4f^{13}6s^26p\ (\frac{7}{2},\frac{3}{2})_2$	†	35,197	35,590	+393		
$6s^2\ {}^1S_0 \leftarrow 4f^{13}5d^16s^2\ (\frac{5}{2},\frac{5}{2})_1$	(d)	37,415	37,730	+315	37,730	~ 0
$6s^2\ {}^1S_0 \leftarrow 4f^{13}5d^16s^2\ (\frac{5}{2},\frac{3}{2})_1$	(e)	38,422	39,610	+1,188	39,670	+60

Region II ($2.2 \times 10^4 \sim 2.6 \times 10^4$ $\rm cm^{-1}$): Apart from the $6s^2\ {}^1S_0 \leftarrow 6s6p\ {}^1P_1$ decay at 25,320 $\rm cm^{-1}$, the other two bands in this region are identified as two forbidden transitions of Yb in vacuum. The band at 23,070 $\rm cm^{-1}$ corresponds to the $6s^2\ {}^1S_0 \leftarrow 4f^{13}5d6s^2\ (\frac{7}{2},\frac{3}{2})_2$ decay, which is forbidden by the selection rule $J = 0 \nleftrightarrow 2$. Note that the level $4f^{13}5d6s^2\ (\frac{7}{2},\frac{3}{2})_2$ has the same configuration as the excited levels of absorption bands (c), (d), and (e). The band at 24,490 $\rm cm^{-1}$ corresponds to the $6s^2\ {}^1S_0 \leftarrow 6s5d\ {}^3D_1$ decay, which is forbidden by the parity selection rule.

Region III ($2.7 \times 10^4 \sim 4.0 \times 10^4$ $\rm cm^{-1}$): The energy of the emission bands in this region is higher than that of the 388 nm photon because Yb atoms on $6s6p\ {}^3P_0$ absorb a second 388 nm photon and get further excited before decaying to $6s^2\ {}^1S_0$. The emission bands are tentatively assigned to the decays of various excited levels to $6s^2\ {}^1S_0$ according to the proximity of their transition wavenumbers to those in vacuum.

CHAPTER 4

LIFETIMES OF YB IN SOLID NE

4.1 Hyperfine Quenching

The conservation of angular momentum strictly forbids single-photon transitions between two atomic states if both electronic angular momenta are equal to zero, i.e. $J = 0 \nleftrightarrow 0$. This restriction can be circumvented by state mixing due to the hyperfine interaction [47]. The consequent increase in the transition rate is referred to as hyperfine quenching (HFQ), a feeble mechanism that typically plays a significant role in the radiative decay of only the lowest lying $^3P_{0,2}$ levels of divalent atoms.

The earliest studies of the HFQ effect focused on the spectra originating from nebulae [48]. More recently, the isotopic dependence of these astronomical spectra have been used to infer HFQ rates [49] and, conversely, isotope ratios that result from stellar nucleosynthesis [50]. In the laboratory, the $1s2p\ ^3P_{0,2}$ levels in He-like ions were the first to be measured and are the most thoroughly studied [51]. The HFQ rates of a handful of many-electron ions have also been measured [51, 52, 53, 54]. However, the rate has never been measured in any neutral atoms due to difficulties involved in populating the relevant levels and subsequently observing their slow decay.

In neutral atoms, efforts have been made in modern *ab initio* calculations of the HFQ rate [55, 56], motivated by the promising application of neutral divalent atoms to optical clocks [57], quantum computing [58], and quantum simulation of many-body systems [59]. In the case of optical clocks, the HFQ rate determines the natural linewidth and the Rabi frequency of the "clock transition" $ns^2\ ^1S_0 - nsnp\ ^3P_0$ in fermionic isotopes. The HFQ rate calculations require accurate knowledge of the atomic structure of the many-electron atoms.

For $6s^2\ {}^1S_0\ (F = 1/2) - 6s6p\ {}^3P_0\ (F = 1/2)$ in ^{171}Yb with a nuclear spin $I = 1/2$, the HFQ rate (Γ_{HFQ}) involves the matrix element of the electric-dipole ($E1$) operator ($\mathscr{D}$) between intermediate levels (λ) and the ground level $6s^2\ {}^1S_0$, as well as the matrix element of the hyperfine interaction ($\mathscr{H}_{\mathrm{HFI}}$) between these levels ($\lambda$) and $6s6p\ {}^3P_0$,

$$\Gamma_{\mathrm{HFQ}}({}^1S_0 - {}^3P_0) \propto \left| \sum_{\lambda} \frac{\langle {}^1S_0 || \mathscr{D} || \lambda \rangle \langle \lambda || \mathscr{H}_{\mathrm{HFI}} || {}^3P_0 \rangle}{E(\lambda) - E({}^3P_0)} \right|^2, \tag{4.1}$$

where $E(\lambda)$ are energies of the levels relative to the ground level [55]. Among the intermediate levels, the HFQ of $6s6p\ {}^3P_0$ is predominantly caused by the admixture of the lowest lying $6s6p\ {}^3P_1$ and $6s6p\ {}^1P_1$ [55], from which the transitions to the ground level are both $E1$ allowed. Our measurement, therefore, serves as a sensitive benchmark for these calculations.

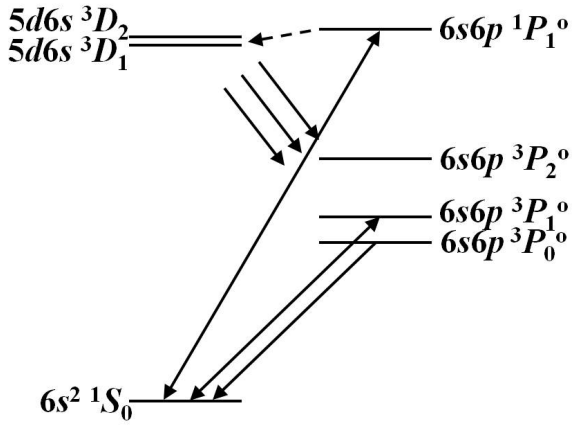

Figure 4.1: Low-lying atomic levels and transitions of Yb in solid Ne. ${}^3P_0$ can be efficiently populated by virtue of an enhanced intersystem crossing ${}^3D_1 \leftarrow {}^1P_1$. The radiative decay of ${}^3P_0$ is observed in both ^{171}Yb and ^{172}Yb samples.

We employ a novel technique of probing atoms embedded in solid Ne to extract the HFQ rate $\Gamma_{\mathrm{HFQ}}({}^1S_0 - {}^3P_0)$ in free ^{171}Yb. Interrogating atoms trapped in a solid offers both high atomic density and long observation time. In addition, while matrix isolated Yb atoms qualitatively resemble free atoms, they exhibit an enhanced intersystem crossing $5d6s\ {}^3D_1 \leftarrow 6s6p\ {}^1P_1$, enabling efficient population of $6s6p\ {}^3P_0$ by pumping the strong $6s^2\ {}^1S_0 - 6s6p\ {}^1P_1$ transition and the subsequent spontaneous decay (Figure 4.1) [24]. We

choose solid Ne as the matrix because it is less polarizable than heavier noble-gas solids and more technically accessible than solid He. While He only solidifies under at least 25 bar pressure, Ne readily forms a solid with face-centered-cubic structure at 24.5 K and 1 bar [22].

The main challenge of performing this measurement is to properly account for various medium effects. First, the medium may open additional radiative or nonradiative decay channels on an excited atom. Second, the medium may alter the HFQ rate of a free atom by modifying the atomic wave functions and shifting the energies in Equation (4.1). Third, Fermi's golden rule dictates that the spontaneous emission rate of a transition depends cubically on the transition frequency that may be shifted in medium. Finally, the spontaneous emission rate also depends on the environment of the emitter. Such a phenomenon, known as the Purcell effect, is one of the hallmarks of quantum electrodynamics (QED). In cavity QED, the decay rate is modified by the geometry of the surrounding vacuum environment [60, 61, 62, 63]. Within a medium, however, the decay rate depends on the index of refraction because it modifies both the photon dispersion relation and the energy fluctuation of the QED vacuum. Although the index-of-refraction effect has been known for some time, there is still considerable tension in its understanding [64, 65].

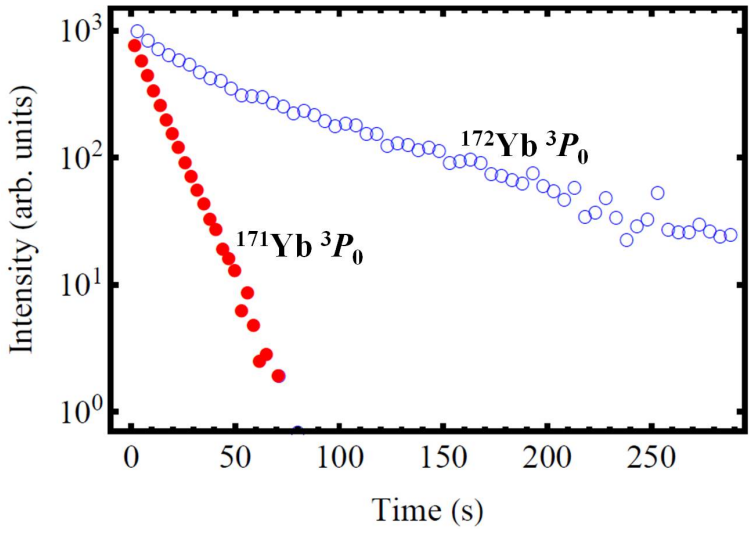

Figure 4.2: The time-dependent fluorescence intensity of ^{171}Yb $^3P_0$ (red solid circles) and ^{172}Yb $^3P_0$ (blue open circles) in solid Ne near the center of the emission peak. The influence of the HFQ effect is evident.

We address these effects as follows. First, we measure the $6s6p\ ^3P_0$ decay rate for isotopically pure ^{171}Yb and ^{172}Yb ($I = 0$) in solid Ne (Figure 4.2). The difference between these two rates separates the HFQ contribution from any medium quenching mechanisms that are independent of isotopes. Second, the Yb transition frequencies in solid Ne are used to calculate the energy and frequency dependent corrections. Third, we measure the decay rate of Yb $6s6p\ ^3P_1$ in solid Ne and compare it with the experimental value in vacuum [66] to provide a direct calibration of the index-of-refraction effect. After making these corrections, we then obtain the HFQ rate of a free atom.

4.2 Lifetime of $6s6p\ ^3P_0$ in Solid Ne

The samples are prepared with a similar setup we used previously [24]. Before the deposition on the liquid-He cooled sapphire substrate, Ne gas (99.999%) flows through a noble gas purifier (LDetek LDP1000) and a 77 K charcoal trap in order to minimize the growth defects and increase the sample transparency. We codeposit Yb using an atomic beam generated by an effusive oven. To avoid the formation of Yb clusters, we keep the Yb-to-Ne ratio below 5 ppm and the temperature below 5 K to suppress the mobility of the atoms. Samples with isotopically pure ^{171}Yb (95%, Oak Ridge batch 196043) and ^{172}Yb (97%, Oak Ridge batch 124501) are separately made. While the enriched Yb is available for several even isotopes, ^{172}Yb contains the least concentration of odd isotopes.

We use a 385 nm light-emitting diode (LED) to excite the $^1S_0 - {}^1P_1$ transition [44] and subsequently populate $^3P_0$. The fluorescence is detected by a 1.5 nm resolution optical spectrometer (Ocean Optics USB4000-UV-VIS). Figure 4.3(a) shows the emission spectrum of ^{171}Yb $^3P_0$ (solid circles) and ^{172}Yb $^3P_0$ (open circles) in solid Ne after the LED is switched off. We record the fluorescence decay at select wavelengths for 100 s for ^{171}Yb and 300 s for ^{172}Yb. The decay near the center of the emission peak (565 nm) is shown in Figure 4.2. At each wavelength, the decay rate of each isotope is obtained by fitting the data to an exponential function and is plotted in Figure 4.3(b). The uncertainty about the size of the

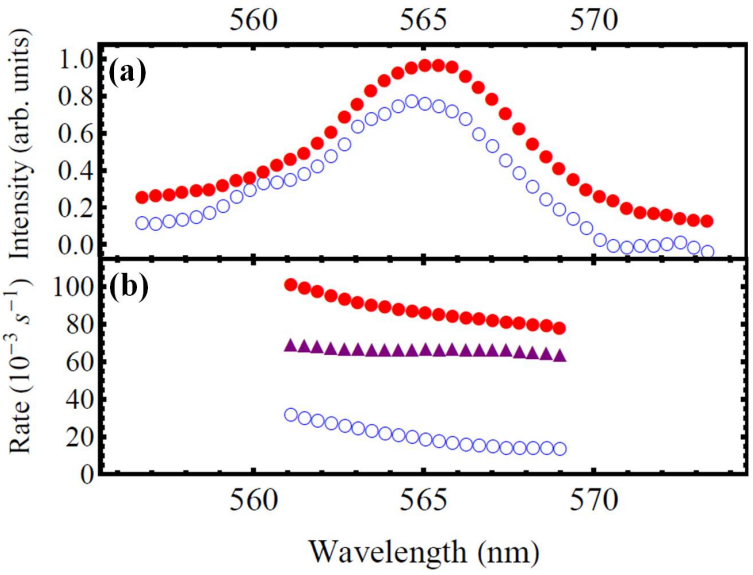

Figure 4.3: (a) The $^1S_0 \leftarrow {}^3P_0$ emission spectrum of ^{171}Yb (red solid circles) and ^{172}Yb (blue open circles) in solid Ne after the 385 nm LED is switched off. The peak is shifted from the vacuum position at 578.4 nm. The spectra are separately normalized so that the peaks appear to have similar height. (b) The decay rate of ^{171}Yb $^3P_0$ (red solid circles) and ^{172}Yb $^3P_0$ (blue open circles), and the difference of the decay rates between the two isotopes (purple solid triangles) at select wavelengths. The error bars are about the size of the markers.

markers is determined from the fitting error and the sample variance based on three ^{171}Yb and two ^{172}Yb samples with different Yb densities and optical transparencies. The strong wavelength dependence of the decay rates is in part due to the frequency cube dependence. The remainder is likely caused by the interaction with phonons of different energies. The sum of multiple exponential functions, which describes multiple types of trapping sites in solid Ne, gives a better fit at some wavelengths, but the weighted average of the multiple rates is not significantly different from the rate of the single exponential fit.

The decay rate of ^{172}Yb $^3P_0$ near 565 nm is approximately 2×10^{-2} s^{-1}. Since its single-photon decay in vacuum is strictly forbidden, this rate reflects the overall medium quenching of an excited atom. One possible quenching mechanism may be that the atomic wave functions are perturbed by the crystal field in solid Ne. To model this perturbation (Appendix C), we assume that this field is randomly oriented and has a constant strength. Eleven low-lying levels are included, between which the reduced matrix elements of the

electric-dipole operator have been calculated [67]. We sum over M_J states and the orientation of the field, leading to a Stark-like coupling between levels. In order to account for the observed decay rate, it requires a 27 MV/m crystal field so that the perturbed $^3P_0$ wave function has an admixture of $^3P_1$ with a mixing coefficient of 8.2×10^{-5}. Such a crystal field strength is not unexpected in solid Ne [22].

For the ^{171}Yb $^3P_0$ decay, since the nuclear spins are unpolarized and the crystal field is randomly oriented, the effects of the HFQ and the medium quenching add incoherently. We plot the difference of the decay rates between the two isotopes in Figure 4.3(b) (solid triangles). As expected, this differential rate is mostly independent of the wavelength and represents the HFQ contribution. We take the average of the rates weighted by the emission intensity and find the HFQ rate of ^{171}Yb $^3P_0$ in solid Ne to be $(6.72 \pm 0.28) \times 10^{-2}$ s^{-1}. The uncertainty is conservatively chosen to be half of the full range.

4.3 Medium Effects

We first examine the medium's influence on the HFQ mechanism described in Equation (4.1). From the crystal field strength estimation, we are assured that the atomic wave functions are essentially intact. However, the medium alters the energy differences in the denominators. The HFQ of $^3P_0$ is predominantly caused by the admixture of the lowest lying $^3P_1$ and $^1P_1$ [55]. In solid Ne, we take $E(^3P_0) = (565 \text{ nm})^{-1}$, $E(^3P_1) = (546 \text{ nm})^{-1}$, and $E(^1P_1) = (396 \text{ nm})^{-1}$ in the emission mode [24, 44]. $E(^3P_1) - E(^3P_0)$ in solid Ne is equal to 616 cm^{-1} and is changed from its vacuum value (704 cm^{-1}) by a factor of 0.875. Therefore, the HFQ rate is enhanced by a factor of 1.306 if the $^3P_1$ term dominates the sum. Similarly, $E(^1P_1) - E(^3P_0)$ is changed by 0.971, and the rate enhanced by 1.061. Assuming a uniform probability distribution of the relative contribution from $^3P_1$ and $^1P_1$, we take the midpoint as the mean and $1/\sqrt{12}$ of the full range as the uncertainty [68] and obtain an enhancement factor of 1.183 ± 0.071.

We then consider the medium's influence on the spontaneous emission rate of a transition,

$$\frac{\Gamma_{\rm m}}{\Gamma_{\rm v}} = \left(\frac{\omega_{\rm m}}{\omega_{\rm v}}\right)^3 G(n), \tag{4.2}$$

where $\omega_{\rm m}$ ($\omega_{\rm v}$) is the transition frequency in medium (vacuum), and the scale factor G is a function of the index of refraction n. To extract $\Gamma_{\rm HFQ,v}(^1S_0 - {}^3P_0)$, we use $\omega_{\rm Ne}(^1S_0 - {}^3P_0) = (565 \pm 1 \text{ nm})^{-1}$ and $\omega_{\rm v}(^1S_0 - {}^3P_0) = (578.4 \text{ nm})^{-1}$ to calculate the frequency dependent correction. The uncertainty is due to the spectrometer calibration and the sample variance.

We determine $G_{\rm Ne}$ by measuring the $^3P_1$ decay for the following reasons. The HFQ transition $^1S_0$ ($F = 1/2$) $-$ $^3P_0$ ($F = 1/2$) and the intercombination transition $^1S_0 - {}^3P_1$ are both of $E1$ type. Their transition wavelengths are sufficiently close that the wavelength dependence of the index of refraction is insignificant. The $^3P_1$ decay rate in vacuum is precisely known $\Gamma_{\rm v}(^1S_0 - {}^3P_1) = (1.162 \pm 0.008) \times 10^6 \text{ s}^{-1}$ [66]. Compared to this rate, the medium quenching rate ($\sim 2 \times 10^{-2} \text{ s}^{-1}$) is negligible, which allows us to use the measured total decay rate for $\Gamma_{\rm Ne}(^1S_0 - {}^3P_1)$.

4.4 Lifetime of $6s6p\ ^3P_1$ in Solid Ne

For the $^3P_1$ lifetime measurement in solid Ne, samples of natural Yb are used. We excite the $^1S_0 - {}^3P_1$ transition by a green diode pumped solid state laser (Opto Engine MGL-III-543). The fluorescence light is coupled into a spectrometer (McPherson 225) and detected by a photomultiplier tube counting module (Sens-Tech P10PC-2) mounted at the exit of the spectrometer. A dead time correction is applied for the counting rate (Appendix E). Figure 4.4(a) shows the steady-state emission spectrum of $^3P_1$ in solid Ne with 1 nm resolution.

We chop the laser at 50 kHz with a 50% duty cycle using an acousto-optic modulator and record the decay at select wavelengths with 50 ns resolution. The decay rate at each wavelength is plotted in Figure 4.4(b). The average of the rates weighted by the emission intensity is $\Gamma_{\rm Ne}(^1S_0 - {}^3P_1) = (1.464 \pm 0.040) \times 10^6 \text{ s}^{-1}$, where the uncertainty is half of the

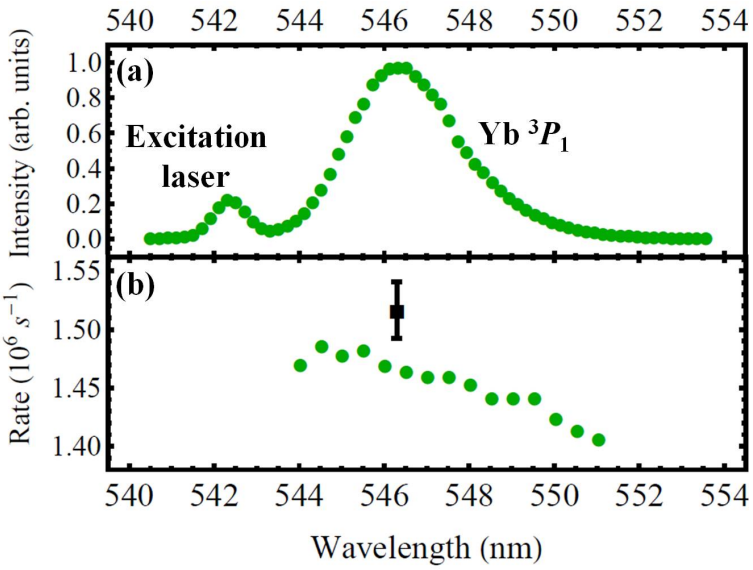

Figure 4.4: (a) The $^1S_0 \leftarrow {}^3P_1$ emission spectrum of Yb in solid Ne induced by the 543 nm laser. The peak is shifted from the vacuum position at 555.8 nm. (b) The decay rate of $^3P_1$ at select wavelengths in solid Ne (green circles). The error bars are about the size of the markers. The decay rate in vacuum, 1.162×10^6 s^{-1}, is off the scale. The black square with an error bar indicates the predicted $^3P_1$ decay rate in solid Ne using the RC model and the frequency cube dependence.

full range. From Equation (4.2) for the $^3P_1$ decay with $\omega_{\rm Ne}(^1S_0 - {}^3P_1) = (546 \pm 1 \text{ nm})^{-1}$ and $\omega_{\rm v}(^1S_0 - {}^3P_1) = (555.8 \text{ nm})^{-1}$, we obtain the transition-independent $G_{\rm Ne} = 1.194 \pm 0.036$. Again using Equation (4.2) for the $^3P_0$ decay, we arrive at $\Gamma_{\rm HFQ,v}(^1S_0 - {}^3P_0) = (4.42 \pm 0.35) \times 10^{-2}$ s^{-1} for free ^{171}Yb. All the corrections we have made are summarized in Table 4.1.

We compare this result to two available calculations: 6.2×10^{-2} s^{-1} (no uncertainty provided) [69] and 4.35×10^{-2} s^{-1} (a few percent uncertainty) [55]. Authors of Reference [69] have used experimentally measured hyperfine parameters in their calculation and have included only two intermediate levels in Equation (4.1). Authors of Reference [55] have computed the sum with multiple intermediate levels and have independently calculated the hyperfine constants with better than 1% accuracy as a verification of the quality of their technique. Our measurement is in good agreement with Reference [55].

We are also able to compare our experimentally determined $G_{\rm Ne}$ to theoretical predictions. One theory supported by recent experiments for $E1$ transitions [70, 71] is the real

Table 4.1: A summary of corrections due to medium effects for the extraction of the $^3P_0$ HFQ rate of free ^{171}Yb based on the measurements in solid Ne.

Correction	Scale factor	Uncertainty
Energy difference, Equation (4.1)	0.845	6.0%
Medium quenching	0.771	4.2%
Index-of-refraction effect, Equation (4.2)	0.838	3.0%
Frequency cube, Equation (4.2)	0.932	0.5%
Total	0.508	7.9%

cavity (RC) model [72]. It treats the emitter as residing in an empty spherical cavity carved out of a lossless, homogeneous, and isotropic medium with permittivity $\epsilon = n^2\epsilon_0$. The macroscopic field in the dielectric is canonically quantized. The model predicts the following scaling with n,

$$G^{\mathrm{RC}}(n) = n^3 \left[\frac{1}{n}\left(\frac{E_{\mathrm{loc}}}{E_{\mathrm{mac}}}\right)_{\mathrm{RC}}\right]^2. \tag{4.3}$$

The factor n^3 comes from the in-medium photon dispersion relation. The macroscopic field operator $\hat{\boldsymbol{E}}_{\mathrm{mac}}$ is renormalized by $1/n$ due to the in-medium energy density $\epsilon\hat{\boldsymbol{E}}^2_{\mathrm{mac}}/2$. The ratio of the local field inside the cavity E_{loc} to the macroscopic field far outside the cavity E_{mac} is $(E_{\mathrm{loc}}/E_{\mathrm{mac}})_{\mathrm{RC}} = 3\epsilon/(2\epsilon + \epsilon_0)$ using the boundary conditions on the sphere.

Given the growth conditions of our solid Ne samples and both the wavelength and the temperature dependence of the index of refraction, we take $n_{\mathrm{Ne}} = 1.10 \pm 0.01$ [73, 74, 75]. Therefore, the RC model gives $G^{\mathrm{RC}}_{\mathrm{Ne}} = 1.239 \pm 0.024$. This is in good agreement with our experimentally determined value $G_{\mathrm{Ne}} = 1.194 \pm 0.036$. The predicted $^3P_1$ rate in solid Ne using the RC model and the frequency cube dependence is also indicated in Figure 4.4(b) (solid square).

In heavier noble gas solids, we find that the Yb transitions suffer from exacerbated medium effects. In solid Ar, they manifest in a stronger wavelength dependence of the $^3P_1$ decay rate. Our measurements show $\omega_{\mathrm{Ar}}(^1S_0 - {}^3P_1) = (562 \pm 1\ \mathrm{nm})^{-1}$, $\Gamma_{\mathrm{Ar}}(^1S_0 - {}^3P_1) = (1.82 \pm 0.19) \times 10^6\ \mathrm{s}^{-1}$, and thus $G_{\mathrm{Ar}} = 1.62 \pm 0.17$. The larger uncertainty makes solid Ar a less attractive medium for transition-rate measurements. Nevertheless, this result still

agrees with the RC model prediction $G_{\mathrm{Ar}}^{\mathrm{RC}} = 1.69 \pm 0.05$ with $n_{\mathrm{Ar}} = 1.28 \pm 0.02$ [76, 75]. In solid Xe, the Yb $^3P_0$ lifetime is shorter than 50 μs due to a much stronger crystal field. Therefore, the HFQ measurement becomes impossible.

4.5 Summary

In conclusion, we have measured the HFQ rate of the $^1S_0(F = 1/2) - ^3P_0(F = 1/2)$ transition in ^{171}Yb based on the matrix isolation technique using solid Ne and spectrally resolved fluorescence decay measurements. We have accounted for medium effects using measurements of both the ^{172}Yb $^3P_0$ decay and the Yb $^3P_1$ decay in solid Ne. The average $^3P_1$ decay rate across the emission peak in solid Ne agrees with the RC model prediction. In order to carry out a more precise study on the index-of-refraction effect, one needs to consider the phonon interaction to better understand the wavelength dependence.

Finally, the most suitable naturally abundant candidates for the study of the HFQ effect using this technique are ^{25}Mg, ^{43}Ca, ^{67}Zn, ^{87}Sr, ^{111}Cd, ^{113}Cd, ^{171}Yb, ^{173}Yb, ^{199}Hg, and ^{201}Hg. For each of these candidates, a naturally abundant isotope with zero nuclear spin is available, and the transition from the ground level to the lowest lying $^1P_1$ is optically accessible. Lighter atoms are more tightly bound which likely means that the medium induced corrections are smaller but the efficiency of populating $^3P_0$ is worse. On the other hand, lighter atoms also have higher $^1P_1$ levels which may provide an alternative and more efficient path for the $^3P_0$ population.

CHAPTER 5

OPTICAL PUMPING OF YB NUCLEI IN SOLID NE

Yb has two stable isotopes with nonzero nuclear spins, ^{171}Yb and ^{173}Yb. Ne, on the other hand, only has one stable isotope with a nonzero nuclear spin, ^{21}Ne, with a natural abundance of 0.27% (Table 5.1). We have made a few attempts to polarize the ^{171}Yb nuclei in a natural-Ne solid by transverse optical pumping. However, we have not observed the polarization signal yet for at least two reasons. First, the optical pumping rate in solid Ne is significantly reduced due to both the broad linewidth of electronic transitions and the presence of the crystal field. Second, the dark-state detection of the spin polarization is not feasible due to the unresolved hyperfine structure while the direct detection of the sample magnetization is challenging because Yb nuclei are very dilute compared to conventional condensed matter samples for nuclear magnetic resonance. Nevertheless, the current understanding is reported in this chapter to provide a guidance for future efforts.

Table 5.1: Properties of stable Yb and Ne Isotopes with nonzero nuclear spins [77]. M is the atomic mass, N.A. stands for natural abundance, I is the nuclear spin, g_I is the nuclear g-factor, $\mu = g_I I \mu_{\mathrm{N}}$ is the nuclear magnetic moment where μ_{N} is the nuclear magneton, and $\gamma = g_I \mu_{\mathrm{N}}/\hbar$ is the gyromagnetic ratio.

isotope	M (u)	N.A. (%)	I	g_I	μ (μ_{N})	$\gamma/2\pi$ (Hz/G)
^{171}Yb	170.94	14.28	1/2	0.987	+0.494	745
^{173}Yb	172.94	16.13	5/2	-0.259	-0.648	195
^{21}Ne	20.99	0.27	3/2	-0.441	-0.662	333

5.1 Transverse Optical Pumping

In transverse optical pumping [36], a magnetic holding field is applied perpendicular to a laser beam. The laser for optical pumping is circularly polarized and is resonant with a transition of the atoms to be spin polarized. The absorption of photons from this pump beam creates a spin polarization in the ground state which is then forced into Larmor precession by the transverse magnetic field. In our case, the intensity of the optical pumping laser, and

thus the optical pumping rate, is modulated at the Larmor frequency by an acousto-optical modulator to increase the polarization [78], and the precession of the polarization is read out by a SQUID magnetometer (Figure 5.1).

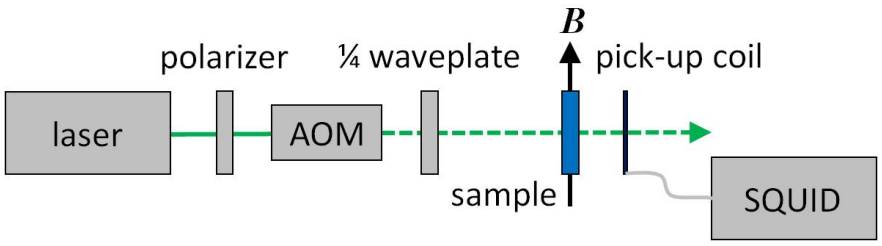

Figure 5.1: A sketch of the experimental setup for transverse optical pumping.

The dynamics of the spin ensemble during transverse optical pumping is described by the phenomenological Bloch equations [79]

$$\frac{\mathrm{d}\boldsymbol{P}}{\mathrm{d}t} = \tilde{\Gamma}_{\mathrm{p}}(t)(\boldsymbol{P}_0 - \boldsymbol{P}) + \boldsymbol{P} \times \boldsymbol{\omega}_{\mathrm{L}} - \mathbb{T}^{-1} \cdot \boldsymbol{P}. \tag{5.1}$$

Here, $\boldsymbol{P} = (P_x, P_y, P_z)$ is the polarization vector of the spin ensemble. $\boldsymbol{P}_0 = (P_0, 0, 0)$ is the polarization vector of the circularly polarized laser beam traveling in the $+x$ direction, where P_0 is the degree of polarization. $\tilde{\Gamma}_{\mathrm{p}}(t)$ is the pumping rate modulated at an angular frequency ω. $\boldsymbol{\omega}_{\mathrm{L}} = (0, 0, \omega_{\mathrm{L}})$ is the Larmor frequency vector given a magnetic holding field $\boldsymbol{B}$ pointing in the $+z$ direction (the longitudinal direction) with $\boldsymbol{\omega}_{\mathrm{L}} = \gamma \boldsymbol{B}$, where γ is the gyromagnetic ratio of the spins. $\mathbb{T}^{-1} = \mathrm{diag}(T_2^{-1}, T_2^{-1}, T_1^{-1})$ is the relaxation matrix, where T_1 (T_2) is the longitudinal (transverse) relaxation time.

Under the rotating-wave approximation, the Bloch equations can be analytically solved (Appendix F). The steady-state polarization is

$$P \equiv |\boldsymbol{P}| = P_0 \cdot \frac{|c_1|}{\sqrt{(\omega - \omega_{\mathrm{L}})^2 + (c_0 + 1/T_2)^2}} \tag{5.2}$$

where c_0 and c_1 are coefficients of the Fourier expansion $\tilde{\Gamma}_{\mathrm{p}}(t) = \sum_n c_n \mathrm{e}^{\mathrm{i}n\omega t}$. In our case, $\tilde{\Gamma}_{\mathrm{p}}(t)$ is a square wave with a duty cycle D and a height Γ_{p}, the Fourier coefficients of which

are $c_0 = D\Gamma_\mathrm{p}$ and $c_1 = \Gamma_\mathrm{p}\sin(D\pi)e^{-iD\pi}/\pi$. The steady-state polarization when the laser modulation frequency is resonant with the Larmor frequency ($\omega = \omega_\mathrm{L}$) is then

$$P_\mathrm{r} = P_0 \cdot \frac{\sin(D\pi)/\pi}{D + 1/\Gamma_\mathrm{p}T_2}. \tag{5.3}$$

The optimal D_m that maximizes P_r satisfies $D_\mathrm{m} + (\Gamma_\mathrm{p}T_2)^{-1} = \pi^{-1}\tan(D_\mathrm{m}\pi)$ and the maximal polarization is $P_\mathrm{m} = P_0\cos(D_\mathrm{m}\pi)$. When $\Gamma_\mathrm{p}T_2 \ll 1$, $D_\mathrm{m} \sim \frac{1}{2} - \Gamma_\mathrm{p}T_2/\pi^2$ and $P_\mathrm{m}/P_0 \sim \Gamma_\mathrm{p}T_2/\pi$. When $\Gamma_\mathrm{p}T_2 \gg 1$, $D_\mathrm{m} \sim (\pi^2\Gamma_\mathrm{p}T_2/3)^{-1/3}$ and $P_\mathrm{m}/P_0 \sim 1 - \frac{1}{2}(\Gamma_\mathrm{p}T_2/3\pi)^{-2/3}$. To achieve a high steady-state on-resonance polarization, we can work to increase the degree of polarization of the photons ($P_0 \uparrow$), increase the pumping rate ($\Gamma_\mathrm{p} \uparrow$), and increase the transverse relaxation time ($T_2 \uparrow$). Among these parameters, the polarization of the photons is usually well controlled with $P_0 \sim 1$.

5.2 Pumping Rate for Nuclear Polarization

In a solid Ne matrix, the pumping rate for nuclear polarization is inevitably reduced from that in vacuum, and the reduction of the pumping rate can be examined in two steps. First, the overall excitation rate in solid Ne is suppressed because the cross-section is suppressed as a result of the broadened linewidth (Section 3.3.5). Second, the pumping rate for nuclear polarization is further suppressed because the crystal field in solid Ne strongly perturbs the hyperfine interaction which plays a crucial role in transferring angular momenta from electrons to the nucleus.

5.2.1 Pumping Rate in Vacuum

We use the $6s^2\ {}^1S_0 - 6s6p\ {}^3P_1$ transition for optical pumping because $6s^2\ {}^1S_0 - 6s6p\ {}^1P_1$ is not closed in solid Ne (Section 3.3.2). However, the $6s6p\ {}^3P_1$ transition is about 200 times weaker than $6s6p\ {}^1P_1$ due to the flip of the electronic spin S. The hyperfine structure of $6s6p\ {}^3P_1$ in ^{171}Yb is described by the Hamiltonian $\mathscr{H}_\mathrm{HFI} = A\boldsymbol{I}\cdot\boldsymbol{J}'$, where $A \sim 4$ GHz is the

hyperfine constant, $\boldsymbol{I}$ ($I = 1/2$) is the nuclear spin operator and $\boldsymbol{J'}$ ($J' = 1$) is the electron's total angular momentum operator. Thus $6s6p\ {}^3P_1$ splits into two hyperfine levels $F' = 1/2$ and 3/2 (Figure 5.2). The hyperfine structure of $6s^2\ {}^1S_0$ is simply a doublet $F = 1/2$.

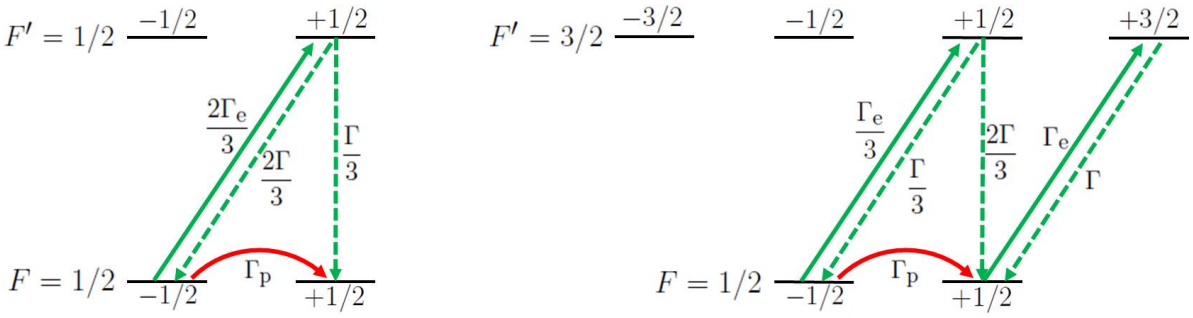

Figure 5.2: The pumping scheme for polarizing ^{171}Yb nuclei in vacuum using the $F = 1/2 \leftrightarrow F' = 1/2$ and 3/2 transitions and the σ_+ light. The spontaneous emission rate of $J = 0 \leftarrow J' = 1$ is Γ. The excitation rate of $J = 0 \rightarrow J' = 1$ is Γ_e. The pumping rate of $|M_F = -1/2\rangle \rightarrow |M_F = +1/2\rangle$ is $\Gamma_p = 2\Gamma_e/9$ when $\Gamma_e \ll \Gamma$.

We assume that the decay rate of $J = 0 \leftarrow J' = 1$ is Γ and the excitation rate of some σ_+ light driving $|M_J = 0\rangle \rightarrow |M'_J = +1\rangle$ is Γ_e with $\Gamma_e \ll \Gamma$. Γ_e is calculated using $\Gamma_e \sim (I_e/I_{sat})(\Gamma/2)$, where I_e is the intensity of the excitation light and I_{sat} is the saturation intensity of the transition. The pumping rate of $|M_F = -1/2\rangle \rightarrow |M_F = +1/2\rangle$ equals Γ_e multiplied by the absorption probability of $|M_F = -1/2\rangle \rightarrow |M'_F = +1/2\rangle$ and the decay probability of $|M_F = +1/2\rangle \leftarrow |M'_F = +1/2\rangle$. The pumping rate in the opposite direction can be similarly calculated. Then the net pumping rate Γ_p equals the difference of these two rates. Let us take the $F = 1/2 \leftrightarrow F' = 1/2$ hyperfine transition as an example. The absorption probability of $|M_F = -1/2\rangle \rightarrow |M'_F = +1/2\rangle$ is 2/3 because $|M_F = -1/2\rangle$ is purely $|M_I = -1/2, M_J = 0\rangle$ but $|M'_F = +1/2\rangle$ only contains $\sqrt{2/3}$ of $|M_I = -1/2, M'_J = +1\rangle$. The decay probability of $|M_F = +1/2\rangle \leftarrow |M'_F = +1/2\rangle$ is 1/3 for the similar reason. Therefore the pumping rate of $|M_F = -1/2\rangle \rightarrow |M_F = +1/2\rangle$ is $2\Gamma_e/9$. The pumping rate in the opposite direction is zero, so the net pumping rate Γ_p is $2\Gamma_e/9$. Similar analysis can be made for the $F = 1/2 \leftrightarrow F' = 3/2$ hyperfine transition which gives an identical pumping rate of $|M_F = -1/2\rangle \rightarrow |M_F = +1/2\rangle$.

5.2.2 Pumping Rate in Solid Ne

In solid Ne, the hyperfine structure of $6s6p\ ^3P_1$ is not resolved, and thus both hyperfine transitions are excited with the same probability. The saturation intensity of the $6s^2\ ^1S_0 - 6s6p\ ^3P_1$ transition in vacuum is $I_{\rm sat} = 0.14$ mW/cm^2. The saturation intensity in solid Ne is, however, increased by the linewidth broadening factor W (Section 3.3.5), which is about 7×10^6 for $6s^2\ ^1S_0 - 6s6p\ ^3P_1$ (Table 3.1). The intensity of our on-resonance excitation laser is $I_{\rm e} \sim 50$ mW/cm^2. Therefore $\Gamma_{\rm e} \sim (I_{\rm e}/WI_{\rm sat})(\Gamma/2) = 40$ s^{-1}, where $\Gamma \sim 1.5 \times 10^6$ s^{-1} for $6s^2\ ^1S_0 - 6s6p\ ^3P_1$ in solid Ne (Section 4.4).

Now let us consider the perturbation of the crystal field on the hyperfine interaction in Yb. The crystal field does not change the structure of $6s^2\ ^1S_0$ ($F = 1/2$) while its effect on $6s6p\ ^3P_1$ is described by

$$\mathscr{H}_{\rm HFI+CF} = A\boldsymbol{I}\cdot\boldsymbol{J'} + U(\boldsymbol{r}), \tag{5.4}$$

where $U(\boldsymbol{r})$ is the crystal-field potential. Because the crystal field only acts on the electrons, we first seek the matrix representation of $U(\boldsymbol{r})$ in the 3D subspace $J' = 1$ and then use a Kronecker product ($\otimes$) to promote it to the 6D subspace $I = 1/2 \otimes J' = 1$. It is shown in Appendix G that the matrix representation of the crystal field in the $J' = 1$ subspace can be parametrized by three real amplitudes a_0, a_1, and a_2 and two real phases ϕ_1 and ϕ_2

$$U^{(1)} = \frac{1}{\sqrt{2\pi}}\begin{pmatrix} -\sqrt{\frac{1}{10}}a_0 & -\sqrt{\frac{3}{10}}a_1 e^{-i\phi_1} & -\sqrt{\frac{6}{10}}a_2 e^{-i\phi_2} \\ -\sqrt{\frac{3}{10}}a_1 e^{i\phi_1} & \sqrt{\frac{4}{10}}a_0 & \sqrt{\frac{3}{10}}a_1 e^{-i\phi_1} \\ -\sqrt{\frac{6}{10}}a_2 e^{i\phi_2} & \sqrt{\frac{3}{10}}a_1 e^{i\phi_1} & -\sqrt{\frac{1}{10}}a_0 \end{pmatrix}. \tag{5.5}$$

We then find the matrix representation of Hamiltonian (5.4) in the 6D subspace and numerically find its eigenstates $|\lambda_i\rangle$ ($i = 1, 2, \cdots 6$) given a set of crystal-field parameters.

To estimate the size of the parameters a_0, a_1, and a_2, or essentially the energy scale of the crystal field, we use the field strength obtained in Section 4.4 (27 MV/m) and use the

atomic radius of Yb (1.76 Å [25]) as the length scale. Therefore a_0, a_1, and a_2 are on the order of $\sqrt{2\pi} \cdot e \cdot 27$ MV/m $\cdot$ 1.76 Å = 12 meV = 96 cm^{-1} = $720A$. At large fields $a_i \gg A$, the spectrum of Hamiltonian (5.4) typically splits into three levels, and each level further splits into two hyperfine levels.

At the presence of the crystal field, the calculation of the pumping rate for nuclear polarization [80] is based on the same principle discussed earlier. The difference is that we need to sum over all the new eigenstates $|\lambda\rangle$ in the excited level. The absorption probability of $|M_F = -1/2\rangle \rightarrow |\lambda\rangle$ is $|\langle M_I = -1/2, M'_J = +1|\lambda\rangle|^2$. The decay probability of $|M_F = +1/2\rangle \leftarrow |\lambda\rangle$ is $\sum_{M'_J} |\langle M_I = +1/2, M'_J|\lambda\rangle|^2$. Therefore the pumping rate of $|M_F = -1/2\rangle \rightarrow |M_F = +1/2$ through $|\lambda\rangle$ is

$$\Gamma_{\mathrm{e}} \cdot |\langle M_I = -1/2, M'_J = +1|\lambda\rangle|^2 \cdot \textstyle\sum_{M'_J} |\langle M_I = +1/2, M'_J|\lambda\rangle|^2. \tag{5.6}$$

We then sum over all six $|\lambda_i\rangle$ to get the total pumping rate of $|M_F = -1/2\rangle \rightarrow |M_F = +1/2\rangle$

$$\Gamma_{\mathrm{e}} \cdot \sum_{i=1}^{6} \left(|\langle M_I = -1/2, M'_J = +1|\lambda_i\rangle|^2 \cdot \textstyle\sum_{M'_J} |\langle M_I = +1/2, M'_J|\lambda_i\rangle|^2 \right). \tag{5.7}$$

Similarly, the pumping rate of $|M_F = +1/2\rangle \rightarrow |M_F = -1/2\rangle$ is

$$\Gamma_{\mathrm{e}} \cdot \sum_{i=1}^{6} \left(|\langle M_I = +1/2, M'_J = +1|\lambda_i\rangle|^2 \cdot \textstyle\sum_{M'_J} |\langle M_I = -1/2, M'_J|\lambda_i\rangle|^2 \right). \tag{5.8}$$

The difference between the above two rates gives the net pumping rate Γ_{p}.

Given $a_0, a_1, a_2 \sim 720A$, we play with different combinations of the crystal-field parameters. The resultant Γ_{p} is independent of ϕ_1 and ϕ_2 and is roughly on the order of $10^{-5}\Gamma_{\mathrm{e}}$. Compared to $\Gamma_{\mathrm{p}} = 2\Gamma_{\mathrm{e}}/9$ in the case of no crystal field, such a reduction in pumping rate by a factor of 10^4 is identified as the main reason we have not observed the polarization signal.

5.3 Magnetic Dipolar Broadening

The magnetic dipole interaction between spins in a crystal can broaden the linewidth of magnetic resonance, or equivalently decrease the transverse relaxation time. This is because each spin produces its own local magnetic field $\boldsymbol{B}_{\rm loc}$. If the spins are not polarized, then their $\boldsymbol{B}_{\rm loc}$ are randomly oriented with respect to the holding magnetic field $\boldsymbol{B}$, which introduces an effective inhomogeneity to $\boldsymbol{B}$.

The calculation starts with the Hamiltonian $\mathscr{H} = \mathscr{H}_{\rm Z} + \mathscr{H}_{\rm dip,s} + \mathscr{H}_{\rm dip,m}$ that consists of two types of dipoles $\boldsymbol{\mu}_i = \gamma\hbar\boldsymbol{S}_i$ and $\boldsymbol{\mu}'_m = \gamma'\hbar\boldsymbol{S}'_m$ subject to a holding field $\boldsymbol{B} = B\hat{z}$, where $\mathscr{H}_{\rm Z} = \gamma\hbar B S_z$ ($S_z = \sum_i S_{iz}$) is the Zeeman term,

$$\mathscr{H}_{\rm dip,s} = \frac{\mu_0}{4\pi}\gamma^2\hbar^2 \sum_{i<j}\left[\frac{\boldsymbol{S}_i\cdot\boldsymbol{S}_j}{r_{ij}^3} - \frac{3(\boldsymbol{r}_{ij}\cdot\boldsymbol{S}_i)(\boldsymbol{r}_{ij}\cdot\boldsymbol{S}_j)}{r_{ij}^5}\right] \tag{5.9a}$$

is the self term of $\boldsymbol{\mu}_i$ interacting with its own type, and

$$\mathscr{H}_{\rm dip,m} = \frac{\mu_0}{4\pi}\gamma\gamma'\hbar^2 \sum_{i,m}\left[\frac{\boldsymbol{S}_i\cdot\boldsymbol{S}'_m}{r_{im}^3} - \frac{3(\boldsymbol{r}_{im}\cdot\boldsymbol{S}_i)(\boldsymbol{r}_{im}\cdot\boldsymbol{S}'_m)}{r_{im}^5}\right] \tag{5.9b}$$

is the mutual term of $\boldsymbol{\mu}_i$ and $\boldsymbol{\mu}'_m$ interacting with each other. The goal is to calculate the absorption linewidth $\Delta\omega$ of a transverse field $\boldsymbol{B}_\perp(t) = B_\perp\hat{x}\cos\omega t$ due to the $\boldsymbol{\mu}_i$ dipoles via the coupling $\mathscr{H}_\perp = \gamma\hbar B_\perp S_x\cos\omega t$ ($S_x = \sum_i S_{ix}$). In $\mathscr{H}$, similar terms like $\mathscr{H}'_{\rm Z}$ and $\mathscr{H}'_{\rm dip,s}$ have already been omitted because we are interested in how $\boldsymbol{\mu}'_m$ affect the absorption linewidth of $\boldsymbol{\mu}_i$ rather than $\boldsymbol{\mu}'_m$'s own absorption linewidth. The absorption lineshape is described by the distribution $f(\omega) = \sum_{\lambda_1,\lambda_2}|\langle\lambda_1|S_x|\lambda_2\rangle|^2\delta(\lambda_1-\lambda_2-\hbar\omega)$, where $\lambda_{1,2}$ are eigenvalues of $\mathscr{H}$. Of course, it is formidable to figure out all the eigenvalues of $\mathscr{H}$, but the second moment of the distribution f can be readily computed without solving $\mathscr{H}$ due to the invariance of the trace [81],

$$\langle\Delta\omega^2\rangle_f = \langle\omega^2\rangle_f - \langle\omega\rangle_f^2 = -\frac{{\rm Tr}\left([\mathscr{H},S_x]^2\right) + {\rm Tr}^2\left([\mathscr{H},S_x]S_x\right)}{\hbar^2{\rm Tr}\left(S_x^2\right)}. \tag{5.10}$$

When calculating the commutators and the traces, we should only keep terms in $\mathscr{H}$ that commute with S_z. Inclusion of terms that do not commute with S_z will create subsidiary absorption peaks at $\omega = 0, 2\gamma B, (2\gamma - \gamma')B, \cdots$, and thus the second moment does not truly reflect the width of the main peak at $\omega = \gamma B$. The retained terms are $\mathscr{H}_{\rm Z}$ itself,

$$\mathscr{H}^0_{\rm dip,s} = \frac{\mu_0}{4\pi}\gamma^2\hbar^2 \sum_{i<j} \frac{1 - 3\cos^2\theta_{ij}}{r_{ij}^3} \left(\frac{3}{2} S_{iz} S_{jz} - \frac{1}{2} \boldsymbol{S}_i \cdot \boldsymbol{S}_j \right), \tag{5.11a}$$

$$\text{and } \mathscr{H}^0_{\rm dip,m} = \frac{\mu_0}{4\pi}\gamma\gamma'\hbar^2 \sum_{i,m} \frac{1 - 3\cos^2\theta_{im}}{r_{im}^3} (S_{iz} S'_{mz}), \tag{5.11b}$$

where θ_{ij} (θ_{im}) are the angles between $\boldsymbol{r}_{ij}$ ($\boldsymbol{r}_{im}$) and $\boldsymbol{B}$. After some lengthy calculations, we get $\langle \Delta\omega^2 \rangle_f = \langle \Delta\omega^2 \rangle_{f,\rm s} + \langle \Delta\omega^2 \rangle_{f,\rm m}$, where

$$\langle \Delta\omega^2 \rangle_{f,\rm s} = \frac{3}{2} \left(\frac{\mu_0}{4\pi} \right)^2 \gamma^4 \hbar^2 S(S+1) \frac{1}{N} \sum_{i<j} \frac{(1 - 3\cos^2\theta_{ij})^2}{r_{ij}^6} \tag{5.12a}$$

$$\text{and } \langle \Delta\omega^2 \rangle_{f,\rm m} = \frac{2}{3} \left(\frac{\mu_0}{4\pi} \right)^2 \gamma^2\gamma'^2 \hbar^2 S'(S'+1) \frac{1}{N} \sum_{i,m} \frac{(1 - 3\cos^2\theta_{im})^2}{r_{im}^6}. \tag{5.12b}$$

The sums in the above equations can be further calculated. It is reasonable to assume that all the $\boldsymbol{\mu}_i$ sites are equivalent, so that the sums over j and m are independent of i, and thus $\sum_{i<j} = \frac{N}{2} \sum_j$ and $\sum_{i,m} = N \sum_m$. These sums only include lattice sites that are occupied by magnetic dipoles. To convert to sums that include all the lattices sites, we need to insert the dilution factor ξ so that $\sum_j = \xi \sum_{\mathbf{R}}$ and $\sum_m = \xi' \sum_{\mathbf{R}}$, where $\mathbf{R}$ are the lattice vectors. Since our samples are at best polycrystalline, we can first average the angular factor over a sphere $\frac{1}{4\pi} \int \mathrm{d}\Omega (1 - 3\cos^2\theta)^2 = \frac{4}{5}$. The remaining sum over all lattice sites is $\sum_{\mathbf{R}} r(\mathbf{R})^{-6} = 14.45 \cdot n^2/2$ for face-centered-cubic lattice, where n is the number density of the lattice sites [22]. Combining all the factors, we get

$$\langle \Delta\omega^2 \rangle_{f,\rm s} = 14.45 \cdot \frac{3}{10} \left(\frac{\mu_0}{4\pi} \right)^2 \gamma^4 \hbar^2 S(S+1) \xi n^2 \tag{5.13a}$$

$$\text{and } \langle \Delta\omega^2 \rangle_{f,\mathrm{m}} = 14.45 \cdot \frac{4}{15} \left(\frac{\mu_0}{4\pi} \right)^2 \gamma^2 \gamma'^2 \hbar^2 S'(S'+1) \xi' n^2. \tag{5.13b}$$

With $\xi(^{171}\mathrm{Yb}) \sim 14.28\% \times 1$ ppm, $\xi(^{173}\mathrm{Yb}) \sim 16.13\% \times 1$ ppm, and $\xi(^{21}\mathrm{Ne}) = 0.27\%$, their contributions to the second moment are $(0.72 \text{ rad/s})^2$, $(0.65 \text{ rad/s})^2$, and $(94 \text{ rad/s})^2$, respectively. Assuming that the lineshape is Gaussian, the transverse relaxation time is defined as $T_2 = \langle \Delta\omega^2 \rangle_f^{-1/2}$. In our case, $T_2 = 10.6$ ms, dominated by the ^{21}Ne nuclear spins [82]. Using $\Gamma_\mathrm{p} \sim 1 \times 10^{-5} \Gamma_\mathrm{e} = 4 \times 10^{-4}$ s^{-1} from the previous section, we are in the $\Gamma_\mathrm{p} T_2 \ll 1$ regime where $D_\mathrm{m} \sim 50\%$ and $P_\mathrm{m} \sim 1.3 \times 10^{-6}$.

5.4 SQUID Detection

In Figure 5.2, the absorption probability of σ_+ light is the same from $|M_F = \pm 1/2\rangle$ in the ground level to the $F' = 1/2$ and $3/2$ excited levels. Therefore given that the hyperfine structure of ^{171}Yb is not resolved in solid Ne, it is impossible to detect the nuclear polarization using the dark-state method. One alternative optical detection method is the nuclear spin optical rotation [83] which will not be discussed here. Instead, we use a SQUID magnetometer to detect the bulk magnetization of our nuclear spin polarized samples. SQUIDs, short for Superconducting QUantum Interference Devices, are the most sensitive magnetic flux detectors. This device, operating at cryogenic temperatures with quantum-limited sensitivity, has demonstrated field resolution at the 10^{-13} G level. A review on the principles of SQUID sensors is given in Reference [84].

We use a STAR Cryoelectronics SQUID system that consists of a low-T_c dc SQUID (SQ1200 LTS), a single-channel SQUID controller (PC-100), and a shielded cryocable (CBL-C2-10-1). Low-T_c SQUIDs with their internal circuits made of Nb need be cooled below its transition temperature 9.2 K in order to work properly. In our liquid He cryostat, we install the SQUID on the cold surface using a copper mount (Figure 5.3). To minimize the heat load on the SQUID, the cryocable that connects the SQUID and the room-temperature electronics system is also heatsinked by the cold surface and the liquid N_2 shield.

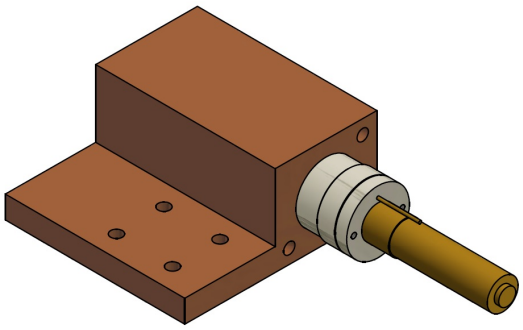

Figure 5.3: A sketch of the SQUID mount with the STAR Cryoelectronics SQUID installed. Image courtesy of T. O'Connor.

An external magnetic field is probed by the SQUID through a pick-up coil also made of Nb. The magnetic flux in the pick-up coil is coupled to the internal SQUID loop by a flux transformer. Typically, only about 1% of the external flux is transferred to the SQUID due to the low mutual inductance. Figure 5.4(a) shows a sketch of the cylindrical sapphire substrate used in optical pumping experiments. Yb/Ne samples are grown on one flat surface of the cylinder, and one pick-up loop is shown wound around the cylinder. Given a uniform polarization across the sample, the flux Φ in this pick-up loop is

$$\Phi(d) = \Phi_{\mathrm{s}} \int_0^1 \mathrm{d}x \int_0^{2\pi} \mathrm{d}\phi \frac{x(1 - x\cos\phi)}{(1 - 2x\cos\phi + x^2 + (d/R)^2)^{3/2}}, \tag{5.14}$$

where d is the distance between the sample and the loop, R is the radius of the cylinder, and Φ_{s} is independent of d and has the dimension of magnetic flux (Appendix H).

When R is fixed, Φ/Φ_{s} shows a rapid decay as d increases (Figure 5.4(b)). This makes it feasible to implement a first order gradiometer as the pick-up coil which is less sensitive to any far-field noise than a zeroth order gradiometer (a single loop). Appendix I describes the construction of (axial) gradiometers of arbitrary orders. In the case of the first order gradiometer, the net flux in the pick-up coil is $N\Phi(d_+) - N\Phi(d_-)$, where N is the number of turns of each loop and $d_\pm$ are the distances from the sample to the two counter-wound loops. The typical dimensions are $N = 2$, $R = 1.27$ cm, $d_+ = 0.1$ cm, and $d_- = 0.6$ cm, and thus $\Phi(d_-) = 0.36\Phi(d_+)$, which means that most of the local flux signal is picked up.

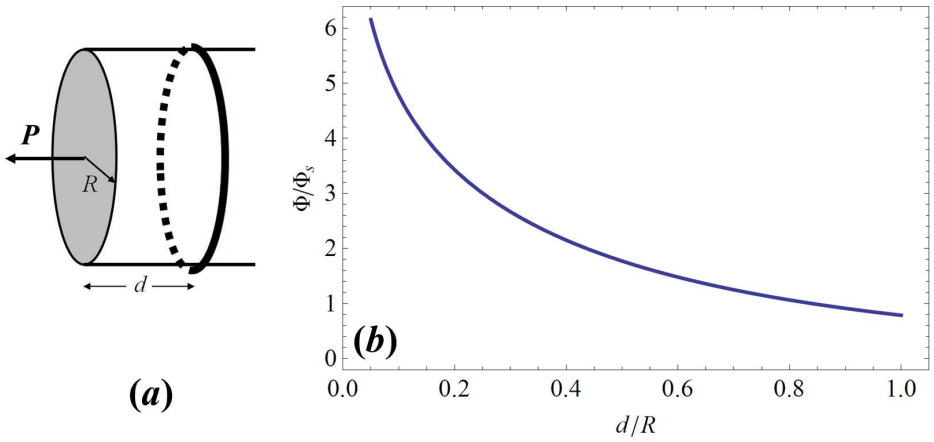

Figure 5.4: (a) A sketch of the cylindrical substrate used in optical pumping experiments. The Yb/Ne sample is grown on one end of the cylinder and a pick-up loop is wound around the cylinder with a distance d away from the sample. (b) The magnetic flux from a polarized sample in the pick-up loop Φ as a function of d. The polarization is assumed to be uniform and along the common axis.

The scale of the flux in the pick-up coil is roughly determined by $\Phi_{\rm s} = \frac{1}{2}\mu_0\mu n_{2,\mu}R$, where μ is the magnetic moment of spins and $n_{2,\mu}$ is their 2D density (Appendix H). In our case, μ is the nuclear magnetic moment of ^{171}Yb and $n_{2,\mu} = n_{2,^{171}\rm Yb}P$, where $n_{2,^{171}\rm Yb}$ is the 2D density of ^{171}Yb and P is the polarization of ^{171}Yb. If we grow the sample with natural Yb at the rate $\mathrm{d}s_{\rm Ne}/\mathrm{d}t = 50$ μm/hr and the Yb/Ne dilution factor $\xi = 1$ ppm for five hours, then $n_{2,^{171}\rm Yb} \sim 1.6 \times 10^{14}$ cm^{-2} (Section 2.4). P is estimated in the previous section to be 1.3×10^{-6}. Then $\Phi_{\rm s} = 2.1 \times 10^{-8}\Phi_0$, where $\Phi_0 = h/(2e) = 2.1 \times 10^{-15}$ Wb is the magnetic flux quantum. Together with the number of turns, the numerical factor from the integral in Equation (5.14), and the coupling efficiency of the SQUID, the flux in the SQUID loop is only about $2 \times 10^{-9}\Phi_0$.

We have also measured the SQUID noise. When the SQUID input is internally shorted by a Nb wire, the SQUID puts out its intrinsic noise. The noise density is typically about 5×10^{-6} $\Phi_0/\sqrt{\rm Hz}$ below the 5 kHz bandwidth of the SQUID (Figure 5.5, blue curve). When the input is connected to a pick-up coil, the spectrum reflects the magnetic Johnson noise of the copper pieces close to the pick-up coil, which exhibits a higher base level that rolls off at high frequencies (Figure 5.5, red curve). The spikes in the spectrum are mostly the 60 Hz

noise and its harmonics in the power line. Our holding field is about 4 G and thus the Larmor frequency of ^{171}Yb is about 3 kHz where the noise density is about 2.5×10^{-5} $\Phi_0/\sqrt{\text{Hz}}$. When the pick-up coil is not sufficiently cooled, an even higher base level is observed due to the electric Johnson noise of the wire (Figure 5.5, green curve).

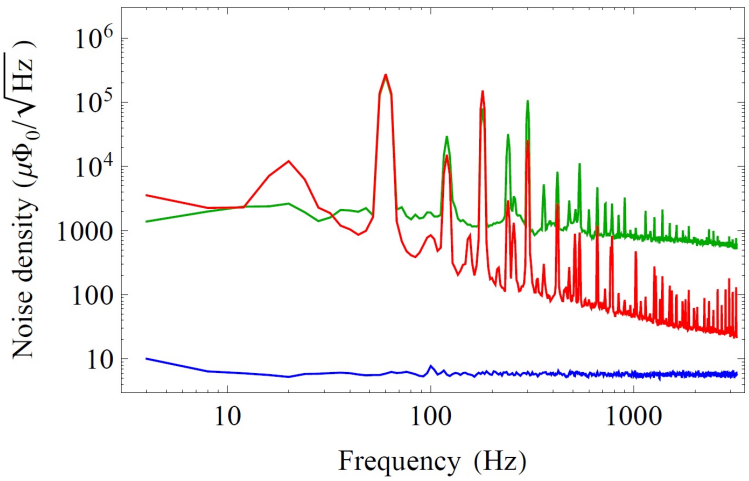

Figure 5.5: The flux noise spectra of the STAR Cryoelectronics SQUID. Blue curve: the intrinsic flux noise measured with the SQUID input shorted. Red cure: the flux noise when a first-order-gradiometer pick-up coil is attached. Green curve: the flux noise when the pick-up coil is not sufficiently cooled.

Compared to the estimated signal, even the intrinsic noise level of the SQUID seems overwhelmingly high that there is no chance detecting the polarization as it stands. Ways to improve the signal-to-noise ratio include getting a more powerful laser to increase the optical pumping rate, using the ^{21}Ne-depleted Ne gas to grow the matrix, and replacing the copper pieces in the cryostat with non-metallic but thermally conductive materials.

CHAPTER 6

OUTLOOK

I would like to propose a few experiments to further understand the interaction between the Yb impurities and the Ne lattice and to work toward polarizing nuclear spins of diamagnetic atoms trapped in noble-gas solids by optical pumping.

1. Lineshape of La Transitions in Solid Ne

We have established a one-to-one correspondence between the Yb transitions $4f^{14}6s^2\ {}^1S_0 - 4f^{13}5d6s^2\ (j_1, j_2)_1$ and the La transitions $5d6s^2\ {}^2D_{j_2} - 4f6s^2\ {}^2F_{j_1}$, where $j_1 = 5/2, 7/2$ and $j_2 = 3/2, 5/2$ (Section 3.4.2). Absorption spectroscopy on the La transitions in solid Ne will provide more insights to the broadening of inner-shell transitions and the splitting of atomic levels in solid Ne. The La $5d6s^2\ {}^2D_{5/2}$ level is not thermally populated, but it is metastable and can be populated by driving the $5d6s^2\ {}^2D_{3/2} \rightarrow 4f6s^2\ {}^2D_{5/2}$ transition so that the transitions from La $5d6s^2\ {}^2D_{5/2}$ can also be probed.

2. Single Atom Detection of Yb in Solid Ne

Due to the enhanced intersystem crossing of Yb in solid Ne (Section 3.3.2), Yb atoms are able to give off strong green fluorescence under the blue excitation. Basic signal-to-noise ratio calculations show that optical detection of single Yb atoms in solid Ne is feasible [85]. This project is in preparation for the single atom detection of Mg in solid Ne with the application of measuring the cross-section of the nuclear astrophysical reaction $^{22}\mathrm{Ne}(\alpha, \mathrm{n})^{25}\mathrm{Mg}$ [86].

3. Hyperfine Quenching Rate in ^{87}Sr

^{87}Sr optical clocks operate with the $5s^2\ {}^1S_0 - 5s5p\ {}^3P_0$ transition [87]. However, similar to the ^{171}Yb case, the hyperfine quenching rate of this transition has not been measured before either. The measurement of this rate in a solid matrix should be feasible using the techniques we have developed (Chapter 4). However, the Sr intersystem crossing $5s5p\ {}^3P \leftarrow 5s5p\ {}^1P_1$ is likely to be less enhanced in solid Ne than Yb due to a larger energy difference between $5s5p\ {}^1P_1$ and $4d5s\ {}^3D$. The hyperfine quenching in Sr is also weaker than that in Yb, and thus the intrinsic decay rate may experience a larger medium correction.

4. Dependence of Yb Lifetime on the Index of Refraction

To make a more decisive measurement of the spontaneous emission rate as a function of the index of refraction, one can combine the matrix-isolation technique with the diamond-anvil-cell technique [88]. Yb atoms can be implanted into solid Ne by laser ablation and the index of refraction of solid Ne can be changed by the pressure in the cell. Measurement of the decay rate of $6s^2\ ^1S_0 - 6s6p\ ^3P_1$ in solid Ne has been demonstrated (Section 4.4). The index of refraction of solid Ne can be measured using the interference principle [74].

5. Hanle Effect of Yb Decay in Solid Ne

One way to investigate if an electronic polarization has been established in the excited level is to study the Hanle effect [89]. The suitable transition for this study is again $6s^2\ ^1S_0 - 6s6p\ ^3P_1$ with a decay rate of $\Gamma \sim 1.5 \times 10^6\ \mathrm{s}^{-1}$. The gyromagnetic ratio of $6s6p\ ^3P_1$ is $\gamma/2\pi \sim 1.4 \times 10^6$ Hz/G. Therefore if we expose Yb/Ne samples in a 5 G field, the Hanle effect should be most likely observed. The reduced contrast of the oscillation should tell us about the transverse relaxation time of the electronic spin.

6. Relaxation Times of ^{171}Yb Nuclei in Solid Ne

One way to get a large polarization of ^{171}Yb nuclei in solid Ne is to polarize ^{171}Yb in the beam and freeze the atoms in noble-gas solids. It has been shown that a large fraction of nuclear polarization is unaffected by the freezing [90]. Once we have a nuclear spin polarized sample, we can apply all sorts of techniques in pulsed nuclear magnetic resonance to study the nuclear-spin relaxation.

APPENDIX A

LIQUID HE DEWAR AND TRANSFER

A portable liquid He dewar is equipped with three ball valves, three pressure relief valves, a burst disk, and a pressure gauge for its pressure control and safety (Fig. A.1).

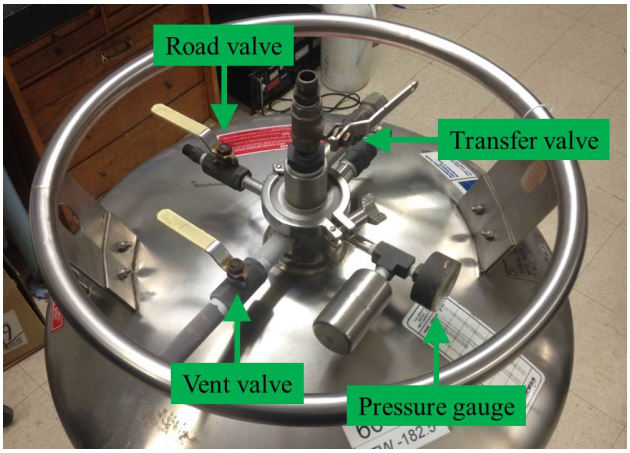

Figure A.1: A picture of a portable liquid He dewar with three ball valves illustrated.

The three ball valves are the transfer valve, the road valve and the vent valve. The transfer valve located at the vertical transfer port controls the access to liquid He. The transfer line cannot be inserted into the dewar unless the transfer valve is open. The road valve together with the 0.5 psig pressure relief valve regulates the dewar pressure. In normal status, the road valve is open. During the transfer, the road valve is closed for the pressure build-up. The vent valve opens or closes the vent port which is used to externally pressurize the dewar during the transfer and relieve the pressure after the transfer.

The three pressure relief valves are 0.5, 10, and 15 psig, respectively. The 0.5 psig valve regulates the dewar pressure in normal status. This amount of overpressure allows liquid He to evaporate at a slower rate. The 10 and 15 psig valves and the burst disk provide pressure safety during the transfer. They cannot be disabled by closing any ball valves. Note that the maximal pressure an average portable dewar can hold is about 15 psig.

Before transferring liquid He, make sure there are at least two trained experimenters present, face masks and gloves are worn, and doors and windows are open for ventilation.

Step 1: Deplete liquid N_2 in the liquid He vessel

(1) Attach the T-shaped tube to the liquid He port of the cryostat.

(2) Insert the 3/8" stainless steel tube all the way into the liquid He vessel through the transfer port of the T-shaped tube.

(3) Connect the vent port of the T-shaped tube to a He gas bottle after purging the gas line for at least 10 seconds.

(4) Start flowing He gas from the gas bottle to the liquid He vessel to expel the liquid N_2.

(5) Once the stainless steel tube starts blowing out white plume instead of liquid N_2, the liquid N_2 in the liquid He vessel has been depleted. Stop flowing He gas.

(6) If the temperature of the liquid He vessel climbs up to higher than 120 K, it needs to be precooled with liquid N_2 again.

(7) Disconnect the gas line, withdraw the stainless steel tube, and detach the T-shaped tube.

(8) Cover the liquid He port of the cryostat so that the He gas inside cannot escape.

Step 2: Build up the pressure of the liquid He dewar

(1) Make sure the initial status of all the valves is correct. The vent valve and the transfer valve are closed, and the road valve is open.

(2) Open the vent valve to release the 0.5 psig pressure and then close. Close the road valve.

(3) Slide the adapter nut to 10" from the end of the transfer line, open the transfer valve, insert the transfer line into the dewar through the transfer port, and tighten the nut.

(4) Monitor the pressure gauge on the dewar, and continue to slowly insert the transfer line until the pressure reaches 5$\sim$10 psig.

(5) If the pressure cannot reach 5$\sim$10 psig, proceed to Step 4(1) for external pressurization.

(6) If the pressure goes above 10 psig, the 10 psig pressure relief valve will be triggered. Crack open the vent valve to help release the pressure until it falls back to 5$\sim$10 psig.

(7) Make sure the transfer line almost touches the bottom of the dewar and the pressure is stable at 5$\sim$10 psig.

(8) Wait and watch the outlet of the transfer line. Initially, there is a gentle gas-flowing

sound which will get louder until the white plume blows out about 10 minutes later. Now it is ready to transfer liquid He to the cryostat.

Step 3: Transfer liquid He to the liquid He vessel

(1) Uncover the liquid He port of the cryostat and attach the T-shaped tube.

(2) Insert the transfer line into the liquid He vessel through the T-shaped tube until it almost touches the bottom. Tighten the adapter nut, and now liquid He is being transferred.

(3) Initially, there is strong white plume blowing from the vent port of the T-shaped tube, which indicates that liquid He is cooling down the vessel.

(4) After about 5 minutes, the white plume becomes significantly weaker which indicates that liquid He starts collecting in the vessel.

(5) After 30∼45 minutes, the white plume becomes strong again and unstable, and liquid air is dripping from the vent port. This indicates that the liquid He vessel is full.

(6) Detach the T-shaped tube together with the transfer line from the liquid He port.

(7) If the dewar is externally pressurized, proceed to Step 4(4).

(8) Crack open the vent valve to release pressure of the dewar. After the pressure falls back to 0 psig, withdraw the transfer line from the liquid He dewar.

(9) Open the road valve and close the transfer valve and the vent valve. The liquid He transfer is finished.

Step 4: Externally pressurize the liquid He dewar

(1) Crack open the vent valve to purge the vent port with the He vapor inside the dewar.

(2) Connect the vent port to a He gas bottle after purging the gas line for at least 10 seconds.

(3) Increase the pressure of the gas regulator to 5∼10 psig and fully open the vent port of the dewar. Now the pressure of the dewar is maintained by the He gas bottle. The pressure gauge on the dewar should read the same pressure as the regulator. Proceed to Step 2(6).

(4) Close the vent valve and turn off the supply from the gas bottle. Disconnect the gas line from the vent port. Proceed to Step 3(8).

APPENDIX B

RUSSEL-SAUNDERS COUPLING IN YB

The excitations of the two $6s$ electrons in Yb are well approximated by the Russel-Saunders coupling scheme, or the LS coupling scheme. In this scheme, the spin-orbit interaction can be considered as a perturbation to the residual Coulomb interaction. Therefore, we first construct the orbital wave functions that diagonalize the residual Coulomb interaction. Due to the Fermi statistics, the constructed wave functions must have exchange symmetry.

Note that given two single-electron states $n_1 l_1$ and $n_2 l_2$, we can put either electron in the first state and the other in the second. Therefore in the uncoupled scheme, the basis vectors come in two groups

$$|\psi^{(1)}_{n_1 l_1 m_1}\psi^{(2)}_{n_2 l_2 m_2}\rangle,\ |\psi^{(1)}_{n_2 l_2 m_2}\psi^{(2)}_{n_1 l_1 m_1}\rangle. \tag{B.1}$$

In the LS coupling scheme, the new basis vectors are eigenstates of the total angular momenta $\hat{\boldsymbol{L}}^2 = (\hat{\boldsymbol{l}}_1 + \hat{\boldsymbol{l}}_2)^2$ and $\hat{L}_z = \hat{l}_{1z} + \hat{l}_{2z}$

$$|LM_L\rangle_1 = \sum_{m_1,m_2} C(LM_L; l_1 m_1 l_2 m_2)|\psi^{(1)}_{n_1 l_1 m_1}\psi^{(2)}_{n_2 l_2 m_2}\rangle, \tag{B.2a}$$

$$|LM_L\rangle_2 = \sum_{m_1,m_2} C(LM_L; l_1 m_1 l_2 m_2)|\psi^{(1)}_{n_2 l_2 m_2}\psi^{(2)}_{n_1 l_1 m_1}\rangle, \tag{B.2b}$$

where $C(LM_L; l_1 m_1 l_2 m_2)$ are the Clebsch-Gordon coefficients. Since $|LM_L\rangle_{1,2}$ are related by swapping the two electrons, the exchange symmetric and antisymmetric orbital wave functions are

$$|LM_L\rangle_\pm = (|LM_L\rangle_1 \pm |LM_L\rangle_2)/\sqrt{2}, \tag{B.3}$$

which happen to diagonalize the residual Coulomb interaction.

The spin wave functions with exchange symmetry are simply the triplet and the singlet states $|SM_S\rangle_\pm$. Therefore the total wave functions $|LM_L SM_S\rangle$ which must be exchange

antisymmetric are

$$|LM_L\rangle_+|SM_S\rangle_-,\ |LM_L\rangle_-|SM_S\rangle_+. \tag{B.4}$$

These states, abbreviated as terms ^{2S+1}L, are eigenstates of the parity $\hat{P}$, the angular momenta $\hat{\boldsymbol{L}}^2$, $\hat{\boldsymbol{S}}^2$, $\hat{L}_z$ and $\hat{S}_z$, and the Hamiltonian $\hat{H}$ with the spin-orbit interaction ignored

$$\hat{P}|LM_LSM_S\rangle = (-1)^{l_1+l_2}|LM_LSM_S\rangle, \tag{B.5a}$$

$$\hat{\boldsymbol{L}}^2|LM_LSM_S\rangle = L(L+1)\hbar^2|LM_LSM_S\rangle, \tag{B.5b}$$

$$\hat{\boldsymbol{S}}^2|LM_LSM_S\rangle = S(S+1)\hbar^2|LM_LSM_S\rangle, \tag{B.5c}$$

$$\hat{L}_z|LM_LSM_S\rangle = M_L\hbar|LM_LSM_S\rangle, \tag{B.5d}$$

$$\hat{S}_z|LM_LSM_S\rangle = M_S\hbar|LM_LSM_S\rangle, \tag{B.5e}$$

$$\hat{H}|LM_LSM_S\rangle = E(L,\pm)|LM_LSM_S\rangle. \tag{B.5f}$$

Here are two examples. (1) The configuration $6s6p$ ($l_1 = 0, l_2 = 1$) of Yb has an odd parity since $l_1 + l_2 = 1$. Such a configuration leads to two terms ^1P and ^3P since L can only be 1. According to Hund's rule, ^3P has a lower energy due to its larger multiplicity $2S + 1$. (2) The configuration $6p^2$ ($l_1 = l_2 = 1$) has an even parity since $l_1 + l_2 = 2$. When two electrons have the same n and l, it can be shown from the properties of Clebsch-Gordon coefficients that $|LM_L\rangle_1 = (-1)^{2l-L}|LM_L\rangle_2$. For $l_1 = l_2 = 1$, in principle we can have $L =$ 0, 1 or 2. But when $L = 0$ or 2, the antisymmetric state $|L, M_L\rangle_-$ vanishes, whereas when $L = 1$, the symmetric state $|L, M_L\rangle_+$ vanishes. Therefore the allowed terms for $6p^2$ are ^1S, ^1D and ^3P, among which ^3P has the lowest energy.

APPENDIX C

STARK MIXING BY CRYSTAL FIELD

The crystal field in solid Ne can induce Stark mixing between atomic states of Yb atoms. The matrix element of $\mathscr{H}_{\rm S} = e\sum_m E_m r_m$ between two states $|J_1 M_1\rangle$ and $|J_2 M_2\rangle$ is

$$\langle J_1 M_1|\mathscr{H}_{\rm S}|J_2 M_2\rangle = e\sum_m E_m \langle J_1 M_1|r_m|J_2 M_2\rangle = e\sum_m E_m \frac{\langle J_1||r||J_2\rangle}{\sqrt{2J_1+1}}\langle J_2 M_2; 1m|J_1 M_1\rangle, \tag{C.1}$$

where the Wigner-Eckart theorem is applied to obtain the last equality, $\langle J_1||r||J_2\rangle$ is the reduced matrix element of the dipole operator, and $\langle J_2 M_2; 1m|J_1 M_1\rangle$ are the Clebsch-Gordan coefficients. Reduced matrix elements between eleven low-lying Yb levels are calculated [67].

We can define the coupling between two levels as an incoherent sum of couplings between two states,

$$|\langle J_1|\mathscr{H}_{\rm S}|J_2\rangle|^2 \equiv \sum_{M_1 M_2} |\langle J_1 M_1|\mathscr{H}_{\rm S}|J_2 M_2\rangle|^2 . \tag{C.2}$$

In expanding the square on the right-hand side with $\mathscr{H}_{\rm S} = e\sum_m E_m r_m$, we get terms that look like $e^2\sum_{m,m'} E_m E^*_{m'}\langle J_1 M_1|r_m|J_2 M_2\rangle\langle J_1 M_1|r_{m'}|J_2 M_2\rangle^*$. Since the solid Ne samples we grow are at best polycrystalline, the crystal field is randomly oriented within one sample. Therefore it is legitimate to first carry out an average over the crystal-field orientation and replace $E_m E^*_{m'}$ by $(E^2/3)\delta_{mm'}$, where E is the mean magnitude of the crystal field in solid Ne. We then are left with

$$|\langle J_1|\mathscr{H}_{\rm S}|J_2\rangle|^2 = \frac{e^2E^2}{3}\sum_{M_1 M_2 m} |\langle J_1, M_1|r_m|J_2, M_2\rangle|^2. \tag{C.3}$$

To proceed the calculation with the Wigner-Eckart theorem, we utilize the orthogonality of Clebsch-Gordan coefficients $\sum_{M_2 m}|\langle J_2 M_2; 1m|J_1 M_1\rangle|^2 = 1$. We finally have

$$|\langle J_1|\mathscr{H}_{\rm S}|J_2\rangle|^2 = \frac{e^2E^2}{3}|\langle J_1||r||J_2\rangle|^2 \text{ or simply } \langle J_1|\mathscr{H}_{\rm S}|J_2\rangle = \frac{eE}{\sqrt{3}}\langle J_1||r||J_2\rangle. \tag{C.4}$$

With the coupling between levels properly defined, we can calculate how the crystal field perturbs the atomic levels. For the diagonal part, we inherit the atomic Hamiltonian for a free Yb atom. We diagonalize the perturbed Hamiltonian and find the new eigenstates. In particular, the admixture of $6s6p\ ^3P_1$ in $6s6p\ ^3P_0$ makes the dominant contribution to the induced decay rate of $6s6p\ ^1S_0 \leftarrow 6s6p\ ^3P_0$ for even Yb isotopes in solid Ne.

The spontaneous emission rate from one level $|J_1\rangle$ to another level $|J_2\rangle$ is the same as from any state $|J_1 M_1\rangle$ to the level $|J_2\rangle$, which is given by

$$\Gamma = \frac{e^2\omega_0^3}{3\pi\epsilon_0\hbar c^3}\sum_{M_2}|\langle J_1 M_1|r_{M_1-M_2}|J_2 M_2\rangle|^2 = \frac{e^2\omega_0^3}{3\pi\epsilon_0\hbar c^3(2J_1+1)}|\langle J_1||r||J_2\rangle|^2. \tag{C.5}$$

Suppose $(^3P_0)_\mathrm{m} \simeq (^3P_0)_\mathrm{v} + \beta(E)(^3P_1)_\mathrm{v} + \cdots$ and $(^1S_0)_\mathrm{m} \simeq (^1S_0)_\mathrm{v} + \cdots$, and then we have

$$\Gamma[(^1S_0)_\mathrm{m} \leftarrow (^3P_0)_\mathrm{m}] = \frac{e^2\left(\omega[(^1S_0)_\mathrm{m}] - \omega[(^3P_0)_\mathrm{m}]\right)^3}{3\pi\epsilon_0\hbar c^3(2\times 0+1)}\beta^2(E)|\langle(^3P_1)_\mathrm{v}||r||(^1S_0)_\mathrm{v}\rangle|^2. \tag{C.6}$$

In Section 4.2, we find this rate to be about 2×10^{-2} s^{-1} from which the crystal-field strength is calculated to be 27 MV/m. With this field strength, the level-mixing coefficients between eight low-lying levels in Yb are listed in Table C.1.

Table C.1: Level-mixing coefficients between eight low-lying levels in Yb with an electric-field strength $E = 27$ MV/m.

	$(^1S_0)_\mathrm{v}$	$(^3P_0)_\mathrm{v}$	$(^3P_1)_\mathrm{v}$	$(^3P_2)_\mathrm{v}$	$(^3D_1)_\mathrm{v}$	$(^3D_2)_\mathrm{v}$	$(^3D_3)_\mathrm{v}$	$(^1P_1)_\mathrm{v}$
$(^1S_0)_\mathrm{m}$	1	−5E−10	−2E−4	−1E−9	2E−7	3E−7	2E−12	−1E−3
$(^3P_0)_\mathrm{m}$	2E−8	1	8E−5	2E−5	−2E−3	−3E−7	−8E−8	1E−6
$(^3P_1)_\mathrm{m}$	2E−4	−9E−5	1	7E−5	−2E−3	−4E−3	−4E−7	4E−6
$(^3P_2)_\mathrm{m}$	−9E−9	−2E−5	−9E−5	1	−8E−4	−3E−3	−7E−3	5E−6
$(^3D_1)_\mathrm{m}$	−3E−6	2E−3	2E−3	8E−4	1	−3E−4	−4E−5	−3E−3
$(^3D_2)_\mathrm{m}$	−7E−6	5E−7	4E−3	3E−3	2E−4	1	−3E−4	−7E−3
$(^3D_3)_\mathrm{m}$	1E−9	3E−8	8E−7	7E−3	4E−5	2E−4	1	1E−6
$(^1P_1)_\mathrm{m}$	1E−3	6E−6	3E−5	1E−5	3E−3	7E−3	−1E−6	1

APPENDIX D

RATE EQUATIONS FOR EXCITATION DYNAMICS

The dynamics of Yb atoms in solid Ne excited by the 388 nm light can be approximated by a four-level system (Figure D.1). State $|1\rangle$, being the ground state, represents $6s^2\ {}^1S_0$. State $|2\rangle$, being the final state of the transition the excitation light is driving, represents $6s6p\ {}^1P_1$. State $|2\rangle$ can not only directly decay to $|1\rangle$ but through the intermediate states $|3\rangle$ and $|4\rangle$. The branching ratios of $|3\rangle \leftarrow |2\rangle$ and $|4\rangle \leftarrow |2\rangle$ are comparable, but the decay of $|4\rangle$ is much slower than $|3\rangle$. States $|3\rangle$ and $|4\rangle$ represent $6s6p\ {}^3P_{0,1,2}$, with $6s6p\ {}^3P_1$ well described by $|3\rangle$ and $6s6p\ {}^3P_0$ by $|4\rangle$. The classification of $6s6p\ {}^3P_2$ is not clear because it is metastable in vacuum but its slow decay is not observed in solid Ne.

The parameters are assigned as follows. N_i is the population of state $|i\rangle$. The excitation rate of the laser is Γ_e. The decay rate of $|i\rangle \leftarrow |j\rangle$ is Γ_{ij}. The magnitudes of the rates are $\Gamma_\mathrm{e}, \Gamma_{32}, \Gamma_{42}, \Gamma_{13}, \Gamma_{14} \ll \Gamma_{12}$, $\Gamma_{14} \ll \Gamma_{32} \sim \Gamma_{42} \ll \Gamma_{13}$. The rate equations, in accordance with Einstein's treatment of atomic absorption and emission, are

$$\begin{cases} N_1 + N_2 + N_3 + N_4 = 1 \\ \dfrac{\mathrm{d}N_2}{\mathrm{d}t} = \Gamma_\mathrm{e}(N_1 - N_2) - (\Gamma_{12} + \Gamma_{32} + \Gamma_{42})N_2 \\ \dfrac{\mathrm{d}N_3}{\mathrm{d}t} = \Gamma_{32}N_2 - \Gamma_{13}N_3 \\ \dfrac{\mathrm{d}N_4}{\mathrm{d}t} = \Gamma_{42}N_2 - \Gamma_{14}N_4 \end{cases} \tag{D.1}$$

with the initial conditions $N_1(0) = 1$ and $N_2(0) = N_3(0) = N_4(0) = 0$.

Before numerically solving the equations, let us analyze the dynamics. There are three processes involved, $|1\rangle \leftrightarrow |2\rangle$, $|1\rangle \rightarrow |2\rangle \rightarrow |3\rangle \rightarrow |1\rangle$, and $|1\rangle \rightarrow |2\rangle \rightarrow |4\rangle \rightarrow |1\rangle$, each much faster than the next one. Therefore every time we focus on only one process with the dynamics of slower processes ignored. The result of solving a faster process will become a constraint when solving a slower process.

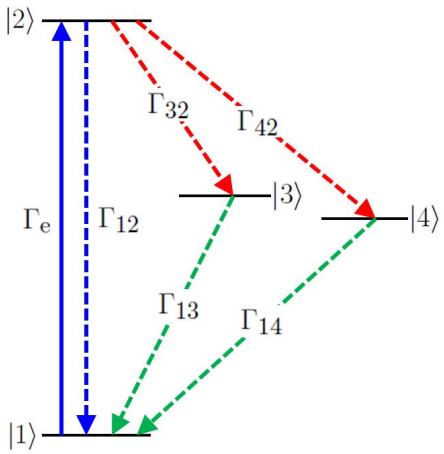

Figure D.1: The energy levels of the rate-equation model that describes the dynamics of Yb atoms in solid Ne when excited by the 388 nm light. The solid upward arrow indicates the optical excitation and the dashed downward arrows indicate the spontaneous decays.

The first process $|1\rangle \leftrightarrow |2\rangle$ is the absorption and emission in a two-level system

$$\begin{cases} N_1 + N_2 = 1 \\ \dfrac{\mathrm{d}N_2}{\mathrm{d}t} = \Gamma_\mathrm{e}(N_1 - N_2) - \Gamma_{12} N_2 \end{cases} \tag{D.2}$$

with initial conditions $N_1(0) = 1$ and $N_2(0) = 0$. The solution is that N_1 (N_2) exponentially decreases (increases) to the equilibrium population $N_2/N_1 = \Gamma_\mathrm{e}/(\Gamma_{12} + \Gamma_\mathrm{e}) \sim \Gamma_\mathrm{e}/\Gamma_{12}$ with a time constant $(\Gamma_{12} + 2\Gamma_\mathrm{e})^{-1} \sim \Gamma_{12}^{-1}$. It implies that after a few Γ_{12}^{-1}, N_2 is locked to N_1 with a ratio of $\Gamma_\mathrm{e}/\Gamma_{12}$ as long as N_1 does not vary at a rate faster than Γ_{12}.

We then use the above constraint in solving the second process $|1\rangle \to |2\rangle \to |3\rangle \to |1\rangle$

$$\begin{cases} N_1 + N_2 + N_3 = 1 \\ \dfrac{\mathrm{d}N_2}{\mathrm{d}t} = \Gamma_\mathrm{e}(N_1 - N_2) - (\Gamma_{12} + \Gamma_{32}) N_2 \\ \dfrac{\mathrm{d}N_3}{\mathrm{d}t} = \Gamma_{32} N_2 - \Gamma_{13} N_3 \end{cases} \quad \Longrightarrow \quad \begin{cases} N_1 + \eta N_1 + N_3 = 1 \\ \dfrac{\mathrm{d}N_3}{\mathrm{d}t} = \Gamma_{32}(\eta N_1) - \Gamma_{13} N_3 \end{cases}, \tag{D.3}$$

where $\eta = N_2/N_1 = \Gamma_\mathrm{e}/\Gamma_{12}$. The initial conditions for the constrained equations are $N_1(0) = (1+\eta)^{-1}$ and $N_3(0) = 0$. The solution is that N_1 (N_3) exponentially decreases (increases) to

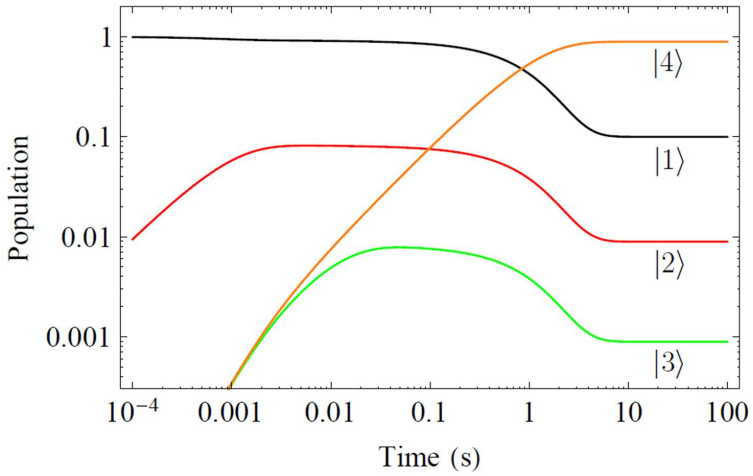

Figure D.2: The solution to the rate equations (D.1) with $\Gamma_e = 10^2$ s^{-1}, $\Gamma_{12} = 10^3$ s^{-1}, $\Gamma_{32} = \Gamma_{42} = 10$ s^{-1}, $\Gamma_{13} = 10^2$ s^{-1}, and $\Gamma_{14} = 10^{-1}$ s^{-1}. The times it takes to reach the equilibrium between different states agree with the breakdown analysis.

the equilibrium population $N_3/N_1 = \eta\Gamma_{32}/\Gamma_{13}$ with a time constant $(\eta\Gamma_{32} + \Gamma_{13})^{-1} \sim \Gamma_{13}^{-1}$. It implies that after a few Γ_{13}^{-1}, N_3 is locked to N_1 with a ratio of $\eta\Gamma_{32}/\Gamma_{13}$ as long as N_1 does not vary at a rate faster than Γ_{13}. The last process $|1\rangle \to |2\rangle \to |4\rangle \to |1\rangle$ is similar except that it happens with a time constant $(\eta\Gamma_{42} + \Gamma_{14})^{-1} \sim (\eta\Gamma_{42})^{-1}$. Therefore both N_2 and N_3 have already been locked to N_1.

We now numerically solve Equations (D.1) with the parameters $\Gamma_e = 10^2$ s^{-1}, $\Gamma_{12} = 10^3$ s^{-1}, $\Gamma_{32} = \Gamma_{42} = 10$ s^{-1}, $\Gamma_{13} = 10^2$ s^{-1}, and $\Gamma_{14} = 10^{-1}$ s^{-1}. Figure D.2 shows the evolution of the populations. The numerical result agrees with our breakdown analysis very well. N_2 takes about a few $\Gamma_{12}^{-1} = 10^{-3}$ s to reach the equilibrium with N_1. Then N_3 takes about a few $\Gamma_{13}^{-1} = 10^{-2}$ s to reach the equilibrium with N_1 and N_2. Finally, N_4 takes about a few $(\eta\Gamma_{42})^{-1} = 1$ s to reach the equilibrium with N_1, N_2, and N_3.

What it implies for Yb atoms in solid Ne is that after the 388 nm excitation light is turned on, the population of both $6s6p\ ^1P_1$ and $6s6p\ ^3P_1$ will quickly reach the equilibrium with $6s^2\ ^1S_0$ and follow the change of its population. Since the 388 nm light is capable of depleting $6s^2\ ^1S_0$, this dynamics must be reflected in the fluorescence intensity of $6s6p\ ^3P_1$ as a decay after the initial build-up.

APPENDIX E

DEAD-TIME CORRECTION FOR PERIODIC COUNTS

We use a PMT to record the dynamics of the Yb $6s6p\ ^3P_1$ emission in solid noble-gas matrices. The emission signal is caused by the excitation of a laser chopped at frequency ν. The measurement is timed by a time base that is ticking at frequency ν_0. Once a photon (indexed by n) is detected by the PMT, the data acquisition system records its timestamp with respect to the initial trigger by the order of the chopping cycle (indexed by i_n) and the order of bin (indexed by j_n) within that cycle. The bin width is $1/\nu_0$.

After some time T_0, we collect N photons with timestamps $\{t_n = (i_n, j_n) | n = 1, 2, \cdots, N\}$. Apparently, $1 \leq i_1 \leq i_2 \leq \cdots \leq i_N \leq N_\mathrm{c}$ and $1 \leq j_n \leq N_\mathrm{b}$ for any n, where $N_\mathrm{c} = \nu T_0$ is the total number of chopping cycles and $N_\mathrm{b} = \nu_0/\nu$ is the number of bins in each cycle. To study the averaged signal in one chopping cycle, we plot the histogram $\{H_j | j = 1, 2, \cdots, N_\mathrm{b}\}$, where H_j is total the number of photons registered in bin j and $\sum_{j=1}^{N_\mathrm{b}} H_j = N$. PMT pulses are gated in the nonretriggerable mode with a dead time t_d to eliminate after-pulsing. Once a photon is registered at time t, no photons can be registered within $[t, t + t_\mathrm{d}]$. Therefore the count H_j does not include those unregistered photons during the dead time.

The true count $\bar{H}_j$ is calculated as follows. The lost count $\bar{H}_j - H_j$ should equal the average number of photons arriving in bin j per chopping cycle multiplied by the number of times bin j falls in the dead-time windows caused by the registered photons. This is because each bin is only counted once in one chopping cycle. The first factor is nothing but $\bar{H}_j/N_\mathrm{c}$, where we have used the true count itself. To figure out the second factor, note that bin j only falls in the dead-time windows of those registered photons whose bin indices j' belong to the class $\mathscr{C}_j = \{j - \nu_0 t_\mathrm{d}, \cdots, j-2, j-1\}$ mod N_b. $\mathscr{C}_j$ will have repeating indices if $\nu_0 t_\mathrm{d} > N_\mathrm{b}$. The second factor is then $\sum_{j' \in \mathscr{C}_j} H_{j'}$. Therefore we have

$$\bar{H}_j - H_j = \frac{\bar{H}_j}{N_\mathrm{c}} \cdot \sum_{j' \in \mathscr{C}_j} H_{j'}. \tag{E.1}$$

Solve for the true count $\bar{H}_j$,

$$\bar{H}_j = \frac{H_j}{1 - \sum_{j' \in \mathscr{C}_j} H_{j'}/N_\mathrm{c}}. \tag{E.2}$$

In the continuous case, the above equation becomes

$$\bar{H}(t) = \frac{H(t)}{1 - \int_{t-t_\mathrm{d}}^{t} H(t')\mathrm{d}t'/T_0}, \tag{E.3}$$

where $H(t)$ and $\bar{H}(t)$ are periodic functions defined over $(-\infty, \infty)$. During the transition to the continuum, the periodicity of $H(t)$ automatically takes care of the potentially repeating indices in $\mathscr{C}_j$.

Let us take a look at a particular data set we took on October 24, 2013. The numbers are $\nu = 50$ kHz, $\nu_0 = 20$ MHz, $N_\mathrm{b} = 400$, $N_\mathrm{c} = 21,039,371$, $N = 2,147,000$, and $\nu_0 t_\mathrm{d} = 212$. Since the dead time is shorter than the chopping cycle, $\mathscr{C}_j$ does not contain repeating indices. For example, $\mathscr{C}_{120} = \{308, 309, \cdots, 400, 1, 2, \cdots, 119\}$. Figure E.1 shows the count $\{H_j\}$ before the correction (red) and the count $\{\bar{H}_j\}$ after the correction (blue), and the dead-time correction itself (black).

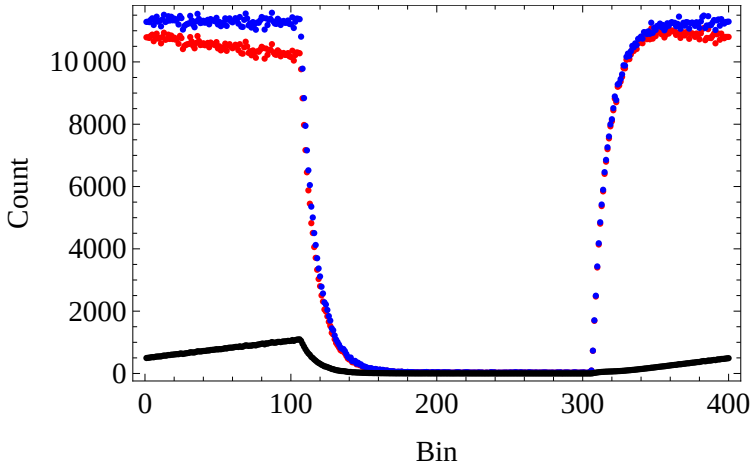

Figure E.1: Red dots: the counting histogram before correction; Blue dots: after correction; Black dots: the dead time correction.

APPENDIX F

PHENOMENOLOGICAL BLOCH EQUATIONS

The solution to the phenomenological Bloch equations (5.1) in this appendix is a generalization of the result in Reference [78]. We first note that the z-component equation

$$\frac{\mathrm{d}P_z}{\mathrm{d}t} = -\tilde{\Gamma}_\mathrm{p}(t)P_z - P_z/T_1 \tag{F.1}$$

is decoupled from the x- and y-components and thus has a trivial solution $P_z(t) \equiv 0$ for the initial condition $P_z(0) = 0$. The remaining x- and y-component equations are written in a complex form

$$\frac{\mathrm{d}\mathcal{P}}{\mathrm{d}t} = \tilde{\Gamma}_\mathrm{p}(t)(P_0 - \mathcal{P}) - \mathcal{P}/T_2 + i\omega_\mathrm{L}\mathcal{P}, \tag{F.2}$$

where the complex polarization $\mathcal{P} = P_x + iP_y$. For the periodic optical pumping rate $\tilde{\Gamma}_\mathrm{p}(t)$ with an angular frequency ω, we Fourier expand it

$$\tilde{\Gamma}_\mathrm{p}(t) = \sum_{n=-\infty}^{\infty} c_n e^{in\omega t}, \tag{F.3}$$

where the Fourier coefficients are

$$c_n = \frac{\omega}{2\pi}\int_0^{2\pi/\omega} \tilde{\Gamma}_\mathrm{p}(t)e^{-in\omega t}\mathrm{d}t. \tag{F.4}$$

Equation (F.2) is solved by a steady-state ansatz $\mathcal{P} = \mathcal{P}_\mathrm{s}e^{i\omega t}$, where $\mathcal{P}_\mathrm{s}$ is a complex amplitude. In the spirit of the rotating-wave approximation, we only keep the $e^{i\omega t}$ terms and then we have

$$\mathcal{P}_\mathrm{s} = P_0 \cdot \frac{c_1}{i(\omega - \omega_\mathrm{L}) + (c_0 + 1/T_2)}. \tag{F.5}$$

The steady-state polarization is

$$P \equiv |\boldsymbol{P}| = |\mathcal{P}| = |\mathcal{P}_\mathrm{s}| = P_0 \cdot \frac{|c_1|}{\sqrt{(\omega - \omega_\mathrm{L})^2 + (c_0 + 1/T_2)^2}}. \tag{F.6}$$

To obtain the build-up of the polarization, we use the ansatz $\mathcal{P} = \mathcal{P}_\mathrm{s}(1 - e^{-t/\tau})e^{i\omega t}$ to solve Equation (F.2), where τ is a complex time constant. Again under the rotating-wave approximation, we have $\tau^{-1} = i(\omega - \omega_\mathrm{L}) + (c_0 + 1/T_2)$ and the same $\mathcal{P}_\mathrm{s}$ in Equation (F.5). The whole solution is

$$\mathcal{P} = P_0 \cdot \frac{c_1}{i(\omega - \omega_\mathrm{L}) + (c_0 + 1/T_2)} \left(1 - e^{-i(\omega-\omega_\mathrm{L})t} e^{-(c_0+1/T_2)t}\right) e^{i\omega t}, \tag{F.7}$$

and the time-dependent polarization is

$$P(t) = P_0 \cdot \frac{|c_1|}{\sqrt{(\omega - \omega_\mathrm{L})^2 + (c_0 + 1/T_2)^2}} \cdot \sqrt{1 - 2\cos[(\omega - \omega_\mathrm{L})t]e^{-(c_0+1/T_2)t} + e^{-2(c_0+1/T_2)t}}. \tag{F.8}$$

When off resonance, the polarization builds up in an under-damped oscillatory way with the angular frequency of the oscillation equal to the detuning $\omega - \omega_\mathrm{L}$. When on resonance, it simply becomes an exponential build-up

$$P(t) = P_0 \cdot \frac{|c_1|}{c_0 + 1/T_2} \left(1 - e^{-(c_0+1/T_2)t}\right), \tag{F.9}$$

where the build-up time is $(c_0 + 1/T_2)^{-1}$.

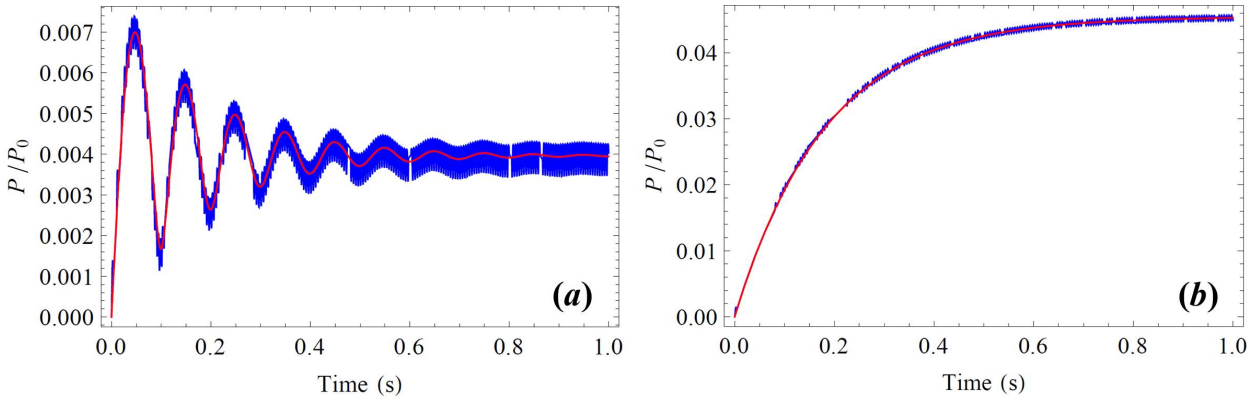

Figure F.1: The solution to Equation (F.2) with $\tilde{\Gamma}_\mathrm{p}(t) = \Gamma_\mathrm{p}(1 + \sin\omega t)/2$, $\Gamma_\mathrm{p} = 1\ \mathrm{s}^{-1}$, $T_2 = 0.2$ s, and $\omega_\mathrm{L} = 2\pi \times 200$ rad/s. The red curves are analytical results under the rotating-wave approximation. The blue curves are numerical results. (a) The off-resonance case, $\omega - \omega_\mathrm{L} = 2\pi \times 100$ rad/s. (b) The on-resonance case.

To verify the analytical result, we numerically solve the Bloch equations for sinusoidally modulated $\tilde{\Gamma}_{\mathrm{p}}(t) = \Gamma_{\mathrm{p}}(1 + \sin\omega t)/2$ of which the Fourier coefficients are $c_0 = \Gamma_{\mathrm{p}}/2$ and $c_1 = \Gamma_{\mathrm{p}}/4i$. The parameters we use are $\Gamma_{\mathrm{p}} = 1\ \mathrm{s}^{-1}$, $T_2 = 0.2$ s, $\omega_{\mathrm{L}} = 2\pi \times 200$ rad/s. In Figure F.1(a) ω has a $2\pi \times 10$ rad/s detuning from ω_{L}, while in Figure F.1(b) ω is on resonance with ω_{L}. The plots show that the analytical solution under the rotating-wave approximation only describes the exact polarization averaged over a $2\pi/\omega$ period of time.

APPENDIX G

CRYSTAL-FIELD HAMILTONIAN

To diagonalize the Hamiltonian (5.4), we first find the matrix representation of the crystal field in the $J' = 1$ subspace of $6s6p\ ^3P_1$ and then promote it to the $I = 1/2 \otimes J' = 1$ subspace by a Kronecker product. The crystal-field potential $U(\boldsymbol{r})$ is expanded

$$U(\boldsymbol{r}) = \sum_{lm} K_{lm}(r) Y_{lm}(\Omega), \tag{G.1}$$

where $Y_{lm}(\Omega)$ are the spherical harmonics. Since the $6s$ electron does not respond to the crystal field, we can use single-particle wave functions of the $6p$ electron $\psi_M(\boldsymbol{r}) = R_M(r) Y_{1M}(\Omega)$ to approximate the three $|J' = 1, M'\rangle$ states of $6s6p\ ^3P_1$. The matrix elements are

$$U^{(1)}_{M'_1 M'_2} = \sum_{lm} \int r^2 \mathrm{d}r R^*_{M'_1}(r) K_{lm}(r) R_{M'_2}(r) \int \mathrm{d}\Omega Y^*_{1M'_1}(\Omega) Y_{lm}(\Omega) Y_{1M'_2}(\Omega). \tag{G.2}$$

The angular integral enforces selection rules that only $l = 0$ and 2 terms in the sum survive and $m = M'_1 - M'_2$. The $l = 0$ term is proportional to the identity matrix and thus does not change the energy eigenstates. Therefore $U^{(1)}_{M'_1 M'_2}$ becomes

$$\int r^2 \mathrm{d}r R^*_{M'_1}(r) K_{2M'_1 - M'_2}(r) R_{M'_2}(r) = q_{M'_1 - M'_2} \tag{G.3}$$

multiplied by a constant obtained from the angular integral. The hermicity dictates $q^*_m = (-1)^m q_{-m}$, so we parameterize $q_0 = a_0$, $q_1 = -q^*_{-1} = a_1 e^{i\phi_1}$, and $q_2 = q^*_{-2} = a_2 e^{i\phi_2}$ with $a_0, a_1, a_2, \phi_1, \phi_2 \in \mathbb{R}$. The crystal-field matrix in the $J' = 1$ subspace is then

$$U^{(1)} = \frac{1}{\sqrt{2\pi}} \begin{pmatrix} -\sqrt{\frac{1}{10}} a_0 & -\sqrt{\frac{3}{10}} a_1 e^{-i\phi_1} & -\sqrt{\frac{6}{10}} a_2 e^{-i\phi_2} \\ -\sqrt{\frac{3}{10}} a_1 e^{i\phi_1} & \sqrt{\frac{4}{10}} a_0 & \sqrt{\frac{3}{10}} a_1 e^{-i\phi_1} \\ -\sqrt{\frac{6}{10}} a_2 e^{i\phi_2} & \sqrt{\frac{3}{10}} a_1 e^{i\phi_1} & -\sqrt{\frac{1}{10}} a_0 \end{pmatrix}. \tag{G.4}$$

We use Kronecker products ($\otimes$) to construct the 6D space from the 2D space of $I = 1/2$ and the 3D space of $J' = 1$ and solve the Hamiltonian (5.4) in the 6D space of $I = 1/2 \otimes J' = 1$. The matrix representations of angular momentum operators are

$$j_x^{(1/2)} = \frac{1}{2}\begin{pmatrix} 0 & 1 \\ 1 & 0 \end{pmatrix},\ j_y^{(1/2)} = \frac{1}{2}\begin{pmatrix} 0 & -i \\ i & 0 \end{pmatrix},\ \text{and } j_z^{(1/2)} = \frac{1}{2}\begin{pmatrix} -1 & 0 \\ 0 & 1 \end{pmatrix} \tag{G.5}$$

in 2D and

$$j_x^{(1)} = \frac{1}{\sqrt{2}}\begin{pmatrix} 0 & 1 & 0 \\ 1 & 0 & 1 \\ 0 & 1 & 0 \end{pmatrix},\ j_y^{(1)} = \frac{1}{\sqrt{2}}\begin{pmatrix} 0 & -i & 0 \\ i & 0 & -i \\ 0 & i & 0 \end{pmatrix},\ \text{and } j_z^{(1)} = \frac{1}{\sqrt{2}}\begin{pmatrix} -1 & 0 & 0 \\ 0 & 0 & 0 \\ 0 & 0 & 1 \end{pmatrix} \tag{G.6}$$

in 3D. Therefore the Hamiltonian matrix in the 6D space is

$$\mathscr{H}_{\text{HFI+CF}}^{6\times 6} = \kappa\left(j_x^{(1/2)} \otimes j_x^{(1)} + j_y^{(1/2)} \otimes j_y^{(1)} + j_z^{(1/2)} \otimes j_z^{(1)}\right) + \mathbf{1}_2 \otimes U^{(1)}, \tag{G.7}$$

where $\mathbf{1}_2$ is the 2D identity matrix. The basis vectors in the 6D space are also Kronecker products of the 2D and the 3D basis vectors. For example, since $(1, 0)$ represents $|M_I = -1/2\rangle$ and $(1, 0, 0)$ represents $|M'_J = -1\rangle$, then $(1, 0, 0, 0, 0, 0) = (1, 0) \otimes (1, 0, 0)$ represents $|M_I = -1/2, M'_J = -1\rangle$. Given a set of crystal-field parameters a_0, a_1, a_2, ϕ_1, and ϕ_2, the eigenvalues of the Hamiltonian matrix (G.7) can be numerically obtained and are labeled as λ_i with eigenstates $|\lambda_i\rangle$ $(i = 1, 2, \cdots, 6)$.

APPENDIX H

MAGNETIC FLUX OF A UNIFORMLY POLARIZED DISK

Consider the case where the polarized disk and the pick-up loop are coaxial (Figure H.1). Let the radius of the disk be R, that of the loop be R', and the distance between them be d. The disk has a uniform surface density of magnetic dipoles $n_{2,\mu}$, and each magnetic dipole has a magnetic dipole moment $\boldsymbol{\mu}$ polarized perpendicular to the disk.

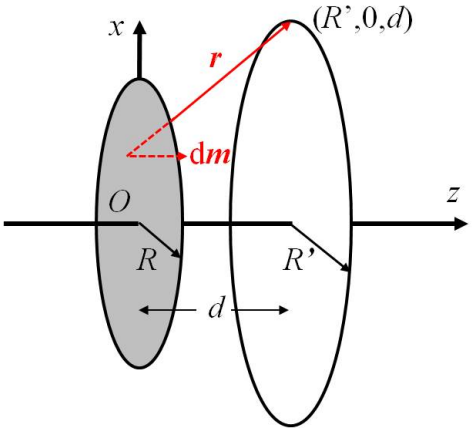

Figure H.1: A pick-up loop coaxially aligned with a uniformly polarized disk.

The magnetic flux Φ is the surface integral of the flux density $\boldsymbol{B}$ generated by the disk on a two dimensional surface Σ enclosed by the loop. Using Stoke's theorem and the vector potential $\boldsymbol{A}$, we can write

$$\Phi = \iint_{\Sigma} \mathrm{d}\boldsymbol{\Sigma} \cdot \boldsymbol{B} = \iint_{\Sigma} \mathrm{d}\boldsymbol{\Sigma} \cdot (\nabla \times \boldsymbol{A}) = \oint_{\partial\Sigma} \mathrm{d}(\partial\boldsymbol{\Sigma}) \cdot \boldsymbol{A}, \tag{H.1}$$

where $\partial\Sigma$ is in fact the loop itself. Due to the azimuthal symmetry, $\boldsymbol{A}$ is tangential to the loop and has the same magnitude along the loop. Therefore the line integral is simplified

$$\Phi = \oint_{\text{loop}} \mathrm{d}(\partial\boldsymbol{\Sigma}) \cdot \boldsymbol{A}_{\text{disk}} = 2\pi R' \cdot |\boldsymbol{A}^0_{\text{disk}}|, \tag{H.2}$$

where $\boldsymbol{A}^0_{\text{disk}}$ can be calculated at any point on the loop, for example $(R', 0, d)$.

Consider an infinitesimal area $\mathrm{d}x\mathrm{d}y$ on the disk, which has a magnetic dipole moment $\mathrm{d}\boldsymbol{m} = \mu n_{2,\mu}\mathrm{d}x\mathrm{d}y\hat{z}$. Its contribution to $\boldsymbol{A}^0_{\text{disk}}$ is

$$\mathrm{d}\boldsymbol{A}^0_{\text{disk}} = \frac{\mu_0}{4\pi}\frac{\mathrm{d}\boldsymbol{m}\times\boldsymbol{r}}{r^3}, \tag{H.3}$$

where $\boldsymbol{r}$ is the displacement vector from $\mathrm{d}\boldsymbol{m}$ to $(R', 0, d)$. $\boldsymbol{A}^0_{\text{disk}}$ is then the integral of $\mathrm{d}\boldsymbol{A}^0_{\text{disk}}$ over the disk. Using polar coordinates ρ, ϕ, and z, we have

$$\boldsymbol{r} = (R' - \rho\cos\phi, -\rho\sin\phi, d),\ r = \sqrt{R'^2 - 2R'\rho\cos\phi + \rho^2 + d^2}, \tag{H.4}$$

$$\mathrm{d}\boldsymbol{m}\times\boldsymbol{r} = \mu n_{2,\mu}\rho\mathrm{d}\rho\mathrm{d}\phi(\rho\sin\phi\hat{x} + (R' - \rho\cos\phi)\hat{y}). \tag{H.5}$$

The x-component of $\mathrm{d}\boldsymbol{m}\times\boldsymbol{r}$ is integrated to zero since we expect $\boldsymbol{A}^0_{\text{disk}}$ to be along y-axis at $(R', 0, d)$. Therefore the magnetic flux from the disk inside the loop is

$$\Phi = 2\pi R'\cdot\frac{\mu_0\mu n_{2,\mu}}{4\pi}\int_0^R \rho\mathrm{d}\rho\int_0^{2\pi}\mathrm{d}\phi\frac{R' - \rho\cos\phi}{(R'^2 - 2R'\rho\cos\phi + \rho^2 + d^2)^{3/2}}. \tag{H.6}$$

Define $\alpha = R'/R$ and $\beta = d/R$ and the magnetic flux can be written $\Phi = \Phi_{\text{disk}}g(\alpha,\beta)$, where $\Phi_{\text{disk}} = \frac{1}{2}\mu_0\mu n_{2,\mu}R$ and

$$g(\alpha,\beta) = \int_0^1 \mathrm{d}x\int_0^{2\pi}\mathrm{d}\phi\frac{\alpha x(\alpha - x\cos\phi)}{(\alpha^2 - 2\alpha x\cos\phi + x^2 + \beta^2)^{3/2}}. \tag{H.7}$$

Φ_{disk} is in the dimension of magnetic flux and only depends on the parameters of the disk while $g(\alpha,\beta)$ is a dimensionless function. $g(\alpha,\beta)$ logarithmically diverges when (α,β) approaches the segment $\{0 \le \alpha \le 1, \beta = 0\}$. The physical meaning is that when the disk and the loop are coplanar, the loop has to be larger than the disk in order to have a well-defined flux. Here are two asymptotic behaviors of $g(\alpha,\beta)$ and Φ. When $\beta \gg \alpha \sim 1$, $g(\alpha,\beta) \sim \pi\alpha^2/\beta^3$ and $\Phi \sim \pi\mu_0\mu n_{2,\mu}R'^2R^2/2d^3$. When $\alpha \gg \beta \sim 1$, $g(\alpha,\beta) \sim \pi/\alpha$ and $\Phi \sim \pi\mu_0\mu n_{2,\mu}R^2/R'$.

APPENDIX I

AXIAL-GRADIOMETER TYPE PICK-UP COIL

An n-th order axial gradiometer pick-up coil is designed to measure the n-th order gradient of a field. Consider a pick-up coil consisting of $n+1$ loops with an identical area δa and alternating winding directions (Figure I.1). The number of turns for each loop is given by the binomial coefficients C_n^k $(0 \leq k \leq n)$. The loops are uniformly placed along an axis with a spacing d and the normal of the loops is parallel to the axis. The dimension of the pick-up coil is assumed to be small compared to the variation length of the magnetic field.

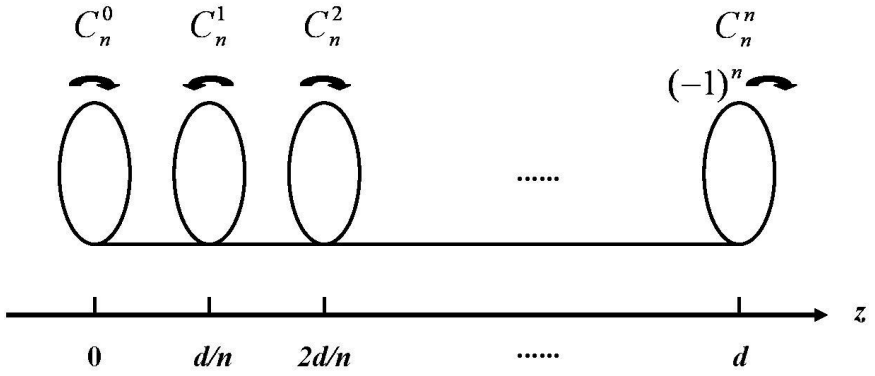

Figure I.1: A sketch of the n-th order axial gradiometer.

The total flux $\delta\Phi$ generated by the axial component of a magnetic field $B_z(z)$ in this pick-up coil is

$$\delta\Phi = \sum_{k=0}^{n} (-1)^k C_n^k B_z\left(\frac{k}{n}d\right)\delta a. \tag{I.1}$$

Substituting the Taylor expansion of $B_z(z)$ around $z=0$ into the flux density, we have

$$\frac{\delta\Phi}{\delta a} = \sum_{k=0}^{n}(-1)^k C_n^k \sum_{m=0}^{\infty}\frac{B_z^{(m)}(0)}{m!}\left(\frac{k}{n}d\right)^m = \sum_{m=0}^{\infty}\left(\sum_{k=0}^{n}(-1)^k C_n^k k^m\right)\frac{B_z^{(m)}(0)}{m!}\left(\frac{d}{n}\right)^m. \tag{I.2}$$

We are going to show that for any $m < n$, the sum in the parentheses $\sum_{k=0}^{n}(-1)^k C_n^k k^m$ vanishes. Therefore all the gradients of the magnetic field $B_z^{(m)}(0)$ lower than the n-th order cancel out in the measured flux density.

Note that the following identity holds for any non-negative integers m and n

$$\left[\left(x\frac{\mathrm{d}}{\mathrm{d}x}\right)^m (1-x)^n\right]_{x=1} = \sum_{k=0}^{n}(-1)^k C_n^k k^m, \tag{I.3}$$

which can be seen by first doing the binomial expansion on the left-hand side, then taking the derivatives m times, and finally setting x to 1. If we take the derivatives first, it is easy to observe that for $m < n$ each term in the result has at least one factor of $(1-x)$. Therefore setting x to 1 kills all the terms and we arrive at the following identity

$$\sum_{k=0}^{n}(-1)^k C_n^k k^m = 0 \ (m < n). \tag{I.4}$$

This means the expansion of the flux density starts from the n-th order term

$$\frac{\delta\Phi}{\delta a} = \sum_{m=n}^{\infty}\left(\sum_{k=0}^{n}(-1)^k C_n^k k^m\right)\frac{B_z^{(m)}(0)}{m!}\left(\frac{d}{n}\right)^m = (-1)^n B_z^{(n)}(0)\left(\frac{d}{n}\right)^n + O(d^{n+1}), \tag{I.5}$$

which is proportional to the n-th order gradient of the magnetic field.

REFERENCES

[1] E. D. Becker and G. C. Pimentel. Spectroscopic Studies of Reactive Molecules by the Matrix Isolation Method. *J. Chem. Phys.*, 25:224, 1956.

[2] V. E. Bondybey, A. M. Smith, and J. Agreiter. New Developments in Matrix Isolation Spectroscopy. *Chem. Rev.*, 96:2113, 1996.

[3] W. E. Moerner and L. Kador. Optical Detection and Spectroscopy of Single Molecules in a Solid. *Phys. Rev. Lett.*, 62:2535, 1989.

[4] C. Crépin-Gilbert and A. Tramer. Photophysics of Metal Atoms in Rare-Gas Complexes, Clusters and Matrices. *Int. Rev. Phys. Chem.*, 18:485, 1999.

[5] M. Lax. The Franck-Condon Principle and Its Application to Crystals. *J. Chem. Phys.*, 20:1752, 1952.

[6] I. G. Kaplan. *Intermolecular Interactions*. John Wiley & Sons Publishing, Hoboken, 2006.

[7] C.-Y. Xu, J. Singh, J. C. Zappala, K. G. Bailey, M. R. Dietrich, J. P. Greene, W. Jiang, N. D. Lemke, Z.-T. Lu, P. Mueller, and T. P. O'Connor. Measurement of the Hyperfine Quenching Rate of the Clock Transition in ^{171}Yb. *Phys. Rev. Lett.*, 113:033003, 2014.

[8] A. N. Kanagin, S. K. Regmi, P. Pathak, and J. D. Weinstein. Optical Pumping of Rb Atoms Frozen in Solid Ar. *Phys. Rev. A*, 88:063404, 2013.

[9] A. E. Ezwam and J. Billowes. A Solid Xe Catcher for Rare Isotope Laser Spectroscopy. *Hyperfin Interact.*, 162:189, 2005.

[10] M. Danilov, R. DeVoe, A. Dolgolenko, G. Giannini, G. Gratta, P. Picchi, A. Piepke, F. Pietropaolo, P. Vogel, J.-L. Vuilleumier, Y.-F. Wang, and O. Zeldovich. Detection of Very Small Neutrino Masses in Double-Beta Decay Using Laser Tagging. *Phys. Lett. B*, 480:12, 2000.

[11] A. Weis, S. Kanorsky, S. Lang, and T.W. Hänsch. Can Atoms Trapped in Solid He Be Used to Search for Physics Beyond the Standard Model? In K. Jungmann, J. Kowalski, I. Reinhard, and F. Träger, editors, *Atomic Physics Methods in Modern Research*, volume 499 of *Lecture Notes in Physics*, page 57. Springer Berlin Heidelberg, 1997.

[12] W. Weyhmann and F. M. Pipkin. Optical Absorption Spectra of Alkali Atoms in Rare-Gas Matrices. *Phys. Rev.*, 137:A490, 1965.

[13] S. L. Kupferman and F. M. Pipkin. Properties of Rb Atoms Trapped in a Solid Ar Matrix. *Phys. Rev.*, 166:207, 1968.

[14] T. Kinoshita, Y. Takahashi, and T. Yabuzaki. Optical Pumping and Optical Detection of the Magnetic Resonance of Alkali-Metal Atoms in Superfluid Helium. *Phys. Rev. B*, 49:3648, 1994.

[15] M. Arndt, S. I. Kanorsky, A. Weis, and T. W. Hänsch. Long Electronic Spin Relaxation Times of Cs Atoms in Solid ^{4}He. *Phys. Rev. Lett.*, 74:1359, 1995.

[16] L. F. Mollenauer, W. B. Grant, and C. D. Jeffries. Achievement of Significant Nuclear Polarization in Solids by Optical Pumping. *Phys. Rev. Lett.*, 20:488, 1968.

[17] K. Shimomura, I. Ogawa, K. Suzuki, S. Hamada, T. Nakamura, H. Okuno, M. Koizumi, N. Inabe, Y. Fukashiro, H. Sunaoshi, M. Wada, S. Hatori, T. Murayama, T. Kohmoto, Y. Fukuda, T. Kubo, T. Shinozuka, K. Asahi, S. Morinobu, T.T. Inamura, M. Ishihara, M. Fujioka, M. Kondo, and S. Matsuki. OPERA: An On-Line System of Optical Pumping in Solids for Unstable Nuclei. *Nucl. Instrum. Methods Phys. Res. B*, 70:513, 1992.

[18] L. I. Schiff. Measurability of Nuclear Electric Dipole Moments. *Phys. Rev.*, 132:2194, 1963.

[19] M. Gatzke, G. D. Cates, B. Driehuys, D. Fox, W. Happer, and B. Saam. Extraordinarily Slow Nuclear Spin Relaxation in Frozen Laser-Polarized ^{129}Xe. *Phys. Rev. Lett.*, 70:690, 1993.

[20] C. P. Slichter. *Principles of Magnetic Resonance*. Springer-Verlag, New York, 1978.

[21] A. C. Gossard, V. Jaccarino, and J. H. Wernick. Yb NMR: ^{171}Yb Nuclear Moment and Yb Metal Knight Shift. *Phys. Rev.*, 133:A881, 1964.

[22] N. W. Ashcroft and N. D. Mermin. *Solid State Physics*. Saunders College Publishing, Philadelphia, 1976.

[23] H. Coufal, E. Lüscher, H. Micklitz, and R. E. Norberg. *Rare Gas Solids*. Springer-Verlag, New York, 1984.

[24] C.-Y. Xu, S.-M. Hu, J. Singh, K. G. Bailey, Z.-T. Lu, P. Mueller, T. P. O'Connor, and U. Welp. Optical Excitation and Decay Dynamics of Yb Atoms Embedded in a Solid Ne Matrix. *Phys. Rev. Lett.*, 107:093001, 2011.

[25] Wikipedia. Ytterbium — Wikipedia, the Free Encyclopedia. `http://en.wikipedia.org/wiki/ytterbium`, 2014. Accessed on 20-November-2014.

[26] J. F. O'Hanlon. *A User's Guide to Vacuum Technology*. John Wiley & Sons Publishing, Hoboken, 2003.

[27] T. Momose, M. Miki, T. Wakabayashi, T. Shida, M.-C. Chan, S. S. Lee, and T. Oka. Infrared Spectroscopic Study of Rovibrational States of Methane Trapped in Parahydrogen Crystal. *J. Chem. Phys.*, 107:7707, 1997.

[28] G. A. Cook. *Argon, Helium, and the Rare Gases*. Interscience Publishing, New York, 1961.

[29] W. H. Keesom and J. Haantjes. The Vapour Pressure of Ne at Liquid H_2 Temperatures. *Physica*, 2:460, 1935.

[30] I. R. Dunkin. *Matrix-Isolation Techniques*. Oxford University Press, New York, 1998.

[31] A. Y. Cho and J. R. Arthur. Molecular Beam Epitaxy. *Prog. Solid State Chem.*, 10:157, 1975.

[32] N. F. Ramsey. *Molecular Beams*. Oxford University Press, New York, 1990.

[33] J. A. McClintock and R. A. Wilson. Optical Measurement of Ga Beam Flux for Molecular Beam Epitaxy. *J. Cryst. Growth*, 81:177, 1987.

[34] R. Lambo, C. C. Rodegheri, D. M. Silveira, and C. L. Cesar. Spectroscopy of Low-Energy Atoms Released from a Solid Noble-Gas Matrix: Proposal for a Trap-Loading Technique. *Phys. Rev. A*, 76:061401, 2007.

[35] R. D. Cowan and K. L. Andrew. Coupling Considerations in Two-Electron Spectra. *J. Opt. Soc. Am.*, 55:502, 1965.

[36] A. Corney. *Atomic and Laser Spectroscopy*. Clarendon Press, Oxford, 1977.

[37] S. Suzer and L. Andrews. Optical Spectra of Yb Atoms and Dimers in Rare Gas Matrices. *J. Chem. Phys.*, 89:5514, 1988.

[38] H. W. Carstens, W. Brashear, D. R. Eslinger, and D. M. Gruen. The Correlation between Gaseous Atomic Spectra and the Absorption Spectra of Atoms Isolated in Noble-Gas Matrices. *Appl. Spectros.*, 26:184, 1972.

[39] C. J. Foot. *Atomic Physics*. Oxford University Press, New York, 2005.

[40] N. Allard and J. Kielkopf. The Effect of Neutral Nonresonant Collisions on Atomic Spectral Lines. *Rev. Mod. Phys.*, 54:1103, 1982.

[41] D. Hsu and J. L. Skinner. On the Thermal Broadening of Zero-Phonon Impurity Lines in Absorption and Fluorescence Spectra. *J. Chem. Phys.*, 81:1604, 1984.

[42] D. Hsu and J. L. Skinner. Nonperturbative Theory of Temperature-Dependent Optical Dephasing in Crystals. I. Acoustic or Optical Phonons. *J. Chem. Phys.*, 81:5471, 1984.

[43] R. Schinke. *Photodissociation Dynamics*. Cambridge University Press, New York, 1993.

[44] R. Lambo, A. A. Buchachenko, L. Wu, Y. Tan, J. Wang, Y. R. Sun, A.-W. Liu, and S.-M. Hu. Electronic Spectroscopy of Yb in a Ne Matrix. *J. Chem. Phys.*, 137:204315, 2012.

[45] M. Tinkham. *Group Theory and Quantum Mechanics*. McGraw-Hill Book Company, New York, 1964.

[46] H. A. Bethe. Termaufspaltung in Kristallen. *Ann. Physik*, 395:133, 1929.

[47] I. S. Bowen. Forbidden Lines. *Rev. Mod. Phys.*, 8:55, 1936.

[48] R. H. Garstang. Hyperfine Structure and Intercombination Line Intensities in the Spectra of Mg, Zn, Cd, and Hg. *J. Opt. Soc. Am.*, 52:845, 1962.

[49] T. Brage, P. G. Judge, and C. R. Proffitt. Determination of Hyperfine-Induced Transition Rates from Observations of a Planetary Nebula. *Phys. Rev. Lett.*, 89:281101, 2002.

[50] R. H. Rubin, G. J. Ferland, E. E. Chollet, and R. Horstmeyer. $^{12}C/^{13}C$ Ratio in Planetary Nebulae from the IUE Archives. *Astrophys. J.*, 605:784, 2004.

[51] W. R. Johnson. Hyperfine Quenching: Review of Experiment and Theory. *Can. J. Phys.*, 89:429, 2011.

[52] E. Träbert, M. Grieser, J. Hoffmann, C. Krantz, S. Reinhardt, R. Repnow, A. Wolf, and P. Indelicato. $M1, M2$ and Hyperfine-Induced Decay Rates in Mg-like ions of Co, Ni and Cu Measured at a Heavy-Ion Storage Ring. *New J. Phys.*, 13:023017, 2011.

[53] S. Schippers, D. Bernhardt, A. Müller, M. Lestinsky, M. Hahn, O. Novotný, D. W. Savin, M. Grieser, C. Krantz, R. Repnow, and A. Wolf. Storage-Ring Measurement of the Hyperfine-Induced $2s2p\ ^3P_0 \rightarrow 2s^2\ ^1S_0$ Transition Rate in Be-like S. *Phys. Rev. A*, 85:012513, 2012.

[54] T. Becker, J. v. Zanthier, A. Y. Nevsky, C. Schwedes, M. N. Skvortsov, H. Walther, and E. Peik. High-Resolution Spectroscopy of a Single In^+ Ion: Progress Towards an Optical Frequency Standard. *Phys. Rev. A*, 63:051802, 2001.

[55] S. G. Porsev and A. Derevianko. Hyperfine Quenching of the Metastable $^3P_{0,2}$ States in Divalent Atoms. *Phys. Rev. A*, 69:042506, 2004.

[56] R. Santra, K. V. Christ, and C. H. Greene. Properties of Metastable Alkaline-Earth-Metal Atoms Calculated Using an Accurate Effective Core Potential. *Phys. Rev. A*, 69:042510, 2004.

[57] A. Derevianko and H. Katori. Colloquium: Physics of Optical Lattice Clocks. *Rev. Mod. Phys.*, 83:331, 2011.

[58] A. J. Daley. Quantum Computing and Quantum Simulation with Group-II Atoms. *Quantum Inf. Process.*, 10:865, 2011.

[59] I. Bloch, J. Dalibard, and W. Zwerger. Many-Body Physics with Ultracold Gases. *Rev. Mod. Phys.*, 80:885, 2008.

[60] H Walther, B. T. H. Varcoe, B.-G. Englert, and T. Becker. Cavity Quantum Electrodynamics. *Rep. Prog. Phys.*, 69:1325, 2006.

[61] K. H. Drexhage. Influence of a Dielectric Interface on Fluorescence Decay Time. *J. Lumin.*, 1–2:693, 1970.

[62] D. J. Heinzen, J. J. Childs, J. E. Thomas, and M. S. Feld. Enhanced and Inhibited Visible Spontaneous Emission by Atoms in a Confocal Resonator. *Phys. Rev. Lett.*, 58:1320, 1987.

[63] F. A. Inam, T. Gaebel, C. Bradac, L. Stewart, M. J. Withford, J. M. Dawes, J. R. Rabeau, and M. J. Steel. Modification of Spontaneous Emission from Nanodiamond Colour Centres on a Structured Surface. *New Journal of Physics*, 13:073012, 2011.

[64] D. Toptygin. Effects of the Solvent Refractive Index and Its Dispersion on the Radiative Decay Rate and Extinction Coefficient of a Fluorescent Solute. *J. Fluoresc.*, 13:201, 2003.

[65] K. Dolgaleva and R. W. Boyd. Local-Field Effects in Nanostructured Photonic Materials. *Adv. Opt. Photon.*, 4:1, 2012.

[66] K. Beloy, J. A. Sherman, N. D. Lemke, N. Hinkley, C. W. Oates, and A. D. Ludlow. Determination of the $5d6s\ ^3D_1$ State Lifetime and Blackbody-Radiation Clock Shift in Yb. *Phys. Rev. A*, 86:051404, 2012.

[67] S. G. Porsev, Y. G. Rakhlina, and M. G. Kozlov. Electric-Dipole Amplitudes, Lifetimes, and Polarizabilities of the Low-Lying Levels of Atomic Yb. *Phys. Rev. A*, 60:2781, 1999.

[68] Joint Committee for Guides in Metrology, Bureau Intertional des Poids et Mesures. Evaluation of Measurement Data – Guide to the Expression of Uncertainty in Measurement. `http://www.bipm.org/utils/common/documents/jcgm/JCGM_100_2008_E.pdf`, 2008. For a uniform probability distribution defined in the interval $[-a/2, a/2]$, the standard deviation, or the second moment of the distribution, is equal to $a/\sqrt{12}$.

[69] A. P. Mishra and T. K. Balasubramanian. Radiative Lifetimes of the First Excited $^3P^\circ_{2,0}$ Metastable Levels in Kr I, Xe I, Yb I and Hg-Like Atoms. *J. Quant. Spectrosc. Radiat Transfer*, 69:769, 2001.

[70] G. L. J. A. Rikken and Y. A. R. R. Kessener. Local Field Effects and Electric and Magnetic Dipole Transitions in Dielectrics. *Phys. Rev. Lett.*, 74:880, 1995.

[71] F. J. P. Schuurmans, D. T. N. de Lang, G. H. Wegdam, R. Sprik, and A. Lagendijk. Local-Field Effects on Spontaneous Emission in a Dense Supercritical Gas. *Phys. Rev. Lett.*, 80:5077, 1998.

[72] R. J. Glauber and M. Lewenstein. Quantum Optics of Dielectric Media. *Phys. Rev. A*, 43:467, 1991.

[73] D. N. Batchelder, D. L. Losee, and R. O. Simmons. Measurements of Lattice Constant, Thermal Expansion, and Isothermal Compressibility of Ne Single Crystals. *Phys. Rev.*, 162:767, 1967.

[74] A. Dewaele, J. H. Eggert, P. Loubeyre, and R. Le Toullec. Measurement of Refractive Index and Equation of State in Dense He, H_2, H_2O and Ne under High Pressure in a Diamond Anvil Cell. *Phys. Rev. B*, 67:094112, 2003.

[75] W. Schulze and D. M. Kolb. Density and Refractive Index of Solid Layers of Noble Gases and Sulphur Hexafluoride. *J. Chem. Soc., Faraday Trans. 2*, 70:1098, 1974.

[76] A. C. Sinnock and B. L. Smith. Refractive Indices of the Condensed Inert Gases. *Phys. Rev.*, 181:1297, 1969.

[77] Stone, N., National Nuclear Data Center, Brookhaven National Laboratory. Table of Nuclear Magnetic Dipole and Electric Quadrupole Moments. `http://www.nndc.bnl.gov/nndc/stone_moments/nuclear-moments.pdf`, 2001.

[78] W. E. Bell and A. L. Bloom. Optically Driven Spin Precession. *Phys. Rev. Lett.*, 6:280, 1961.

[79] W. E. Bell and A. L. Bloom. Optical Detection of Magnetic Resonance in Alkali Metal Vapor. *Phys. Rev.*, 107:1559, 1957.

[80] J. D. Weinstein. Private Communication. 2014.

[81] J. H. Van Vleck. The Dipolar Broadening of Magnetic Resonance Lines in Crystals. *Phys. Rev.*, 74:1168, 1948.

[82] J. Singh. Private Communication. 2011.

[83] I. M. Savukov, S.-K. Lee, and M. V. Romalis. Optical Detection of Liquid-State NMR. *Nature*, 442:1021, 2006.

[84] R. L. Fagaly. Superconducting Quantum Interference Device Instruments and Applications. *Rev. Sci. Instrum.*, 77:101101, 2006.

[85] J. C. Zappala. Private Communication. 2014.

[86] X.-D. Tang. Private Communication. 2011.

[87] B. J. Bloom, T. L. Nicholson, J. R. Williams, S. L. Campbell, M. Bishof, X. Zhang, W. Zhang, S. L. Bromley, and J. Ye. An Optical Lattice Clock with Accuracy and Stability at the 10^{-18} Level. *Nature*, 506:71, 2014.

[88] A. Jayaraman. Diamond Anvil Cell and High-Pressure Physical Investigations. *Rev. Mod. Phys.*, 55:65, 1983.

[89] W. Hanle. Über Magnetische Beeinflussung der Polarisation der Resonanzfluoreszenz. *Z. Phys.*, 30:93, 1924.

[90] G. D. Cates, D. R. Benton, M. Gatzke, W. Happer, K. C. Hasson, and N. R. Newbury. Laser Production of Large Nuclear-Spin Polarization in Frozen Xe. *Phys. Rev. Lett.*, 65:2591, 1990.